Spring 2012

Auger-mediated processes and photoluminescence in group iv semiconductor nanostructures

Nikhil Modi
New Jersey Institute of Technology

ABSTRACT

AUGER-MEDIATED PROCESSES AND PHOTOLUMINESCENCE IN GROUP IV SEMICONDUCTOR NANOSTRUCTURES

by
Nikhil Modi

Group IV semiconductors (Si, Ge) are inefficient light emitting materials due to their indirect bandgap structure. Nanostructures of Si, Ge, and SiGe however, have shown relatively high photoluminescence (PL) quantum efficiency (QE) at low carrier concentrations. At higher carrier concentrations, the PL QE of these nanostructures is drastically reduced due to the onset of a fast non-radiative process attributed to Auger recombination. Moreover, this onset occurs earlier in structures with reduced physical dimensions, than in bulk material. The study of Auger-mediated processes in group IV nanostructures is therefore critical to understanding the physics of carrier recombination and photonic device limitations. This work investigates recombination mechanisms in two such systems: the silicon/silicon germanium three-dimensional (3D) nanostructure system, and the silicon-on-insulator (SOI) system.

Recombination mechanisms are studied by several experimental techniques. One approach explores the steady state PL spectroscopy and PL dynamics under pulsed excitations with varying concentrations of photo-generated charge carriers in the investigated systems. Another important technique uses selective, wavelength dependent photoexcitation to generate carriers up to varying depths in the nanostructures, enabling the understanding of local differences in PL properties through the thickness of structures.

Several interesting observations are reported and underlying recombination mechanisms are discussed. For the Si/SiGe 3D nanostructure system, these include a reversible degradation of the PL after a few minutes of relative stability, an Auger Fountain mechanism that redistributes charge carriers within the nanostructure, and a severe reduction of the exciton diffusion length. For the SOI system, an apparently successful competition of the radiative recombination of carriers in a condensed excitonic phase with Auger processes is observed. The influence of the Si/SiO_2 interface on the recombination mechanism in this system is emphasized. Results of the experiments show that the coexistence of a type II energy band alignment at Si/SiGe interfaces, the electron-hole-droplets in Si, and Auger-mediated processes results in several unusual photoluminescence properties in SiGe and Si nanostructures.

AUGER-MEDIATED PROCESSES AND PHOTOLUMINESCENCE IN GROUP IV SEMICONDUCTOR NANOSTRUCTURES

by
Nikhil Modi

A Dissertation
Submitted to the Faculty of
New Jersey Institute of Technology
in Partial Fulfillment of the Requirements for the Degree of
Doctor of Philosophy in Electrical Engineering

Department of Electrical and Computer Engineering

May 2012

.

APPROVAL PAGE

AUGER-MEDIATED PROCESSES AND PHOTOLUMINESCENCE IN GROUP IV SEMICONDUCTOR NANOSTRUCTURES

Nikhil Modi

Dr. Leonid Tsybeskov, Dissertation Advisor — Date
Professor of Electrical and Computer Engineering, NJIT

Dr. Anthony Fiory, Committee Member — Date
Distinguished Scientist of Physics, NJIT

Dr. Haim Grebel, Committee Member — Date
Professor of Electrical and Computer Engineering, NJIT

Dr. Marek Sosnowski, Committee Member — Date
Professor of Electrical and Computer Engineering, NJIT

Dr. Tao Zhou, Committee Member — Date
Associate Professor of Physics, NJIT

BIOGRAPHICAL SKETCH

Author: Nikhil Modi

Degree: Doctor of Philosophy

Date: May 2012

Undergraduate and Graduate Education:

- Doctor of Philosophy in Electrical Engineering,
  New Jersey Institute of Technology, Newark, NJ, 2012

- Master of Science in Electrical Engineering,
  Southern University, Baton Rouge, LA, 2006

- Bachelor of Science in Electrical and Computer Engineering,
  Louisiana State University, Baton Rouge, LA, 2002

Major: Electrical Engineering

Presentations and Publications:

- Oral Conference Presentations

N. Modi, L. Tsybeskov, D. J. Lockwood, X. Z. Wu, and J-M. Baribeau, "Photoluminescence in Strain-Engineered Si/SiGe Three Dimensional Nanostructures," *American Physical Society March Meeting*, Dallas, TX, 2011.

- Poster Conference Presentations

N. Modi, L. Tsybeskov, D. J. Lockwood, X. Z. Wu, and J-M. Baribeau, "Strain Engineering and Luminescence in Si/SiGe Three Dimensional Nanostructures," *Materials Research Society 2010 Fall Conference*, Boston, MA, 2010.

N. Modi, L. Tsybeskov, J-M. Baribeau, X. Wu, and D. J. Lockwood, "Fatigue of Photoluminescence in Si/SiGe Three-Dimensional Nanostructures," *Materials Research Society 2011 Fall Conference*, Boston, MA, 2011.

- Journal Publications

N. Modi, L. Tsybeskov, J-M. Baribeau, X. Wu, and D. J. Lockwood, "Excitation wavelength dependent photoluminescence in Si/SiGe island multilayers," *Journal of Applied Physics*, Accepted, 2012.

N. Modi, L. Tsybeskov, J-M. Baribeau, X. Wu, and D. J. Lockwood, "Photoluminescence fatigue in three-dimensional silicon/silicon-germanium nanostructures," *Journal of Applied Physics*, vol. 111, pp. 064318, 2012.

- Conference Proceedings Publications

N. Modi, L. Tsybeskov, D. J. Lockwood, X. Z. Wu, and J-M. Baribeau, "Strain Engineering and Luminescence in Si/SiGe Three Dimensional Nanostructures," *Materials Research Society 2010 Fall Conference*, vol. 1305, AA17-56, 2010.

N. Modi, L. Tsybeskov, D. J. Lockwood, X. Z. Wu, and J-M. Baribeau, "Reversible Degradation of Photoluminescence in Si/SiGe Three Dimensional Nanostructures," *Materials Research Society 2011 Fall Conference*, vol. 1409, CC13-08, 2011.

To those that confront cultural barriers

ACKNOWLEDGMENT

I would like to express my deepest appreciation to my research advisor, Dr. Leonid Tsybeskov, for his guidance, patience, and support through this undertaking. I would like to thank Dr. Anthony Fiory, Dr. Haim Grebel, Dr. Marek Sosnowski, and Dr. Tao Zhou, for kindly serving as members of the dissertation committee. I would also like to thank Mr. Bruce Slutsky and the library staff for their prompt assistance during the years of this research. I am deeply thankful to Ms. Radhika Nukala and Ranjani Narayanan for assuming the role of family, and Manveer Sidhu and Binu Weerasinghe for refreshing humor.

TABLE OF CONTENTS

TABLE OF CONTENTS
(Continued)

Chapter **Page**

LIST OF TABLES

LIST OF FIGURES

LIST OF FIGURES
(Continued)

LIST OF FIGURES
(Continued)

LIST OF FIGURES
(Continued)

Figure **Page**

CHAPTER 1

INTRODUCTION

1.1 Motivation

With the ever increasing need to process data faster, the continuously evolving silicon industry seeks routes to circumvent the inadvertent RC delay in metallic interconnects of the modern day integrated circuit (IC). The adoption of a functional approach by the multi-billion dollar microelectronics industry towards this end necessitates that any solution be compatible with the current IC fabrication process. The integration of mainstream electronics with on-chip optics, with its inherent advantage in computing speed, is therefore, an aggressively pursued goal [1].

Over the last 20 years, several strides have been made in the engineering of group IV semiconductor nanostructures. Silicon, being an indirect bandgap material by nature, is inherently a poor light emitter in bulk form. Nanostructures based in silicon however, with their partially relaxed momentum-conservation rules, have opened a new degree of freedom in the engineering of improved quantum efficiency (QE) light-emitting devices. Porous silicon, superlattices of silicon and silicon-germanium alloys, silicon nanocrystals, and multilayers of silicon thin films and silicon-germanium clusters (also known as Si/SiGe three-dimensional (3D) nanostructures) are examples of improved QE group IV nanostructures that are also compatible with the IC fabrication process. In many of these materials, the photoluminescence (PL) QE falls drastically under high levels of photoexcitation. The primary reason for this is the onset of the non-radiative Auger

recombination process at high carrier concentrations. With reduced physical dimensions in nanostructures, the problem gets even worse as the concentration threshold of these processes is also lowered [2]. Thus, any improvement in QE gained by scaling is sustained over a smaller range of carrier concentrations. This makes it imperative to study the physics of Auger processes in low dimensional nanostructures.

1.2 Objective and Scope

The objective of this experimental study is to understand the mechanisms of recombination in two group IV semiconductor nanostructures (Si, Ge). Specifically, Auger recombination and photoluminescence in the silicon/silicon-germanium 3D nanostructure system and in the silicon-on-insulator (SOI) system are investigated. Since the PL QE in these systems decreases at high carrier concentrations, the study focusses on phenomena that occur in this regime of carrier concentration.

1.3 Contribution of Research

Recombination mechanisms are studied by several experimental techniques. One approach explores the steady state PL spectroscopy and PL dynamics under pulsed excitations with varying concentrations of photo-generated charge carriers in the investigated systems. Another important technique uses selective, wavelength dependent photoexcitation to generate carriers up to varying depths in the nanostructures, enabling the understanding of local differences in PL properties through the thickness of structures.

Several interesting observations are reported and underlying recombination mechanisms are discussed. For the Si/SiGe 3D nanostructure system, these include an Auger Fountain mechanism that redistributes charge carriers within the nanostructure, a severe reduction of the exciton diffusion length, and a reversible degradation of the PL after a few minutes of relative stability. For the SOI system, an apparently successful competition of the radiative recombination of carriers in a condensed excitonic phase with Auger processes is observed near the Auger concentration threshold. The influence of the Si/SiO_2 interface on the recombination mechanism in this system is emphasized. Results of the experiments show that the coexistence of a type II energy band alignment at Si/SiGe interfaces, the electron-hole-droplets in Si, and Auger-mediated processes results in several unusual photoluminescence properties in SiGe and Si nanostructures.

1.4 Organization

Chapter 2 of this dissertation summarizes background information relevant to material and inferences made in later chapters. Chapter 3 details experimental samples and techniques used in this study; it also presents estimates of parameters used to interpret data from experiments in Si/SiGe 3D nanostructures. Chapters 4 and 5 present results of experiments, and discuss recombination mechanisms in the Si/SiGe nanostructure system and the SOI system, respectively. Chapter 6 lists various interesting conclusions made from presented work.

CHAPTER 2

BACKGROUND

The sizeable experimental and theoretical knowledge-base on Silicon and other group IV materials and structures enables an assessment of their light emission characteristics. With the ability to create low dimensional structures using various processing techniques, it is possible to experimentally compare photoluminescence characteristics in bulk material to those in micro- and nano- scaled structures. In the following sections, a summary of the current understanding of properties relevant to light emission from bulk group IV materials and their nanostructures is presented. An overview of recombination processes in these materials and questions worthy of consideration are posed. Since Auger processes play a pivotal role in the recombination mechanisms in all of these materials and structures, this chapter begins with a brief introduction to Auger recombination.

2.1 Introduction to Auger Recombination

When an electron and a hole are created in a system, it assumes an energetic state; subsequent recombination restores the system to its ground state. The energy of the system is conserved in the recombination process via one of several mechanisms, the most common ones being the emission of quanta of heat and/or light. Auger recombination occurs when this energy is transferred instead, to a charge carrier.

Resulting from an interaction between carriers, this is a non-radiative process wherein the energy from recombination between an electron and a hole is equal to the energy transferred to one or more charge carriers. Besides energy, momentum is also conserved. The energetic third carrier could be an electron or a hole and requires the availability of a higher energy state, which it occupies upon "ejection". Text books quantitatively analyze Auger process using wave mechanics to predict the location or momentum of the third particle [3].

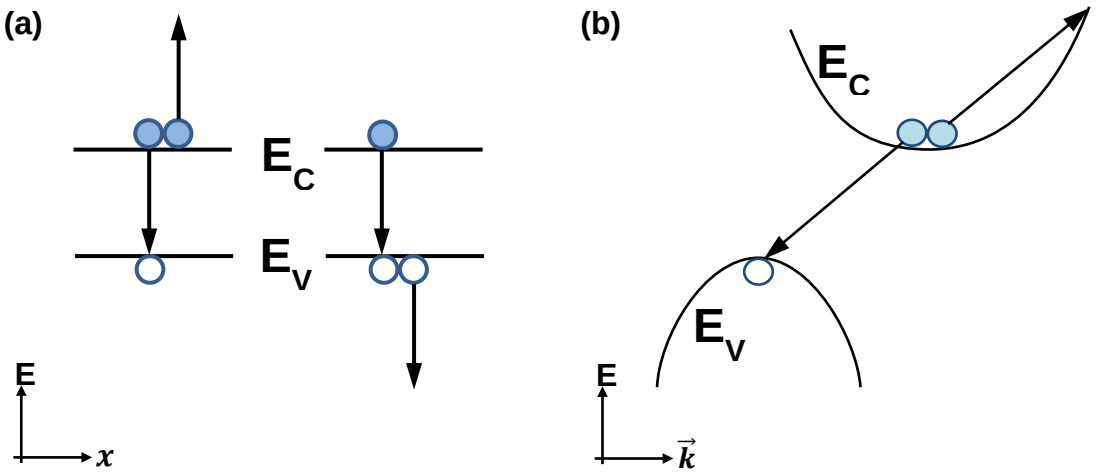

Figure 2.1 Depiction of the basic three-particle Auger process in (a) real space and (b) momentum space. The "hot" carrier may be an electron (solid circles) energized from the conduction band minimum or a hole (hollow circles), energized from the valence band minimum, to a higher energy state, as shown in (a). Both energy and momentum must be conserved, as shown in (b).

The relaxation of the ejected carrier (and therefore, of the system to the ground state) can occur via several processes, the most common being intravalley thermalization.

In this process, the excited state of the carrier lies within the native energy valley of k-space and energy is conserved via the emission of phonons. This common situation is represented in Figure 2.2 for the case of Si [4].

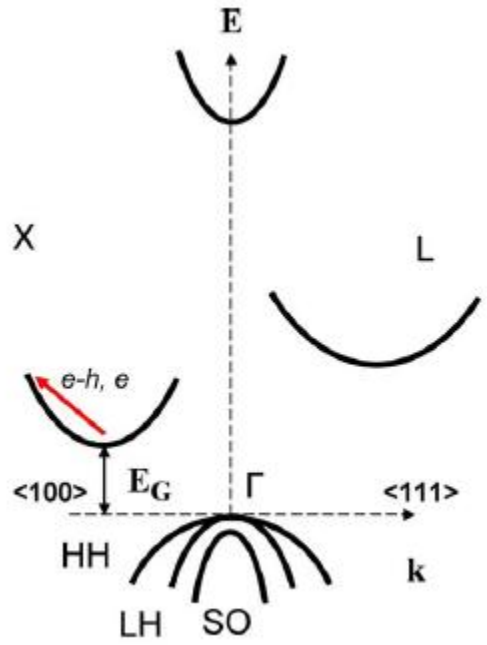

Figure 2.2 Energy-momentum diagram of bulk Si showing the basic Auger process in momentum space [4]. Intravalley thermalization of an Auger electron from a higher state in the same valley occurs by relaxation via phonon emission.

Another possible fate of the ejected carrier is intervalley transfer, wherein the carrier is transferred from one energy valley of k-space to another valley. An example of this is seen in bulk germanium [4], shown in Figure 2.3. In both these cases, relaxation of the ejected carrier to the minimum of its k-space energy valley is accompanied by phonon

emission, and momentum is conserved in the process. Intervalley transfer of carriers however, requires a large change in momentum, which makes it a rare event.

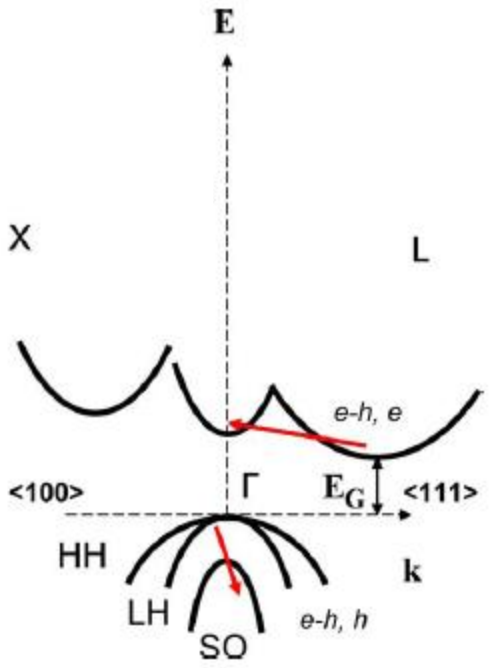

Figure 2.3 Energy-momentum diagram of bulk Ge showing the basic Auger process in momentum space [4]. Intervalley transfer of an Auger electron (or hole) from one valley occurs via excitation to another valley.

The above process is typical of elemental bulk materials and their alloys. More recently, it was shown that in heterosystems with significant spatial confinement of carriers in one material, ejected carriers can physically transfer across energy barriers in *real* space and recombine in the material across the interface. This process of carrier ejection and transfer in real space as a result of an Auger process is called an Auger Fountain [5, 6], and can lead to radiative recombination of the ejected carrier with the

oppositely charged carrier in the higher bandgap material. Such Auger-mediated energy upconversion was originally demonstrated for a GaAs/GaAsP (III-V) system [5] and has been subsequently reported for group IV systems [6]. It is strongly dependent on properties of the interface including energy band alignment, energy band offsets, abruptness, etc.

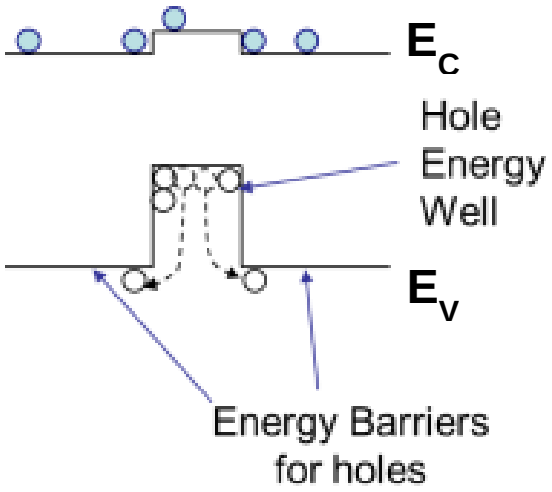

Figure 2.4 Auger Fountain at a Type II Heterointerface. Carriers ejected by an Auger process may overcome energy barriers and spatially transport across heterointerfaces. Strong carrier localization at the interface enhances carrier interaction; "ejected" carriers may recombine radiatively outside the potential well.

Auger processes depend on the availability of charge carriers per unit volume and occur only at high concentrations in bulk material. This is because carrier interaction does not become important until their concentration threshold for Auger recombination is met and sustained in the system. In the simplest case, three particles are involved; the rate of carrier loss shows a cubic dependence on the total concentration of free carriers. The time

scale at which the process occurs is on the order of 10^{-8} s, which typically makes it the dominant mechanism of electron-hole recombination once the carrier concentration is above threshold. Although Auger ejected carriers are not restricted, in principle, to any particular relaxation path, non-radiative recombination is typical, and Auger-mediated radiative recombination is seen only under special conditions in specifically engineered systems.

2.2 Light Emission in Group IV Macro-scale Structures

Group IV semiconductors are poor light emitters. The energy structure of group IV semiconductors, being indirect bandgap in nature, poses the requirement of the participation of a momentum-conserving phonon in the electron-hole recombination process. This produces a low quantum efficiency (QE) of radiative transitions and therefore, inferior light emission characteristics. In bulk Si, for example, the internal QE of phonon-assisted radiative transitions is lower than 10^{-3} [7].

Spectral features of the photoluminescence (PL) in bulk Si were known in the 1960s. At low temperatures, photogenerated electrons and holes form excitons and recombine via several phonon-assisted transitions that give rise to a characteristic spectrum with peaks at well-known energies; an example spectrum of their luminescence in Si [8] is shown in Figure 2.5. Alloying of materials changes their energy structure (k-space), leading to a partial relaxation of momentum conservation rules, and increasing the probability of phonon-assisted or even phonon-less radiative transitions [9]. The ratio of phonon-less transitions to phonon-assisted transitions was seen to increase with Ge

content in bulk SiGe alloys. This was also accompanied by a shift in the PL peak energies, with higher Ge alloys showing red spectral shifts.

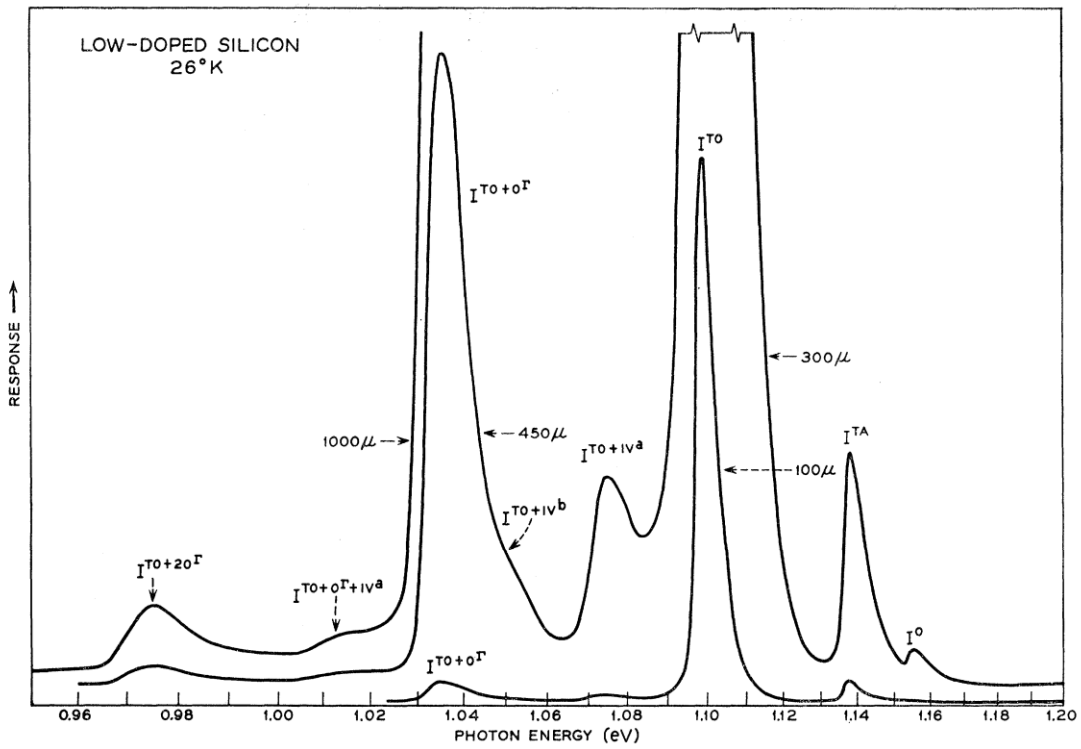

Figure 2.5 Low temperature PL spectrum of Si doped with 2×10^{14} cm^{-3} of P atoms (after [8]).

In systems where carriers are strongly localized, for example, by doping with a deep level impurity, momentum conservation rules may become relaxed, as can be seen via the uncertainty principle, illustrated in Figure 2.6. Complexes of Nitrogen/Carbon in Si with isoelectronic traps introduced in the lattice producing sharp PL peaks are an example [10]. Thus, strong localization can lead to a higher PL QE.

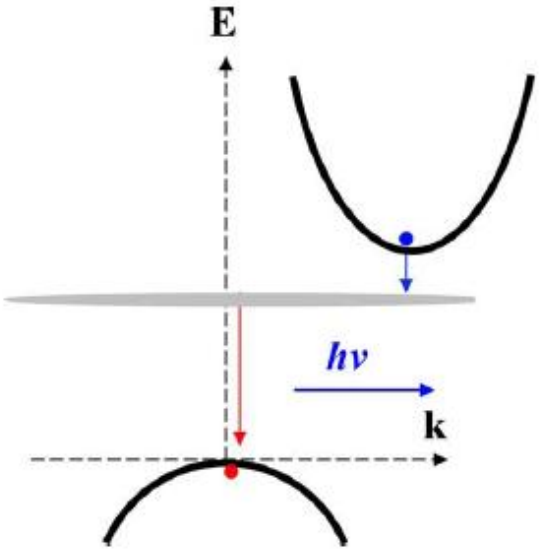

Figure 2.6 E-k mapping for a strongly localized carrier in an indirect bandgap semiconductor with isoelectronic impurities that introduce a deep level trap state. Momentum is not well-defined across the Brilluoin zone [4].

At high carrier concentrations, recombination may occur via two important phenomena. It is seen that at high concentrations and temperatures above 26 K, the quantum efficiency of the luminescence drastically reduces even in low defect density material due to the onset of non-radiative Auger recombination. At low temperatures (< 26 K for Si, 6.5 K for Ge) however, electron-hole pairs form the electron-hole liquid (EHL), which is the subject of Section 2.4, and subsequent carrier recombination in the EHL is radiative and fairly efficient. The phase diagram of electron-hole pairs in Si shown in Figure 2.7 shows various phases, including that of the liquid.

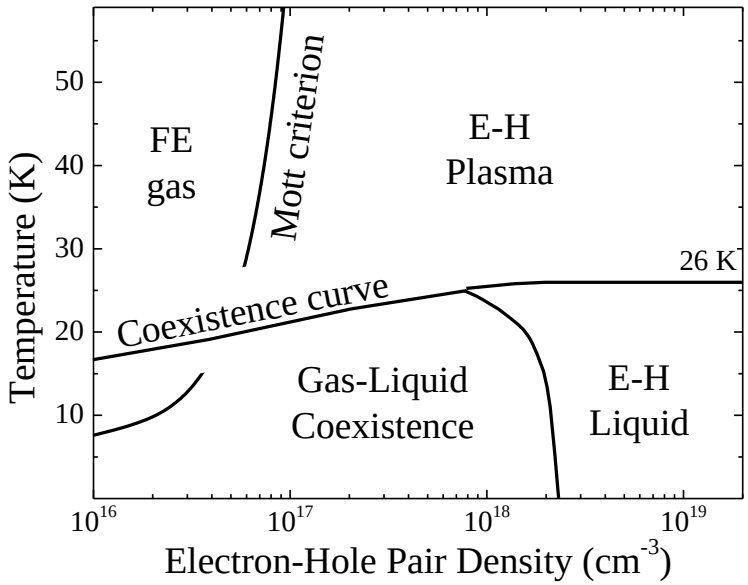

Figure 2.7 Phase diagram of electron-hole (EH) pairs in Si. At low temperatures, carriers can form excitons and exist as a gas of free excitons (FE), as a plasma at higher concentrations, or condense into a liquid at even higher concentrations and lower temperatures (< 26 K). Note the logarithmic horizontal scale.

Both short lifetime recombination processes in Si have concentration thresholds that are also close to each other: 3.3×10^{18} cm^{-3} for Si [11], 2×10^{17} cm^{-3} in Ge [12] for EHL condensation, and ~ 10^{19} cm^{-3} for Auger recombination. A possible competition between the two is of interest.

2.3 Light Emission in Low Dimensional Structures

Group IV materials in bulk form are poor light emitters; nanostructures of group IV materials show enhanced emission characteristics, generally attributed to the partial relaxation of momentum-conservation rules at reduced physical dimensions. Although the probability of radiative band-to-band transitions is enhanced, there is also a concurrent reduction in the threshold for carrier interaction due to spatial confinement of

carriers. This may lead to a loss of carriers via Auger recombination. In the absence of surface- or defect- related non-radiative recombination channels, radiative recombination competes primarily with Auger recombination.

Recombination at an interface is particularly interesting. An abrupt heterojunction in a bulk material could be considered a low dimensional structure if it strongly localizes carriers. With a large spatial change in lattice order, the energy band structure of the material changes dramatically at the interface. Interfaces play an especially significant role in nanostructures because the surface- (or interface-) area to volume ratio of the structure is enhanced by several orders of magnitude. Therefore, the energy distribution of carriers localized in such a structure is significantly influenced by the properties of the material across the interface. This has a striking advantage in that it opens a new degree of freedom in the engineering of systems by utilizing the properties of the interface. The disadvantage however, is that interfaces, which are particularly prone to defects, have to be closer to perfect than in macro-scaled structures: even a single interface defect can drastically reduce or even eliminate all radiative recombination in a nanosystem [13].

In order to be useful, interfaces must retain epitaxial quality (crystallinity) of the material and have an acceptably low defect density. For the Si-Ge system, the pseudomorphic growth of crystals to produce a lattice that stays ordered, can be optimized to control their abruptness and also to filter dislocations. The study of electron-hole recombination at or mediated via the interface in defect free nanostructures, then enables further study of the changes to the energy-momentum space. On the basis of the natural alignment of energy bands of the materials across spatial boundaries, interfaces

are classified as Type I (spatially direct) and Type II (spatially indirect), illustrated in Figure 2.8.

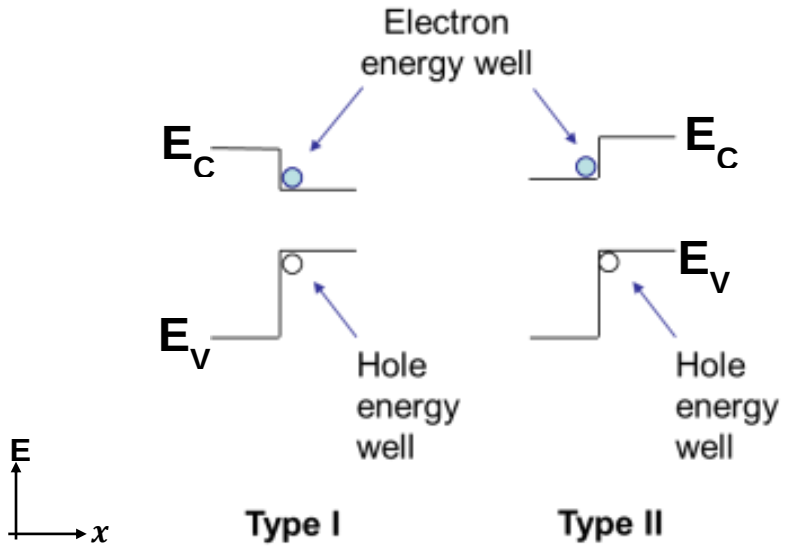

Figure 2.8 Definition of Interface Types. At Type I interfaces (straddling), electrons and holes localize in the same material, whereas at Type II interfaces (staggered), they are spatially separated into different materials.

Recombination mechanisms strongly depend on the Type of the interface, which sets the physical proximity of one type of carrier to another. When a material is spatially restricted by forming interfaces with a different material, narrow potential wells can be created. Type I interfaces form potential wells that favor the localization of electrons and holes in the same material, whereas wells across type II interfaces favor their localization in different materials. This description is based on the distribution of energies across

interfaces in real space. The partial disordering of lattice locations for atoms can lead to very significant changes in momentum-space, to the extent that energies in k-space cannot be mapped easily. This is particularly true for nanostructures with dimensions that approach the radius of Bohr excitons in the material; in those cases, momentum-conservation rules are relaxed even further and the probability of radiative transitions increases [14].

For structures with dimensions less than the Bohr exciton radius, the quantization of energy levels and quantum confinement plays a central role in determining their optical properties. This work does not study structures at these physical dimensions. As in recombination events in the bulk of materials, both energy and momentum have to be conserved at the interface, i.e., both vertical and horizontal neutrality of an entire excitation-deexcitation process is required on an E-k diagram. The momentum-conservation requirement enhances the probability of Auger events because carriers that need a large amount of momentum to transition to a higher state are unlikely to make such a transition and occupy their current energy valleys for longer durations, with increased vulnerability to Auger events.

An interesting observation in nanostructures with a type I interface is the “blinking” of the photoluminescence (PL) intensity. It manifests itself as PL that randomly turns ON and OFF, seen in individual quantum dots (QDs) made of II-VI materials. Figure 2.9 shows reported blinking [15].

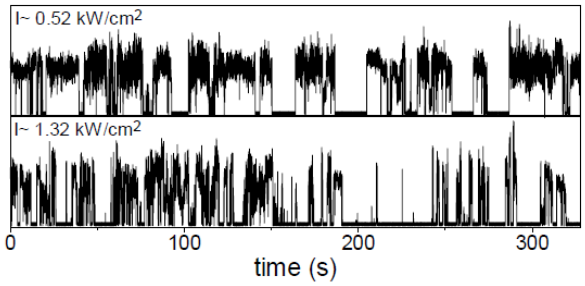

Figure 2.9 Comparison of PL ON/OFF behavior of an individual QD versus time under different excitation intensities. More intense excitation results in shorter ON periods [15].

Experimentally, while this phenomenon is observed as an intermittency of the PL from single nanocrystals, it renders itself as a degradation of the total PL intensity from an ensemble of nanocrystals, as shown in Figure 2.10. This degradation from macro-scale experiments have been correlated to the statistical difference between the ON and OFF times from experiments on individual dots; a histogram used for such an analysis [16] is shown in Figure 2.11. Qualitatively, it is understood that a carrier ejected due to an Auger event enters a transport pathway, wherein it occupies a trap state in the host matrix of the QD system, spends a finite period of time and transports back into the QD. While the carrier is out of the QD, the QD is not electrically neutral and therefore cannot continue radiative recombination of electron-hole pairs that are generated, i.e., it is OFF. Once neutralized, the QD may emit again; the period for which a typical QD stays OFF is longer than that during which it stays ON (seen in the histogram of Figure 2.11), explaining the gradual decrease of PL intensity from an ensemble of QDs.

The phenomenon, attributed to Auger autoionization of single quantum dots [15-21] based on experiments under varying photogenerated electron-hole pair

concentrations, has not been observed in nanostructures with a type II band alignment, assumed at Si/SiGe heterointerfaces. The kinetics of the PL degradation of the two systems, II-VI quantum dots (QD) and Si/SiGe nanostructures however, with their experimental differences, exhibit similar characteristic times. This raises the question of the possibility of a fundamental connection between Auger processes in II-VI QD systems and Si/SiGe nanostructures, and their possible contribution to PL degradation seen in these systems.

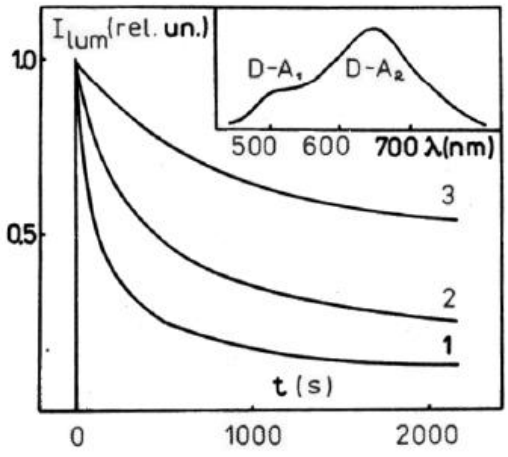

Figure 2.10 PL kinetics in an ensemble of QDs showing degradation under different excitation intensities. More intense excitation, indicated by numbers 3, 2, and 1 respectively, resulted in accelerated degradation. The inset shows a typical room temperature PL spectrum of CdS-in-glass QDs [17].

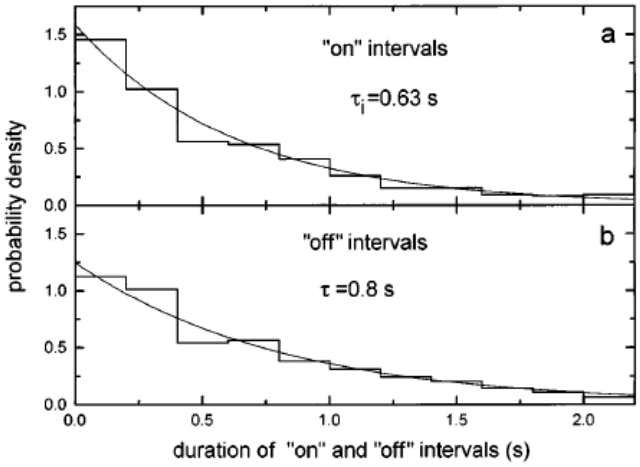

Figure 2.11 Distribution of the ON and OFF periods obtained by simulations of "PL blinking". In these histograms, time bins of 0.2 s durations are used. Curve fitting extracts characteristic ON and OFF times [16].

2.4 The Electron-Hole Liquid

The discovery and initial experimental study of the EHL were done in the late 1960s and early 1970s, on Ge crystals with the purity of the time. Under very high carrier concentrations, strong carrier-carrier interaction was found to change the phase of EHPs from a gas of FEs, to a degenerate, free-flowing, distinct liquid condensate of electrons and holes that showed metallic properties [22]. Subsequent experiments showed the existence of the EHL in Si [11] and even SiGe [23]. It was found to be electrically neutral as a unit. The liquid was shown and found to be more stable in indirect energy bandgap systems than in direct bandgap materials [24]; even more so in Ge than in other group IV semiconductors [25]. As a result, Ge was popularly used to investigate the properties of the liquid, and even today, more is known about the EHL in Ge than in Si. What is now known as the condensate luminescence in Si, was originally misinterpreted to be due to

the recombination of biexcitons [26] and corrected later [27], only after investigations in Ge lead to the demonstration of the liquid phase of charge carriers.

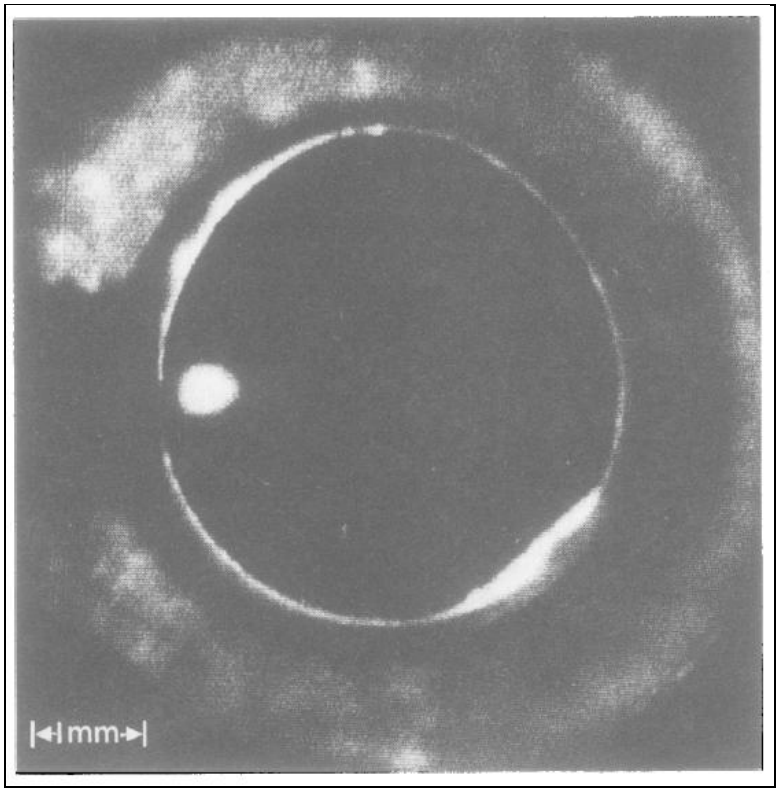

Figure 2.12 The first photograph of a long-lived EHL drop in Ge [28]. The drop is the bright spot towards the left on the 4 mm Ge disk, a position it occupies because the screw that fastens the disk to the sample holder creates a potential well due to strain in that region.

Depending strongly on excitation intensity, EHL drops can have a radius of hundreds of μm, as the one shown in the infrared photograph of Figure 2.12 [28]. In most quantitative studies, drops are assumed to be spherical [12, 27, 29-31], and are free to flow unrestricted in a pure crystal. They are accelerated under strain gradients, and flow

towards the location of maximum strain (minimum energy) in the crystal [31]. In Ge, they have a radiative lifetime of ~ 40 μs [29], while in SiGe, the reported lifetime is in the ~ 10 μs range [23]. There exists a critical EHP density for the condensation of EHPs into the liquid phase; for Ge, this is ~ 2×10^{17} cm^{-3} [12], for SiGe, ~ 5×10^{17} cm^{-3} [23], and for Si, this is ~ 3×10^{18} cm^{-3} [11].

EHL drops in a semiconductor are generally created by exciting it with an intense light pulse and the kinetics of their decay are studied by recording their luminescence after the excitation is turned off. They are formed within nanoseconds, and then decrease in size mainly due to recombination and evaporation. Several interesting dynamics of the PL during EHL decay have been observed, and are reviewed in Refs. [12, 32]. For example, the PL intensity is characterized by a "cutoff time", t_c, before which decay is not only complete, but also accelerates as it approaches this time. Numerical models that correlate this time to the shrinking drop radius have been developed by incorporating the strong dependence of cutoff on the temperature of the liquid, and on the number of EHPs in a single drop [29]. Thus unless the temperature of liquid is below ~ 2 K, decay curves are not exponential, but become steeper as t_c approaches.

An even more remarkable feature is the optical hysteresis of the concentration threshold for liquid formation. When excitation is monotonically increased, this concentration threshold is much larger than the threshold for monotonically decreasing excitation. In other words, nucleation of the condensate occurs at high EHP concentrations; once formed however, the EHL is sustained until much lower concentrations than the formation threshold. This manifests itself on the phase diagram of Figure 2.7, via two distinct branches of the coexistence curve, experimentally measured

by tracking these concentrations. Furthermore, the FE concentration shows correlated hysteresis, simultaneous with that of the EHL, but in the converse direction. The FE gas continues to get dense with increasing excitation until it is supersaturated (leading to EHL condensation), but does not proportionately dilute under decreasing excitation, until the EHL drops vanish (concentration falls below threshold). This is known from careful measurements performed on high quality Si [11] and Ge [33] crystals.

In liquid form, radiative recombination of EHPs is quite efficient and lifetimes on the order of 10^{-7} s have been recorded, thus becoming important competitors with Auger processes that also set in at high carrier concentrations. The requirement of phonon participation for recombination in both indirect bandgap semiconductors causes exciton lifetimes to be quite long, in the μs range, enabling the sustenance of the EHP population for the creation of liquid drops. In contrast, in direct bandgap semiconductors, phonon-less radiative recombination competes with that in the EHL, which is then more difficult to create and sustain. Also favoring the stability of the EHL in Si and Ge, are their crystal anisotropy and energy band degeneracy [12, 32]. Although restricted to low temperatures, the fast radiative recombination of EHPs in the EHL phase is then positioned to compete with Auger processes at high carrier concentrations, and is experimentally explored in this work.

2.5 The Physics of Recombination Processes in Low Dimensional Structures

The question of the importance of studying Auger processes is answered in this section. Regardless of the type of excitation, excited systems undergo processes to minimize the energy of the system. Recombination, which is the ground-state restoration mechanism in

semiconductors, most often involves processes that are not easy to observe. Radiative recombination can be recorded directly, but the inherent difficulty in studying non-radiative processes is that it involves mechanisms that manifest themselves by the absence of the expected byproduct. The construction of plausible models is then guided by circumstantial evidence rather than definite proof [34].

A balance equation describes the entire process of change in carrier concentrations with respect to time. It tracks the evolution of carrier concentration by algebraically adding the rates of recombination processes. The fastest process brings about the largest change in the concentration and is the rate-determining processes. An Auger process is quite often the fastest process in concentration regimes where carrier-carrier interaction is important, and therefore prevails as the dominant rate-determining non-radiative step for several systems. The decrease in quantum efficiency in high quality bulk Si and Ge samples is attributed to Auger recombination.

The alignment of energy bands at the heterointerface of two different materials changes localization of carriers. This in turn influences carrier interaction, which shows as either the enhancement or suppression of Auger rates. In addition, carrier scattering is enhanced at heterointerfaces. Scattering allows a change in the momentum of carriers to values forbidden in the bulk of the material, therefore enabling the conservation of momentum required for an Auger process. The increase in probability of an Auger event is reflected in the lowering of the carrier concentration threshold for Auger recombination in nanostructures (where heterointerfaces have a much larger surface area) than that in materials with larger dimensions. The lower threshold for Auger recombination in nanostructures, attributed to enhanced scattering at interfaces has been found

theoretically for type I quantum well systems [35]; group IV systems can be expected to show a similar behavior. This can lead to lowering of the PL QE at concentrations that are lower than the bulk Auger threshold.

Most interfaces in a nanostructure, as fabricated are abrupt to the extent required by the application and permitted by the growth process. When an interface is not sufficiently abrupt, localized carriers may form interface or surface excitons, but the overlap in their wavefunctions may not be significant. With lower carrier interaction, Auger rates may decrease, but with the concurrent decrease in radiative rates brought about by the limited wavefunction overlap. The abruptness of an interface is an important parameter as it influences localization and Auger rates.

The overlap of electron and hole wavefunctions referred to above, is also influenced by material dimensions of the nanostructure. For example, Figure 2.13 shows a typical Si/SiGe type II heterinterface; by designing either or both materials across the interface to be sufficiently thin, carrier localization may be significantly enhanced. A very thin film of a certain lattice constant grown between materials of different lattice constants is likely to be heavily strained. Strain brings about other changes to the system; in Si and Ge, it reduces the energy gap and lifts the degeneracy of energy bands, which further changes the optical properties of nanosystems in which these strained material are used.

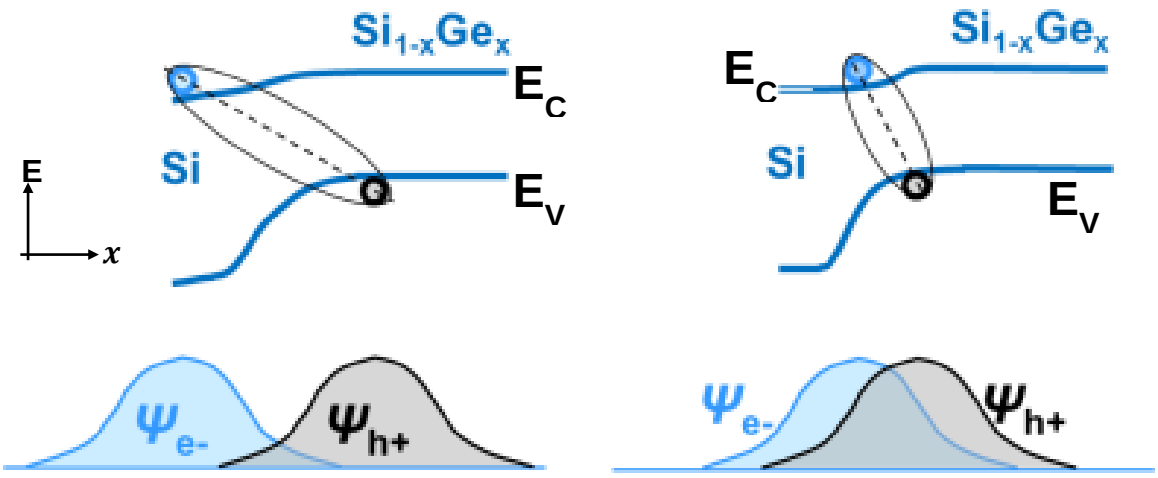

Figure 2.13 Schematic representation of interfaces between Si and SiGe with localized carriers forming an interface exciton. The possible overlap of the wavefunctions of an electron and a hole localized at an interdiffused (left) interface and a relatively abrupt interface is shown.

The pseudomorphic growth of Ge (lattice constant a = 5.658 Å) on Si (a = 5.431 Å), results in the development of intrinsic lattice strain due to the 4.2 % mismatch in these values. Since the growth is pseudomorphic (the tetragonal symmetry of both Si and Ge is distorted), the 2x mismatch in their thermal expansion coefficients is not important, as for amorphous or polycrystalline materials, and the effective strain upon cooling from process to room temperature is determined by the mismatch in lattice constants at room temperature. Also, capping layers on low dimensional structures such as thin films are known to change and even dominate over lattice strain in a fabricated device or structure. In fact, in current MOSFET devices, Si_3N_4 thin films on gate stacks over SiGe channels are commonly used to engineer strain for carrier mobility enhancement in these channels [36]. In the studied nanostructures, Si is used for capping (other materials present an interesting possibility for engineering lattice strain); strain is essentially purely intrinsic.

CHAPTER 3

EXPERIMENTAL

Experimental samples, their preparation, and techniques used in this study are described in this chapter. Estimations of quantities important for the analysis of results presented in subsequent chapters are also presented.

3.1 Sample Description and Preparation

Carrier recombination was studied in a Si/SiGe three-dimensional, epitaxially grown nanostructure system, and in a simpler Silicon-On-Insulator (SOI) thin film system. The Si/SiGe nanostructures were prepared at the Institute of Microstructural Sciences, National Research Council (NRC), Ottawa, Canada, on commercially available Si wafers. These are the subject of Section 3.1.1. Since luminescence properties of these nanostructures critically depend on strain in the multilayers, which is tailored by optimizing parameters directly during the growth process, relevant detail of the physics of the epitaxial growth procedure is presented in Section 3.1.1.1. Besides growth procedures, this section briefly presents information relevant to dislocations, Si/Ge interdiffusion, and strain distribution produced in pseudomorphically grown Si/SiGe structures; these ideas are used in later discussions. Electron microscopy was used, also at NRC, to study structural properties of the crystalline nanostructures; a brief description of the techniques used and notes on the interpretation of images produced are presented in Section 3.1.1.2.

SOI wafers were purchased from a commercial vendor and not processed further. Relevant detail of these wafers is presented in Section 3.1.2.

3.1.1 Si/SiGe Three-Dimensional Nanostructures

Si/SiGe three-dimensional nanostructures are comprised of alternating crystalline layers of pure Si and of islands of SiGe alloys, grown on a Si substrate. They differ from a superlattice by virtue of the three-dimensional morphology of their SiGe clusters, as opposed to the flat morphology of SiGe layers in superlattices. The clusters are dome-shaped islands and the surface of a layer of clusters shows a continuous, undulating morphology. Pyramid shaped clusters with sharp edges have also been produced, but are not investigated in this work; these have been observed to have less intrinsic lattice strain than domes, which typically have 1.5 to 2% strain. By an analysis of the thermodynamics of the growth process, the period of the undulations has been characterized [37], and for the growth process used, is essentially the same as the base dimension of the islands. Thus, boundaries of adjacent clusters touch each other, within each SiGe cluster layer of the nanostructures. The use of multiple cluster-layer pairs allows for a substantial increase in the total volume of 3D morphology, which furthers their technological importance.

The base dimension of the clusters in the nanostructure is ~ 70 – 100 nm and their height is typically ~ 8 nm. The Si “spacer” layers are also typically about 8 nm thick; their top surface is almost completely planar, even while being grown on undulating cluster layers. The growth of Si spacers is preferentially faster between clusters than regions directly above. This is because vertically above the crest of the islands, the lattice

constant of the underlying structure is closer to that of Ge, than it is in the troughs [37]. The surface diffusion of Si atoms is naturally driven by a lower strain energy between clusters (biaxial compressive strain in these regions is comparatively less), and ~ 8 nm thick films show sufficiently good planarity.

The surface of Si films is modulated by the strain field from the underlying cluster layer. This enables preferential nucleation of the growing clusters at sites of maximum strain, i.e., directly above the centers of underlying clusters [38]. Thus, Si spacers separating cluster layers, facilitate vertical alignment through the multilayered structure, provided their thickness is kept low enough for penetration of the SiGe strain field. All samples are capped with a Si thin film to prevent natural oxidation of clusters. A dark-field cross-sectional TEM image of a typical nanostructure is shown in Figure 3.1.

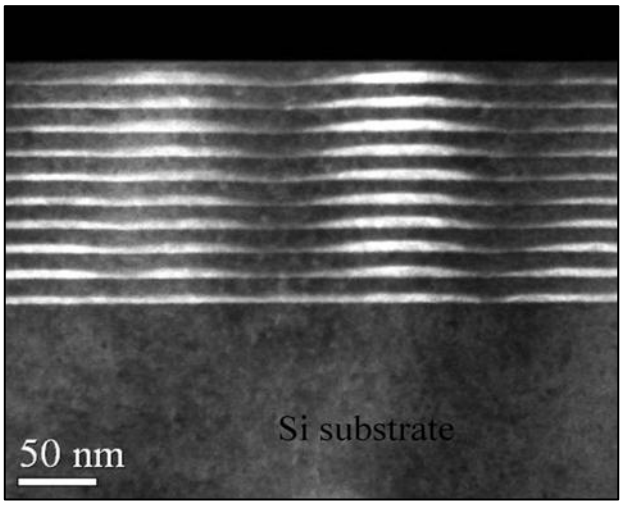

Figure 3.1 A cross-sectional TEM dark field image of a typical Si/SiGe three-dimensional nanostructure showing 10 pairs of SiGe clusters and Si layers, grown on a Si (100) substrate. The pancake-shaped clusters (bright regions) are 7 – 10 nm in height, 70 – 100 nm in base diameter, and separated from subsequent clusters by Si thin films (dark regions).

The areal density of islands in each SiGe layer is an estimated ~ 10^{10} cm^{-2}. Although clusters are dome- shaped, assuming a pyramidal shape with a square base simplifies the estimation of their surface area and volume, while only slightly underestimating their values. The surface area of each cluster is simply the sum of its base area (100 nm × 100 nm) and the combined area of the triangular facets of the pyramid (4 × ½ × 100 nm × $\sqrt{2600}$ nm), and is approximately 2.02 × 10^{-10} cm^2. The volume is easily calculated by assigning variables to cluster dimensions, as shown in Figure 3.2, and integrating between their respective limits. The expression in Equation 3.1, developed using Cartesian coordinates in nanometer units, calculates the volume of a single nanocluster to be 0.66 × 10^{-16} cm^3. These physical parameters are used for rate calculations associated with charge accumulation in clusters, detailed in Chapter 4.

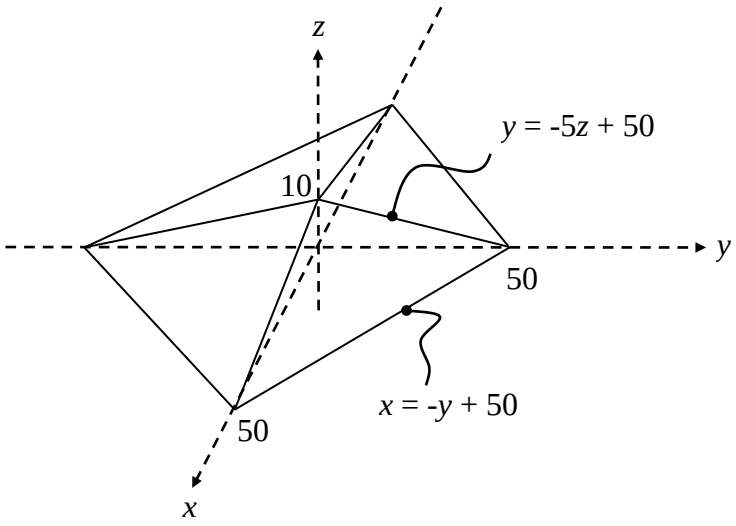

Figure 3.2 A schematic of a pyramid-shaped cluster defined in a Cartesian system to visualize variables used in estimations of the surface area and volume of a single SiGe cluster. The numbers have units of nanometers.

$$\text{Volume} = 4 \times \int_0^{10} \int_0^{-5z+50} \int_0^{-y+50} dx\, dy\, dz \tag{3.1}$$

Several luminescence characteristics of these nanostructures depend on the composition of the clusters and the properties of Si/SiGe heterointerfaces. Samples with different Ge content in the clusters and varying extents of intermixing of Si and SiGe at the interface were used to investigate different recombination mechanisms. Relevant physical properties of these samples are described in Table 3.1. These samples are called A, B, and C, in the rest of this dissertation. Samples A and C were designed to have SiGe cluster layers and Si spacers, both of thickness ~ 8 nm at cluster centers. This ~ 16 nm thickness of a single "standard" cluster-layer pair was kept uniform through all such pairs in the nanostructure, with 10 standard pairs in sample A with ~ 16% Ge, and 5 standard pairs in sample C with ~ 40% Ge in the clusters. A nanostructure with a higher Ge content, ~ 55%, but a design otherwise identical to that of sample A, has been previously investigated [6, 39]; though not listed here, it is used for comparison with experimental results from sample A in Chapter 4.

Table 3.1 Description of Si/SiGe Three-dimensional Nanostructure Samples used in this Dissertation

Sample	Approximate Ge content	Number of cluster-layer pairs (cluster-layer thickness)
A	16%	10 (~ 8 nm – 8 nm, Uniform)
B	40%	9 (Non-uniform)
C	40%	5 (~ 8 nm – 8 nm, Uniform)

The nanostructure of sample B was designed to engineer strain at interfaces at the top of the nanostructure, by changing the thickness of constituent layers. A standard cluster-layer pair was grown on a Si (100) substrate. It was followed by a pair with a ~ 8 nm SiGe cluster layer, but a 30 nm thick Si spacer. This was used to qualitatively understand, via TEM imaging, the strain distribution in a spacer with larger than standard thickness (contrast features in spacers of standard thickness overlap with each other, making it difficult to visualize the strain gradient). Using a 30 nm thickness does not affect the vertical alignment of clusters, in agreement with Ref. [40], and also seen in TEM images of the sample. Five standard cluster-layer pairs were then grown. These were followed by a layer of larger SiGe clusters, with a height of ~ 18 nm, and then a much thinner Si spacer of 3 nm thickness, an ~ 8 nm layer of SiGe clusters, and a final ~ 6 nm thick Si capping layer.

3.1.1.1 Relevant Aspects of Growth. A Vacuum Generator Semicon V80 MBE system was employed to prepare Si/SiGe NS samples studied in this work. A base pressure of 5×10^{-11} mbar, growth temperatures of about 650°C, and flow rates corresponding to a combined Si and Ge growth rate of ~ 5 $Å s^{-1}$ were used to produce the

SiGe clusters. Samples were characterized by various techniques to ascertain crystalline integrity, defect density, structural, stoichiometric, and compositional properties of the grown structures. The findings have been previously reported [41]; only techniques relevant to the current study are discussed in this dissertation.

Fundamental to the process of SiGe island formation is their self-assembly in a controlled environment. A balance between the surface mobility of atoms and the growth rate of SiGe clusters determines their properties and those of their interfaces with Si. Their nucleation requires a clean surface free of native oxides, and occurs within the 600 – 700 °C temperature range. Physical Vapor Deposition [42], Chemical Vapor Deposition [43], and Molecular Beam Epitaxy (MBE) [37, 41, 44, 45] are among the popular processing techniques that have been used to realize these conditions. Temperature is a primary variable in these processing studies, and it emerges that the epitaxial integrity of the nanostructure is compromised by lowering the temperature. Although good crystallinity in SiGe thin films has been achieved for temperatures as low as 150 °C (references in [41]), the growth of epitaxial islands with high Ge content occurs only above 600 °C. At higher temperatures, surface diffusion of atoms results in the reduction of the three-dimensional nature of the growth, and smoother, intermixed SiGe layers are obtained. At the temperatures used, surface diffusion of atoms is too slow to compete with three-dimensional growth. Growth rates less than about 10 $Å s^{-1}$ are generally needed to achieve good crystallinity. An extremely low base pressure is necessary not only to reduce contamination, but also to increase the mean time between collisions of the depositing species [46] in the MBE chamber.

In an attempt to create virtual SiGe substrates to utilize the enhanced carrier mobility of strained material for device applications, the pseudomorphic growth of SiGe on Si to produce Si/SiGe superlattices were extensively investigated, starting in the 1980s [41, 47, 48]. Temperature limits for 3D growth for the entire range of Ge compositions in SiGe were experimentally found [47]. It was found that under specific conditions, the propagation of dislocations in the growth direction could be restricted to Si/SiGe interfaces [48]; hence, superlattice-type structures came to be also known as dislocation filters. The understanding of the mechanism of the propagation of dislocations meant that device quality SiGe layers could be grown simply by optimizing growth parameters. Consequently, strain relaxation in device layers via distortion of their tetragonal lattice symmetry rather than plastic deformation, realized pseudomorphic growth of thick SiGe films on Si substrates. Threading dislocations induced during growth were found to stay within the substrate, and propagate along (111) planes in the substrate. The energy band offsets at the Si/SiGe interface for the valence band were found to be large compared to those for the conduction band [49].

The formation of SiGe islands proceeds via the Stranski-Krastanov growth mode, involving the initial formation of three monolayers of Ge atoms, followed by the growth of 3D islands, schematically represented in Figure 3.3. Features of this growth mode are summarized below, following material from Ref. [37]. It starts with a monolayer-by-monolayer growth of Ge on the lattice-mismatched Si substrate, with continuously increasing surface energy and strain energy in the Ge film. Beyond a critical value, strain energy is released at the expense of surface energy via the nucleation of islands, allowing for an elastic relaxation of substrate planes towards island peaks. The maximum

relaxation occurs at locations that are separated by a characteristic distance, about 100 nm for the Si/SiGe 3D system. The layer grown up to the thickness producing the critical strain energy is called the Wetting Layer. Moderate temperatures are an important feature of this growth mode. At higher temperatures, strain energy is too low to compete with surface energy (strongly temperature dependent), and layer-by-layer growth is energetically favored. At lower temperatures, material crystallinity is compromised; polycrystalline films and eventually amorphous films are formed as the growth temperature is lowered. Low temperature epitaxial growth with low dislocation densities is relatively challenging. With increasing temperature, defect-free epitaxy starts with island + layer growth (via Stranski-Krastanov growth mode), and leads to layer growth. For the Ge/Si system, temperatures for this growth mode lie in the 550-700 °C range.

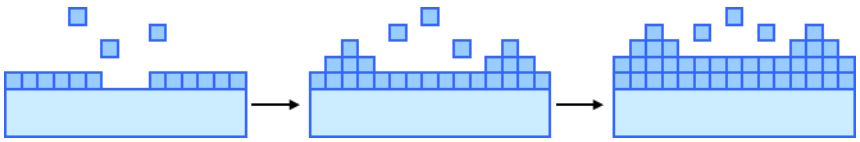

Figure 3.3 Schematic Representation of the Stranski-Krastanov Growth-mode.

The evolution of the shape of islands involves the formation of two-dimensional platelets, followed by pre-pyramids; further deposition yields square or rectangular pyramids with side walls oriented along the <105> planes [42], and eventually larger dome-shaped islands with steeper facets in the <113> or <111> planes.

Interdiffusion of Ge/Si creates smoother compositional transitions, is a function of temperature and time, and reduces the abruptness of interfaces in the nanostructure.

While all layers of the nanostructure, including both SiGe clusters and Si layers, are grown at the same temperature, those at the bottom of the nanostructure are subjected to longer durations at the growth temperature than those near the surface. It is expected that interfaces lower in the nanostructures are more interdiffused than those near the surface. During the growth of SiGe islands, alloying is influenced by the atomic diffusion of Si atoms from the underlying structure into the islands. This produces trenches at the base edges of the islands and is driven by the strain gradient below base edges [50]. During the growth of the Si films, a slight intermixing of Ge from the islands into the growing Si layer is seen in the lateral direction. The presence of Ge atoms in overlying Si films has been verified by various techniques [51, 52], results in the reduction of the nominal Ge content in clusters, and increases the compressive strain in the Si regions in valleys. For larger clusters (as in sample B), the outdiffusion of Ge atoms is expected to be relatively high.

Strain in the nanostructure is best measured by electron microscopy techniques, described in the next section, is also well correlated to and estimated by optical techniques [52]. Quantitatively, the distribution of strain in the nanostructure can be calculated by a superposition of strain induced by individual layers, at any given point in the nanostructure. This can be done using the highly anisotropic linear elastic moduli of Si and Ge in a finite element calculation in the growth direction [38, 53]. It emerges layers higher in the nanostructure, change gradients and absolute values of strains not only in lower layers, but also near the surface of the substrate.

3.1.1.2 Imaging Techniques. Micrographs of Si/SiGe nanostructures were obtained using a JEOL JEM-2100F field emission source Transmission Electron Microscope (TEM), operating at ~ 200 – 300 kV. Cross sectional TEM images were obtained along the <110> plane, in the bright and dark fields, including those meeting a two beam condition (explained below) along <200> planes. Analytical TEM imaging performed at select locations in the nanostructure, provided information about the local Ge content. Samples were cleaved along the [110] direction, thinned initially by mechanical dimple grinding and then by Argon ion beam milling procedures, and were uniformly 50 – 60 nm thick.

The interpretation of images obtained by electron microscopy requires an understanding of how images are acquired; the following notes very briefly summarize concepts necessary to interpret images used in this work and follow material from Refs. [22, 54-58].

Elastic scattering of electrons incident on the thin structure that is the subject of investigation in a TEM is characterized by an extinction distance, which is the distance by which most electrons have had a chance to undergo one scattering event. All electrons exiting a crystalline sample, either transmit through it in the direction of the incident beam and are collected to produce a bright field image, or are redirected by at least one diffraction event and produce a dark field image. If samples are thicker than one extinction distance, scattered electrons have a relatively large probability of undergoing a second diffraction event, and can get realigned with the direction of the incident beam, intensifying the bright field image. Dark field images therefore, are most intense for samples that are thinner than the extinction distance (~ 100 nm for the energy used in this

study). Figure 3.4 shows an example of a bright field image, while Fig. 3.1 showed a dark field image; sample thickness was ~ 50 nm.

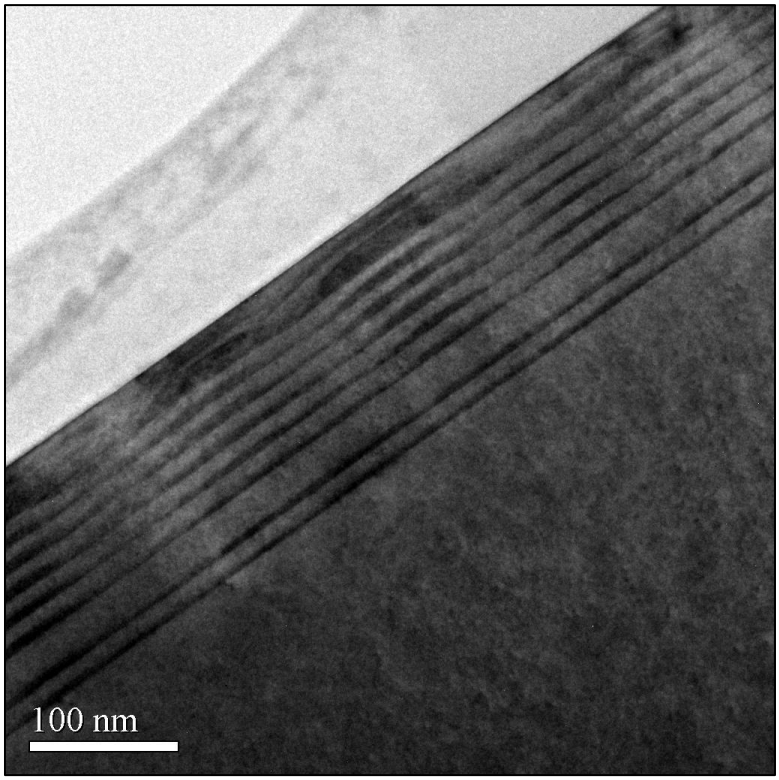

Figure 3.4 The TEM <011> zone axis bright field image of a strain-engineered Si/SiGe nanostructure showing 9 pairs of SiGe clusters and Si layers grown on (100) Si. One layer of clusters, second from the top, was made much thicker than others, and a much thinner (3 nm) Si layer was grown on it to alter the strain gradient in this cluster-layer pair.

Diffraction off individual planes in the sample can be further distinguished by orienting it such that electrons that diffract only along a plane of interest are allowed through the dark field aperture of the TEM. The image thus formed, called a two beam

image, reveals the structural properties of the specific “Bragg” plane. General interpretations are made by comparing images from several Bragg planes.

In an unstrained crystal free of defect clusters, diffracting electrons encounter identical lattice parameters in each successive Bragg plane. Also, basis atoms of a single Bragg plane repeat with a constant displacement vector. In a strained crystal, this vector changes depending on the magnitude of strain and the anisotropy of the lattice. A two beam TEM image is further complicated by differing lattice parameters in successive Bragg planes. Therefore, electrons diffracting off a region deep in sample encounter a different strain field compared to those diffracted off preceding planes. As they exit the sample, diffraction off regions with different lattice parameters can lead to the formation of an interference pattern in the two beam image, which can be analyzed to quantify the change in lattice constant (i.e., strain). This technique of using a two beam image showing an interference pattern was reportedly applied to quantify biaxial strain in individual, coherently grown Ge islands on (100) Si using top view TEM images [56, 57]. The authors analyzed interference patterns to infer that dome-shaped islands were significantly more strained than pyramid-shaped ones. In these experiments, the TEM electron beam was incident on the back surface of a sample, passed through an unstrained substrate, encountered a strain field due to a different lattice parameter in the <400> planes of the Ge islands, and produced interference fringes in the two beam image.

In the current work, strain contrast is analyzed in a cross-sectional image, allowing an understanding of uniaxial strain (in the growth direction) in multiple layers of stacked SiGe islands. The interpretation of images depends not only on the TEM technique used, but also on sample preparation, which is represented in the cartoon of

Figure 3.5. Estimation of strain using cross-sectional images is significantly more complex than with top-view images, as those in Ref. [56]. Top view images of samples with a single island layer allow the estimation of an absolute value for strain since it is done relative to an unstrained substrate. In cross-sectional images of the nanostructure, electrons do not enter unstrained regions of the sample. At the front face of the ~ 50 nm thick cross-sectional samples prepared, the centers of SiGe clusters are approximately aligned with the surface; the back face is weakly aligned with valley regions between clusters. Most electrons of the incident beam therefore, pass through Si layers that are not entirely unstrained (recall Ge interdiffusion from Sub-section 3.1.1.1), before reaching clusters, and any estimation would be relative to strain in these corresponding Si layers.

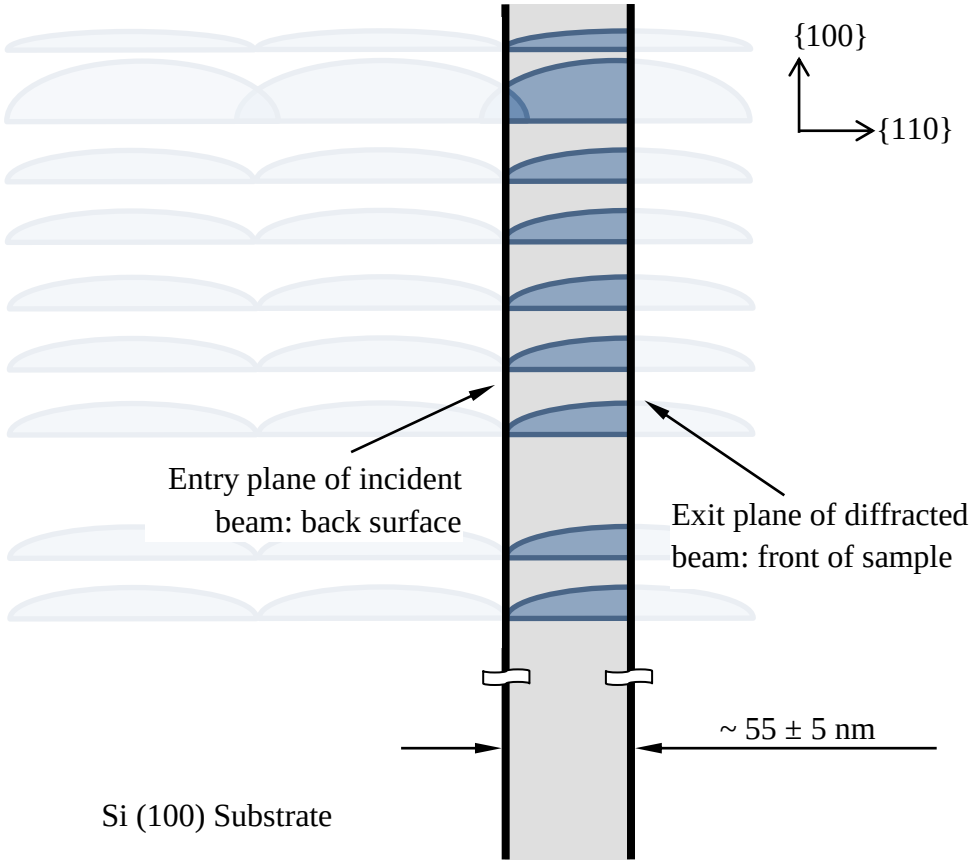

Figure 3.5 Cartoon of the thickness-modified Si/SiGe nanostructure after preparation for TEM analysis showing side-view of samples. Front and Back faces of the prepared cross-section are perpendicular to the plane of diagram. Regions of the sample removed during preparation are blurred. In the region analyzed, the front surface of the sample approximately aligns with the centers of SiGe domes, and the back surface contains valleys of the morphology. Contrast in TEM images depends on the morphological features encountered by electrons as they traverse between the entry and exit planes of the cross section.

Analytical TEM or Energy Dispersive X-ray spectroscopy was used to obtain Ge content as a function of depth in the nanostructures. In this technique, the electron beam of the TEM is converged onto a location on the sample. The high energy electrons interact with and eject electrons in inner shells of atoms, leading to a transition of an electron from an outer shell to the shell of the former electron. The transition is

accompanied by the emission of X-rays of energy specific to the atom. The intensity of these X-rays, being directly proportional to the number of these atoms in the focused area of the incident electron beam, yields quantitative information on the composition of samples, and when acquired over distance, provides a compositional profile of the sample. Results from this technique have been reported for nanostructures with a wide range of Ge content [51]; results from sample B are presented in Chapter 4.

3.1.2 Silicon-On-Insulator Thin Films

Photoluminescence in the Silicon-On-Insulator (SOI) system was studied using a standard, commercially available SOI wafer, produced by bonding. The SOI wafer comprised an unpassivated 2 μm thick Si (100) film of resistivity ~ 10 Ωcm, a 1 μm thick oxide insulator, on a ~ 500 μm thick Si substrate.

3.2 Photoluminescence Experiments

The setup for PL experiments used in this study is schematically represented in Figure 3.6. Electron-hole pairs are created in experimental samples by exciting them with photons of specific wavelengths; subsequent radiative recombination (i.e., PL) is detected, filtered from noise, amplified, converted to digital data, and recorded. The properties of the materials used in this work necessitate that PL experiments be performed at low temperatures. A closed-cycle liquid He cryostat equipped with a high thermal-conductivity cold finger, a high reflectivity thermal shield, and a sapphire sample base with a Cu clamp attached at the tip of the cold finger provided the low temperatures needed. These were enclosed in a chamber with sapphire windows that allowed exciting light to access the sample; the chamber was evacuated to $< 10^{-5}$ mbar pressure before being cooled. Sample temperature was controlled using a PID control system (Lakeshore Temperature Controller), which thermo-electrically heated the cold finger. The entire set up including the sample chamber and the various optical elements were placed on an optical bench which provided isolation from the environment.

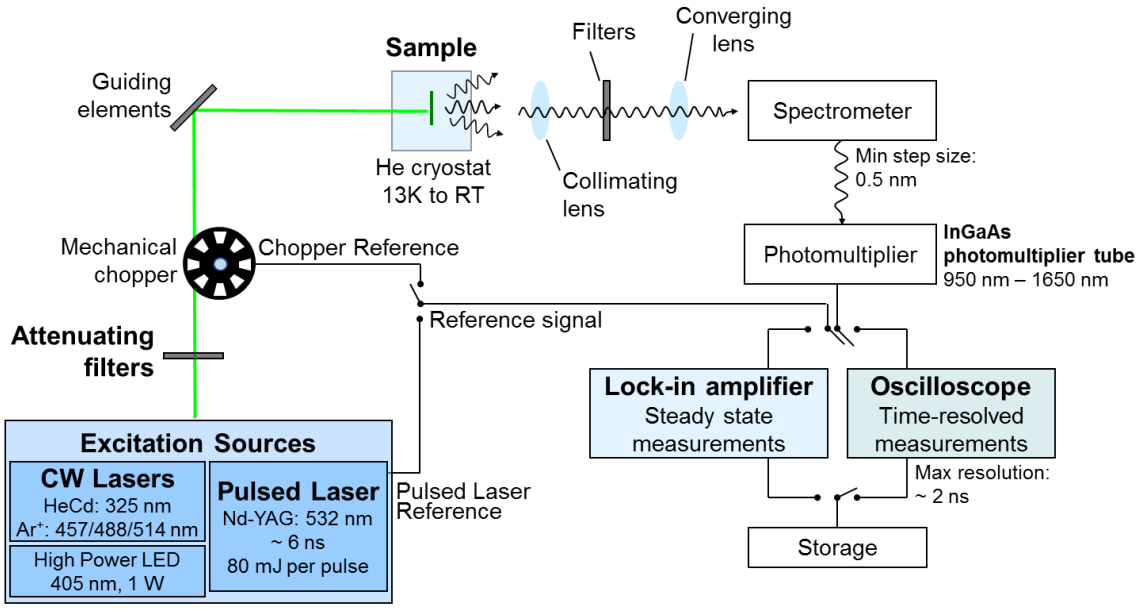

Figure 3.6 Combined schematic representation of experimental setup for PL spectroscopy and time-resolved measurements. The optical path showing sample excitation by various light sources, collection of emitted light, separation into spectral components, amplification, and storage, is indicated with relevant detail.

Several monochromatic light sources were used; their details and relevant properties are presented in Table 3.2. Light from these sources was guided by optical elements such as mirrors and prisms, and directed at a sample through the sapphire window of the cryostat chamber. Photoluminescence exiting the back surface of samples and the cryostat window was collimated and converged on the entrance slit of a 0.5 m monochromator (Acton Research, SpectraPro 500i), equipped with a diffraction prism with gratings of different ruling densities. A fast, air-cooled, near-infrared InGaAs photocathode, sensitive in the range 0.76 – 1.3 eV, with a high voltage photomultiplier tube (Hamamatsu Model H9170-75) is placed at the exit slit of the monochromator. Care is taken to decrease the width of monochromator slits to the extent possible. Electrical

signal from the photomultiplier tube is sent via low capacitance cables to the either an amplifier or an oscilloscope.

Three types of light sources have been used in this work: Continuous wave (CW) lasers, a Light Emitting Diode (LED), and a Pulsed laser. CW photoexcitation was provided by either a 40 mW, HeCd gas laser emitting at 325 nm (Kimmon IK3501R-G), or a multiline 100 mW, Ar^+ gas laser, emitting at 457 nm, 488 nm, and 514.5 nm (LaserPhysics, Reliant 150m). Specific emission wavelengths of the Ar^+ laser could be selected using in-built optical filters. CW laser beams were focused on the sample using wavelength-specific convergent lenses, with a visually estimated spot diameter of about 1 mm. Continuous excitation converged from a high power LED emitting at 405 nm (Thor Labs, M405L1), with up to 1 W optical power output, formed an approximately square spot on the sample with side ~ 6 mm.

Pulsed photoexcitation of samples was provided by a solid-state, Nd-YAG pulsed laser (Quantel, BRIO IR-GR), emitting 100 mJ worth of photons of wavelength 532 nm in ~ 6 ns pulses, with an approximate spot diameter visually estimated to be about 3 – 4 mm. Used directly, the energy of each pulse would be much greater than the density of excitation required; the light was therefore, usually attenuated by a few orders of magnitude using neutral density filters and was directed to the sample unfocussed. The laser was set to output at ~ 20 Hz.

The approximate concentration of electron-hole pairs produced by the various excitations is useful to know since recombination processes strongly depend on this quantity. This is obtained by estimating the number of photons absorbed in the sample,

and the volume of the sample that is covered by the specific excitation used. This volume is obtained by integrating the exponential dropping absorption in the sample over the thickness of the material, as shown in the following expression.

$$\text{Excitation volume} = \int_0^\infty A \exp\left(-\frac{x}{d_p}\right) dx = A \cdot d_p \tag{3.2}$$

This expression assumes an infinite sample thickness for simplicity, well justified for an estimation of absorption decaying exponentially, with a characteristic distance d_p, called the penetration depth. The volume also depends on the area covered by the excitation (A), equal to that of the excitation spot used in the experiment, approximately circular in most cases. Assuming that every photon that is absorbed in the sample creates an electron-hole pair, the average non-equilibrium photogenerated carrier concentration can be estimated using the following expression, where the numerator estimates the number of photons absorbed for a given excitation.

$$\text{Photogenerated Concentration} = \frac{\eta_{abs} \times f \times \frac{\lambda}{\hbar c}}{A d_p} \tag{3.3}$$

In the above expression, η_{abs}, the absorption efficiency is a strong function of the experimental setup, and is estimated as 10%. Since the period of excitation is different among the photoexcitation sources used, the relevant fraction of time over which the

sample is excited is accounted for by the quantity *f*, which depends on the type of excitation. For example, in continuous excitation experiments, Expression 3.3 yields the total generated concentration over 1 second. Since these experiments use a square wave modulation of the excitation, this fraction is developed starting with a factor of 0.5. It must be understood that recombination mechanisms are much faster than 1 s, and for practical purposes, this represents a steady-state for continuous excitation experiments. In pulsed laser experiments, this fraction is 1, and is understood that the concentration given by the expression is created practically instantaneously in experiments that use ~ 6 ns pulses for excitation. For comparison, the concentration generated in 6 ns for a similar continuous excitation, would be 8 orders of magnitude less, but sustained over 0.5 seconds. For various excitation wavelengths used, and their corresponding penetration depths in Si, Expression 3.3 gives the approximate range of electron-hole pair concentration that is generated in an experiment, as shown in Table 3.2. It must be noted that the concentrations shown in the table are valid over different time scales as mentioned above.

Table 3.2 Parameters of Excitations used in PL Experiments

Excitation Wavelength / Type (Source)	**Penetration Depth** [nm] (**Absorption Coefficient** $\times 10^5$ [cm^{-1}])		**Number of photons emitted in 10 mW (continuous) or 10 mJ (6ns pulsed) excitation**	**Corresponding carrier concentration in 1 penetration depth of Si (excitation area used)** [cm^{-3}]
	Si	**Ge**		
325 nm / CW (HeCd)	8.1 (12.35)	8.47 (11.8)	1.635×10^{16}	3.56×10^{21} ($0.28\ cm^2$)
405 nm / High power LED	123 (0.813)	13.74 (7.28)	2.037×10^{16}	2.3×10^{20} ($0.36\ cm^2$)
457 nm / CW (Ar^+)	445 (0.225)	15.48 (6.461)	2.299×10^{16}	8×10^{20} ($0.03\ cm^2$)
488 nm / CW (Ar^+)	762 (0.131)	15.74 (6.352)	2.455×10^{16}	5.1×10^{20} ($0.03\ cm^2$)
514.5 nm / CW (Ar^+)	1075 (0.093)	15.86 (6.3)	2.588×10^{16}	3.83×10^{20} ($0.03\ cm^2$)
532 nm / Pulsed (Nd-YAG)	1280 (0.078)	16.93 (5.91)	2.676×10^{16}	1.06×10^{20} ($0.196\ cm^2$)

Sources: Absorption data were obtained from Ref. [59] for Si and from Ref. [60] for Ge.

3.2.1 Photoluminescence Spectroscopy

For CW excitation, the signal-to-noise ratio of the detected PL was enhanced by amplifying it with respect to a reference signal obtained from a mechanical chopper, which also modulated light emitted from the source before sample excitation. This standard noise cancellation was provided by a lock-in amplifier (Princeton Applied

Research, EG&G 128A). The electrical output of the amplifier was digitized by an analog-to-digital converter (Acton Research, NCL). Software (Acton Research, SpectraSense 4.0) that controlled the selection and turning of the monochromator gratings, also sequentially accumulated the digital raw count off the NCL spectral measurement system. This raw count, acquired over a predetermined period of time, then represented PL intensity shown in the spectra of Chapters 4 and 5. For pulsed excitation, electronic output available directly from the laser source was converted to a square wave signal using a pulse generator (HP, 8012B), and then used as the reference signal required for lock-in amplification.

3.2.1.1 Excitation-intensity Dependent Technique. The study of the dependence of PL spectral features on the number of generated electron-hole pairs is enabled by acquiring the PL spectra under various CW excitation intensities, or various energy densities of pulsed excitation. At an appropriately lowered sample temperature, photoexcitation places the electron-hole system in a specific region of its phase diagram (Figure 2.7) initially, which then relaxes via recombination reflected in the PL spectra. By changing the initial position of electron-hole pairs in the phase diagram and analyzing corresponding changes to PL spectral features, inferences on the mechanism of recombination, including non-radiative recombination, can be drawn. The control of this initial position is achieved by changing excitation levels.

For visible excitation, intensity or energy was measured immediately before exciting the sample, and varied using neutral density filters. For UV CW excitation, intensity was changed by reducing beam size using an iris. Amplification of output from

the PMT was optimized for maximum resolution of the electrical signal. Various experimental parameters were carefully recorded and raw counts were scaled to accommodate any changes made to optimize experimental conditions.

3.2.1.2 Excitation-wavelength Dependent Technique. When short wavelength photons are used to excite materials, they are absorbed within smaller distances than longer wavelength photons (this assumes wavelengths much larger than atomic dimensions of the material). This fact is used to selectively excite the nanostructures being studied. The penetration depth of a photon is the distance in the excited material, in this case Si/SiGe 3D crystalline nanostructures, by which the number of photons absorbed drops by a factor of 1/e, and is used here as a standard for comparing various excitations. The value of this parameter depends on the band structure of the semiconductor, and is equal to the reciprocal of its absorption coefficient. The penetration depth versus excitation wavelength plot, developed using absorption data for bulk Si and bulk SiGe alloys published in the literature [59, 60], is shown in Figure 3.7.

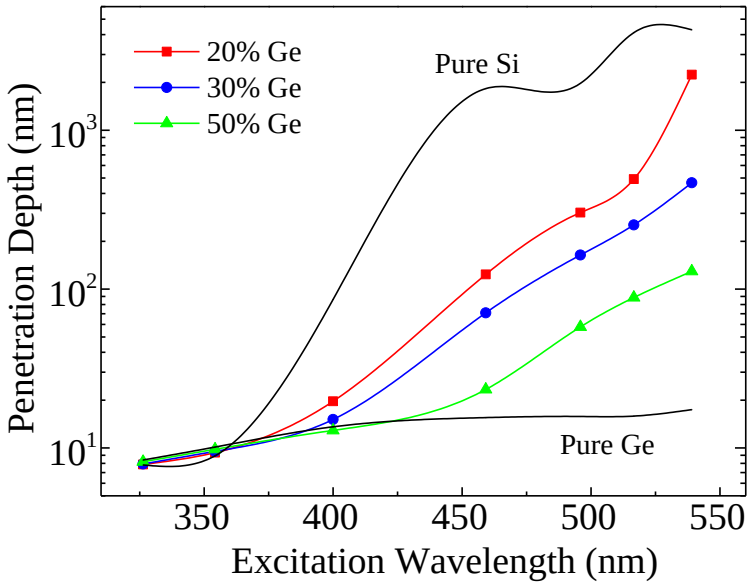

Figure 3.7 Penetration depth of excitation photons in bulk SiGe alloys as a function of their wavelength for various Ge compositions (indicated). Points are marked for wavelengths used in this work. The penetration depth in pure Si and pure Ge is also shown for comparison.

Using values for penetration depth from Figure 3.7, the absorption through the multilayers in the Si/SiGe nanostructures is estimated. Although SiGe island layers are undulating, a uniformly flat morphology is assumed, with thickness equal to the height of islands at their center. The error this introduces is partially offset by using an effective Ge content of SiGe layers as approximately half of their known value. The estimation also assumes zero reflection at Si/SiGe interfaces. These assumptions lead to only a rough approximation of absorption in the nanostructure, but they considerably simplify the estimation by circumventing a two-dimensional numerical solution that would otherwise be required. For a typical superlattice with uniformly thick $Si/Si_{0.8}Ge_{0.2}$ layer-layer pairs (note reduced Ge content), normalized absorption through the multilayers estimated by accounting for the different absorption coefficients in Si and SiGe is shown in Figure 3.8.

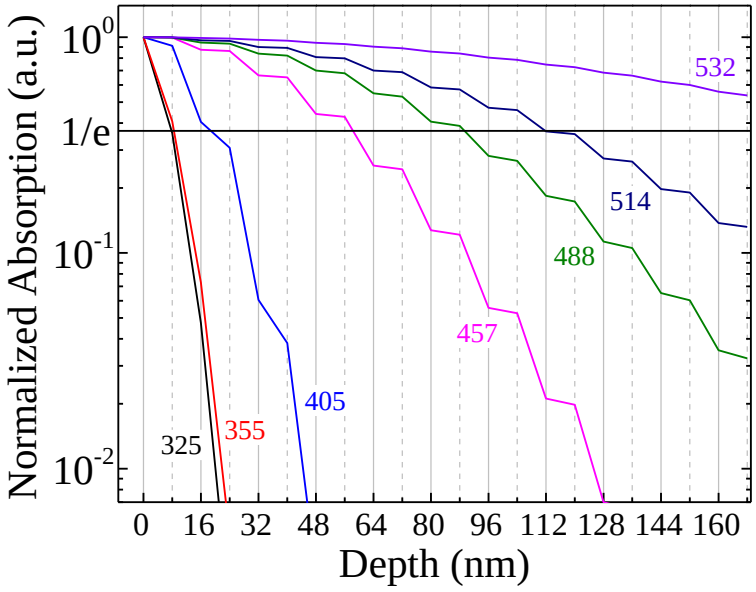

Figure 3.8 Normalized absorption through a $Si/Si_{0.8}Ge_{0.2}$ superlattice with uniformly thick layers, for various excitation wavelengths (indicated). The 1/e (~ 37 %) depth for a given excitation wavelength allows an evaluation of the region of the nanostructure covered by the photoexcitation. Solid and dashed gridlines indicate the top surfaces of Si and SiGe layers respectively; note log scale.

Following the same procedure for a strain-engineered nanostructure (sample C), the absorption through non-uniformly thick layer-layer pairs, using thicknesses seen in TEM images, is plotted in Figure 3.9. Absorption estimates from these figures are used to interpret PL data in Chapter 4.

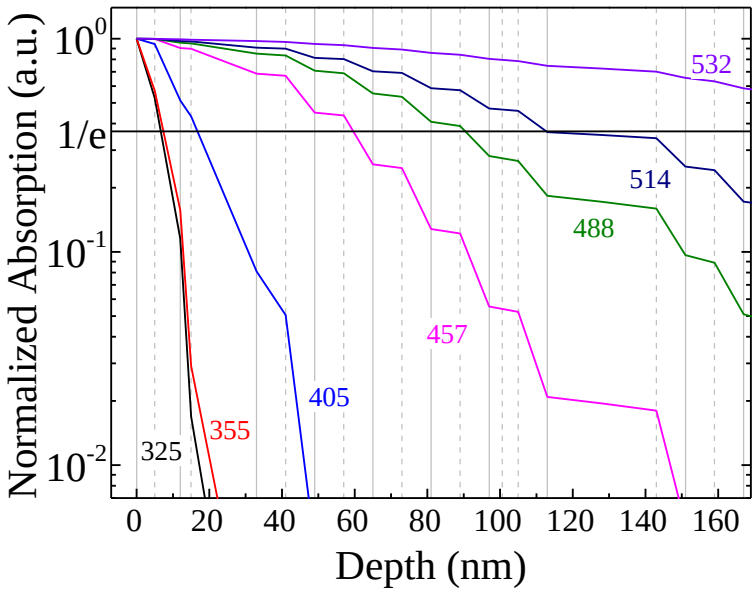

Figure 3.9 Normalized absorption through a $Si/Si_{0.8}Ge_{0.2}$ superlattice with non-uniformly thick layers, for various excitation wavelengths (indicated). The 1/e (~ 37 %) depth for a given excitation wavelength allows an evaluation of the region of the nanostructure covered by the photoexcitation. Solid and dashed gridlines indicate the top surfaces of Si and SiGe layers respectively; note log scale.

3.2.2 Photoluminescence Kinetics

Time-resolved experiments provide critical information about the dynamic behavior of electron-hole pairs, including their lifetime in the excited material. The shortest time interval during which a change in PL intensity can be accurately recorded, i.e., the time resolution, is determined by the slowest changing component of the experimental path, from excitation to data acquisition. This is particularly important for time-resolved measurements of PL intensity because optical processes in the materials studied often occur at very short time scales, sometimes even faster than the limit of the experiment. An incomplete understanding of the response time of individual components could lead

to erroneous data interpretation. Kinetics at the short time scales seen in this work ($< 10^{-2}$ s) were experimentally studied using pulsed laser excitation; phenomena that occurred over relatively long time scales ($\sim 10^{3}$ s) was studied using continuous photoexcitation.

3.2.2.1 Kinetics under Pulsed Excitation. PL kinetics were studied using 532 nm pulsed laser excitation (see Table 3.2) and acquired using a 200 MHz digital oscilloscope (Lecroy 9310M). The oscilloscope received its input from the PMT module and was triggered directly by electrical output of the laser modulating controller, thus internally synchronizing detected signal with reference to the photoexcitation. For very quickly varying PMT signals, the decay time of input channels was reduced to ~ 2 ns using small termination resistors in parallel with the large internal DC coupling of the oscilloscope. This determined the time resolution of the experiments. The transients were averaged over 1000 triggered acquisitions.

3.2.2.2 Slow Dynamics under Continuous Excitation. Slowly varying PL kinetics were acquired using the same experimental setup as for PL spectra acquisitions, with the exception of the recording procedure. Raw counts from the data acquisition system were digitally recorded using software (SpectraSense and ScreenReader). Since the photoexcitation ON time was a critical experimental parameter, every new acquisition was done after warming the sample to room temperature, re-cooling to the temperature required for the experiment, and then performing the experiment on a freshly cooled sample.

CHAPTER 4

RECOMBINATION IN Si/SiGe THREE-DIMENSIONAL NANOSTRUCTURES

Various possible manifestations of Auger processes in the group IV systems being studied have come to light. This chapter describes results from photoluminescence experiments and discusses recombination, including the role of Auger processes, in the Si/SiGe nanostructure system. It is important to note that the presence of an Auger process is inherently difficult to detect because the only quantity directly measured in PL experiments is the number of electron-hole pairs that recombine radiatively. Any inference about Auger processes is then made by interpreting the cause for an observed change in radiative recombination and any conclusion about the role of an Auger process is reached indirectly.

Three different samples, described in Chapter 3 (Table 3.1), were used to investigate recombination processes in the three-dimensional Si/SiGe nanostructure system. Experimental results are presented and discussed in the following three sections, that lead to several significant conclusions including band bending at Si/SiGe interfaces in low Ge content nanostructures, the determination of the upper limit for the exciton diffusion length in the nanostructures, and a delayed Auger onset under prolonged and continuous photoexcitation.

4.1 Auger Fountain and Hole Redistribution

In Si/SiGe nanostructures with high Ge content in SiGe clusters (~ 55%), several effects have been reported including an Auger fountain and a delayed hole transfer [4, 6]. The depth of the potential well formed by the SiGe clusters determines several properties of their luminescence, including the important PL peak position. The influence of SiGe well depth on recombination mechanisms is explored here via PL experiments on a nanostructure grown with lower Ge content (~ 16%) in the clusters (sample A), but is otherwise identical to the one described in Refs. [6, 39]. In these references, Auger recombination at interfaces of high Ge content clusters and Si films were seen to facilitate the formation of an electron-hole condensate in the Si films. Upon subsequent decay of the liquid drops, holes were seen to re-localize in SiGe wells, via PL kinetics experiments. Auger recombination at interfaces of low Ge content clusters and Si films, with correspondingly shallower potential well depths, is expected to show an enhanced Auger Fountain mechanism, since ejected Auger holes have smaller barriers to overcome than those in high Ge content nanostructures; this hypothesis is tested in this study. A dark-field TEM image of the sample is shown in Figure 3.1. Where relevant, properties of the high Ge sample needed for comparison with current results are mentioned and have been obtained from Refs. [6, 39].

4.1.1 Results of Photoluminescence Experiments

Figure 4.1 shows PL spectra acquired at 20 K, using multiple lines of an Ar^+ laser, at various excitation intensities that covered 2 orders of magnitude. At this level of photoexcitation, a broad PL feature centered at 0.95 eV associated with SiGe clusters

[61], and narrower features typical of phonon-assisted free exciton (FE) recombination in Si are seen. As excitation intensity is increased, all PL features are seen to increase in intensity, but not all increase proportionately with excitation intensity, clearly seen in the log scale plot. The FE PL features due to free excitons appear at 1.137 eV, 1.096 eV, and 1.033 eV, which are known to be due to TA, TO, and TO + O^{Γ} phonon-assisted recombination, respectively [8].

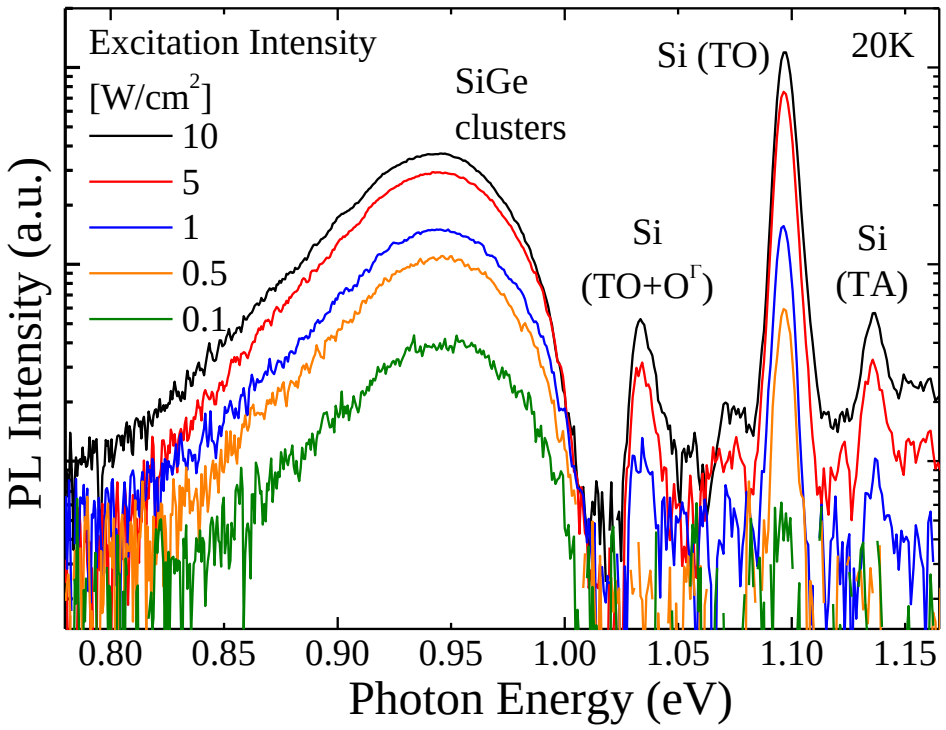

Figure 4.1 Low temperature PL spectra of Si/SiGe nanostructure with low Ge content (~16%), acquired using CW excitation from multiple lines of the Ar^+ laser. Excitation intensities (indicated) covering two orders of magnitude generated electron-hole pairs densities well under the Auger concentration threshold for bulk Si. PL features are identified and discussed in the text; note the log scale.

Figure 4.2 shows the PL intensity of the TO-phonon-assisted FE PL peak, and that due to recombination associated with SiGe clusters, as a function of excitation intensity. The double-log plot clearly shows that the FE PL peak increases linearly with excitation intensity, whereas that due to clusters shows a strongly sublinear increase, at this level of excitation. In Si/SiGe nanostructures with higher Ge content (~ 55%) in the clusters, a sublinear was not seen at the same excitation levels [39].

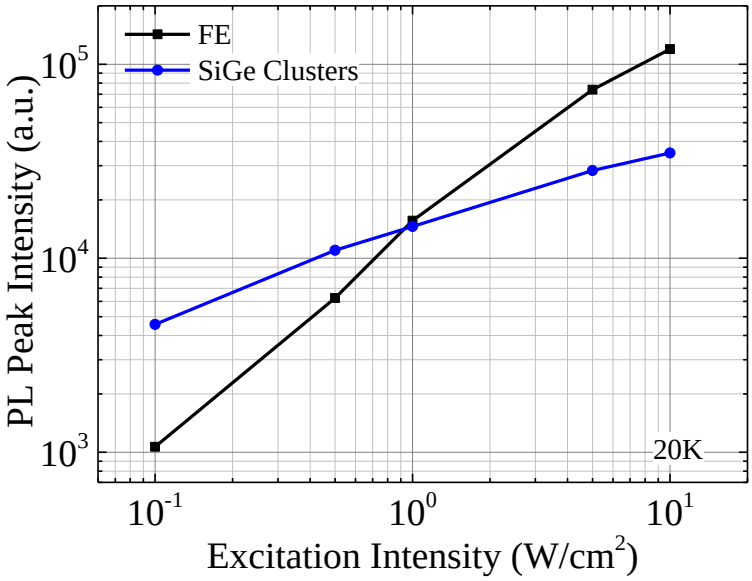

Figure 4.2 The behavior of PL peak intensity due to FE recombination and that associated with low Ge content SiGe clusters, as a function of excitation intensity. Low levels of excitation covering ~ 2 orders of magnitude of intensity were used. Note the double log scale; lines are visual aids.

Figure 4.3 shows the PL spectra acquired under higher levels of photoexcitation, using a 6 ns pulsed laser, again covering two orders of magnitude. The area covered by the laser spot during experiments is estimated visually; errors in this estimation may downscale the energy densities mentioned by about 3 times, but not by an order of magnitude or more. At the lowest excitation energy density used (0.01 mJ/cm^2, part a),

the broad PL feature about 0.95 eV, prominent in the PL spectra under CW excitation (Figure 4.1), is not visible. The TO-phonon-assisted FE PL peak at 1.096 eV is present, along with a broader PL peak at 1.081 eV, which is attributed to recombination of electron-hole pairs in the electron-hole-liquid (EHL) formed at this level of photoexcitation. The PL peak due to recombination in the EHL is seen to grow very quickly in comparison with the FE PL peak, as shown in part (b), and eventually becomes the most dominant PL feature.

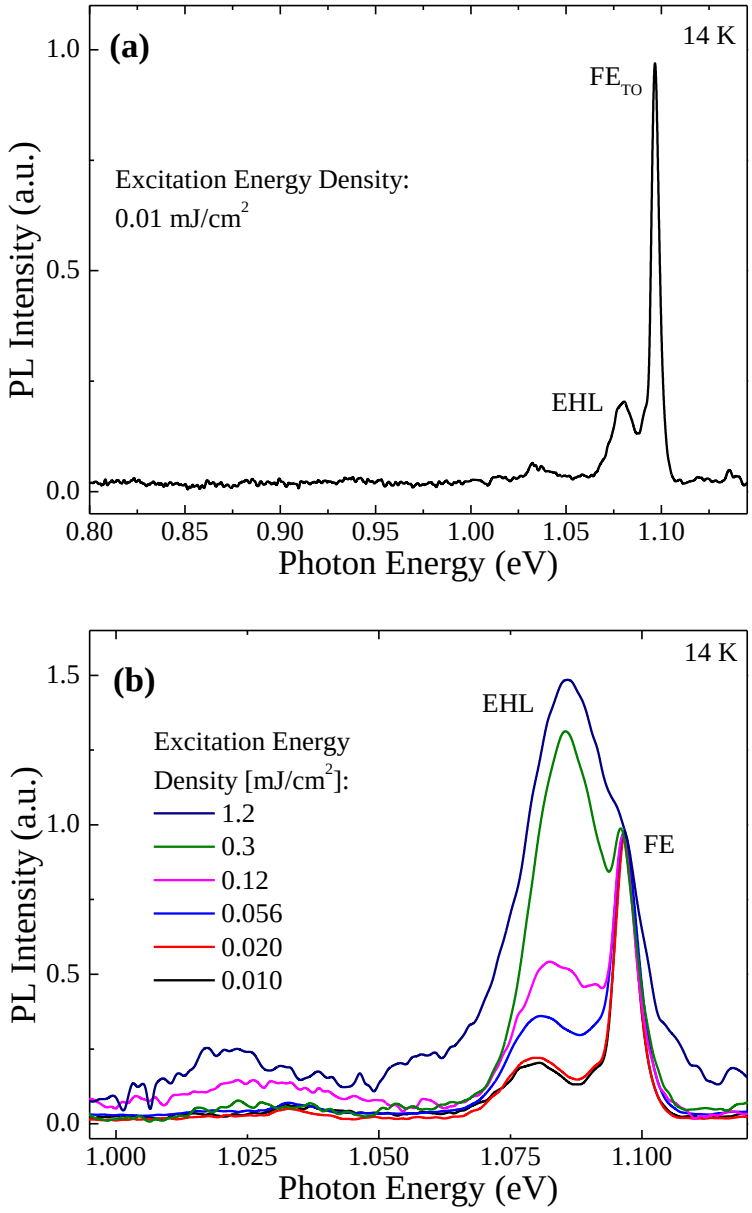

Figure 4.3 Low temperature PL spectra of with low Ge content Si/SiGe nanostructures, under pulsed laser excitation at various energy densities. The PL feature associated with SiGe clusters about 0.95 eV seen under CW excitation is not visible under pulsed excitation, as seen in (a). The behavior of the EHL PL peak as excitation level is increased is highlighted in (b), in which spectra have been normalized to the FE PL peak intensity for comparison. Excitation energy densities are varied over 2 orders of magnitude.

Figure 4.4 shows the behavior of the PL peaks due to FE and EHL recombination, as a function of excitation energy density, on a double log scale. It can be seen that at these relatively high levels of photoexcitation, the FE PL peak intensity continues to increase linearly as it does under CW excitation, unless very high excitation levels are used. This is accompanied by an almost linear (slightly superlinear) increase in the EHL PL peak intensity, as expected when pumping deeper into the liquid region of the phase diagram (Figure 2.7). At the highest excitation energy densities used, both PL peaks saturate and increase sub-linearly.

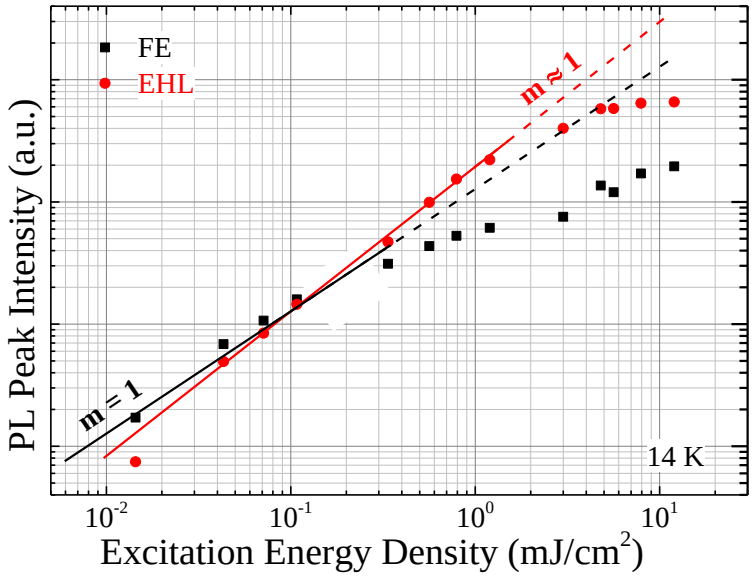

Figure 4.4 The behavior of PL peak intensity due to FE and EHL recombination in low Ge content Si/SiGe nanostructures, as a function of excitation energy density. High levels of excitation, covering ~ 3 orders of magnitude of energy density, were used. Note the double log scale; lines with indicated slopes are visual aids.

Under the pulsed laser excitation used, carrier densities over 3 orders of magnitude larger than those produced under the CW excitation are created. Clearly at

these excitation levels, an Auger process seen at lower excitation levels is expected to continue to show saturation of the PL. The intensity of PL peaks recorded in lab experiments however, is also about 3 orders of magnitude larger than background noise levels, and for a PL feature seen under CW excitation to be detectible under pulsed laser excitation, simultaneously with the FE and EHL features, a significant increase in PL intensity would be needed. The absence of the 0.95 eV PL feature at higher excitation, shown in the linear scale of Figure 4.3(a), further indicates the increase in PL intensity due to interface recombination is under three orders of magnitude as expected for a sub-linear increase, cannot therefore be distinguished for this level of photoexcitation or plotted in Figure 4.4.

Figure 4.5 shows low temperature kinetics of the PL spectral features due to recombination associated with FEs (recorded at 1.096 eV), EHL (1.081 eV), and SiGe clusters (0.95 eV), over two orders of magnitude of excitation energy densities. The PL decay curves have been normalized at $t = 0$. Noise levels are at least two orders of magnitude below initial PL levels.

Under all excitation energy densities shown, it is seen that the PL due to carriers localized at Si/SiGe heterointerfaces (blue curves) show a multi-rate decay, with an initial fast component, and then a much slower decay component (lifetime ~ 10^{-5} s). With increasing excitation, the fast component is seen to accelerate, and the slow component sets in at progressively lower PL levels (clear under log scale). This PL behavior is typical of Auger recombination. Deviations from an exponential behavior of the initial PL decay are also observed before the slow decay rate sets in, especially under the highest excitation energy density shown.

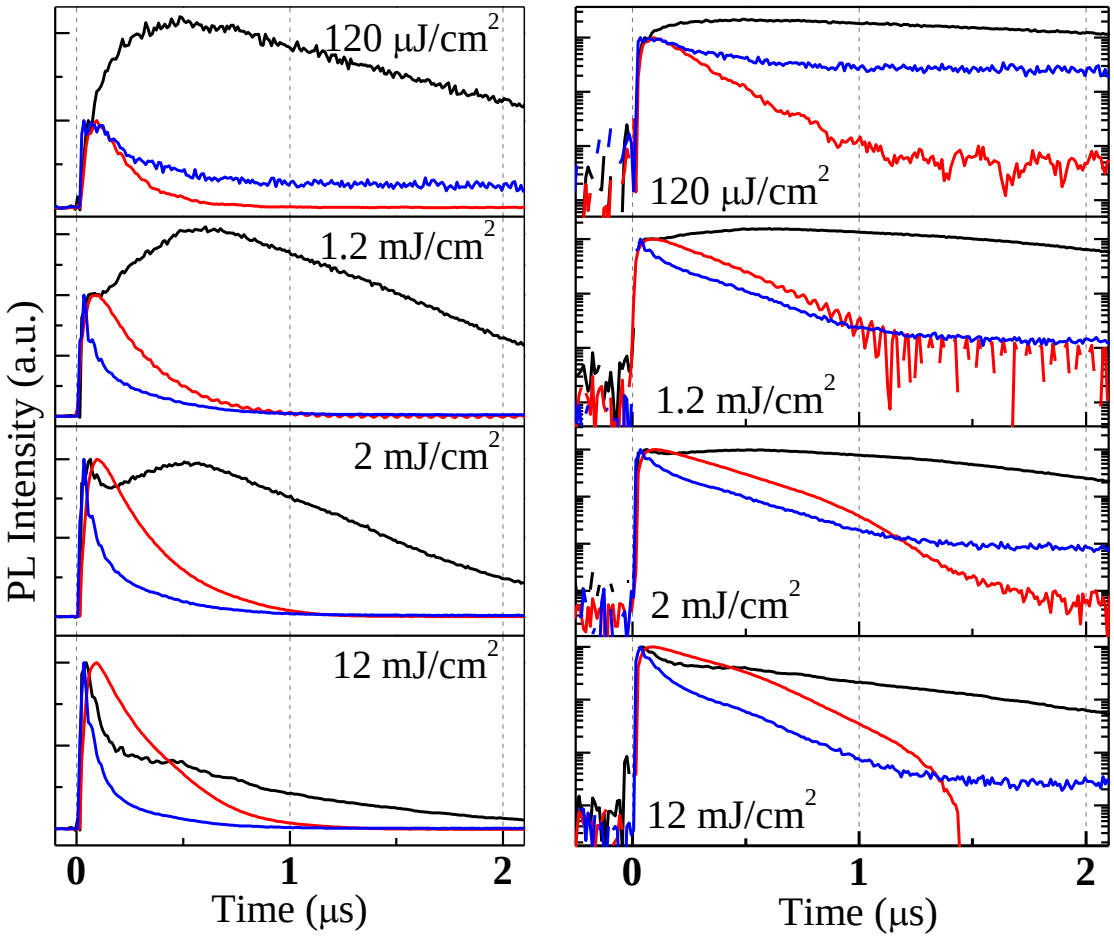

Figure 4.5 PL kinetics of relevant PL spectral features of low Ge content Si/SiGe nanostructures acquired using various excitation energy densities, shown on both linear (left) and log (right) scales for clarity. These PL features are due to recombination associated with FEs (black), EHL (red) and the SiGe clusters (blue). Transients have been normalized at $t = 0$; sample temperature was 16 K.

Several reports of exponential decays of EHL drops in Si mention ~ 100 ns lifetimes [6, 7, 25, 62]; in all reports, EHL PL is not observed beyond 1 μs after the end of the excitation pulse. In the current work, PL due to radiative recombination in the EHL (red curves) under the lower excitation energy densities used (0.12 and 1.2 mJ/cm^2), shows a near-exponential behavior (lifetime ~ 10^{-7} s) and reduces to near-noise levels by ~ 1 μs. This decay is prolonged under 2 and 12 mJ/cm^2 excitation, and lasts beyond 1 μs.

Also, long rise times of ~ 80 ns, are measured under all excitation energy densities shown, compared to bulk Si samples where rise time is shorter than the ~ 3 ns time resolution of the experiment. The traditional acceleration of the decay when approaching a sharp and distinct cutoff (see Section 2.4) is seen only for the highest excitation used.

The surprise in the PL dynamics data of Figure 4.5 lies in the kinetics of FEs (black curves), which show longer rise times at the lower excitation densities shown (clear on linear scale), in comparison with their typical ns rise time seen in bulk Si (reported for example, in Ref. [6]). This slow rise disappears under 2 and 12 mJ/cm^2 excitation, where a quick initial decay is seen. Under 2 mJ/cm^2 excitation, the fast initial decay is followed by a delayed increase in PL intensity, which is not seen under 12 mJ/cm^2. Under all excitation densities used, the FE PL eventually assumes the typical exponential decay with lifetime ~ 2 μs.

4.1.2 Discussion

Experimental data are explained in this section by the interplay, both in space and in phase, between electron-hole pairs that form free excitons, condense into liquid, or form spatially indirect excitons localized at the SiGe cluster - Si layer interface. The model assumes a type II energy band alignment at the Si/SiGe heterointerface, proposed by several groups [63-66], and the absence of defects in the nanostructure, particularly at interfaces. Since interface defects are classic sources for non-radiative recombination, the presence of sustained PL in these data is proof of the high epitaxial quality of the grown structure.

At low levels of excitation (Figures 4.1 and 4.2), it is seen that carriers localizing and recombining radiatively at the interface to produce the broad PL band with intensity (I_{PL}) peaked at 0.95 eV, do not do so in proportion with excitation intensity (I_{exc}). This sublinear behavior, $I_{PL} \propto {I_{exc}}^{n}$ where n ~ 0.5, typically occurs due to a three-particle Auger process. At higher levels of excitation (Figure 4.5), an accelerated initial component of their PL decay and the progressive reduction of PL levels of the slow component, strongly indicate that Auger recombination dominates until the concentration of indirect excitons falls below the Auger threshold.

The sublinear increase of the interface PL at low excitation levels, unlike that in samples with higher Ge content (deeper potential wells for holes) [39], indicates that the concentration threshold for Auger recombination of indirect excitons localized along shallow potential wells is lower than that along deeper potential wells. Holes ejected by Auger recombination at a type II interface with a larger effective energy bandgap, ~ 0.95 eV with 16% Ge in clusters (compared to ~ 0.8 eV with 55% Ge) and correspondingly large energy compared to those ejected from lower bandgap interfaces, are also faced with smaller 100 – 300 meV energy barriers (versus 250 – 450 meV wells in 55% Ge clusters [6, 39]). Thus, "Auger holes" in relatively shallow potential wells can be expected to have a higher probability of leaving the well. At this level of excitation, carrier concentration outside the well is not sufficient to produce a condensate of electrons and holes. Thus, Auger holes cannot contribute to PL due to the EHL in Si layers and the Auger Fountain (Section 2.1) is not observed at this excitation level.

Assuming that saturation of the interface PL under low level excitation (the sublinear increase of Figure 4.2) continues at high excitation levels, the simultaneously

short fast decay component of their PL kinetics, along with the correlated ~ 80 ns long rise time of the EHL PL, indicate that the Auger Fountain exists. Note that the rise time of the EHL PL is on the order of the Auger ejection of holes from SiGe wells. Recall that the EHL is approximately electrically neutral [12]. Thus, in addition to electron-hole pairs in Si contributing to the neutral EHL, excess electrons are expected to provide overall charge neutrality in Si, given the occupation of SiGe wells by holes across the type II interface. Energized Auger holes entering the Si region, can contribute to the condensate along with readily available electrons in Si. Inferring from the correlation of the PL intensities of the two features, it is seen that Auger-mediated hole transfer over Si barriers contributes to carrier condensation in Si, increasing the concentration of electron-hole pairs in the liquid phase and their luminescence intensity. This Auger Fountain mechanism has also been observed in Si/SiGe nanostructures with ~ 55% Ge in the clusters [6], but presumably starts to appear at a lower excitation in the current nanostructure because of a lower Auger threshold. The Auger hole transfer in this low Ge content nanostructure does *not* appear to be more efficient than that in high Ge content nanostructures, as hypothesized earlier.

Over a large range of excitation intensities, the FE luminescence increases linearly (Figure 4.2 and lower energy densities in Figure 4.4), indicating no dependence on processes that may increase the photogenerated FE concentration. At higher excitation levels however, long rise times in their kinetics (Figure 4.5, 0.12 and 1.2 mJ/cm^2) indicate a small, additional supply of FEs that continues after their quick generation (PL rise time in bulk Si ≈ 20 ns). Auger processes have a lifetime of ~ 10^{-8} s and any increase in PL intensity caused by an Auger Fountain mechanism is expected to occur very

quickly after the excitation pulse. With rise times of ~ 0.5 μs and the absence of a superlinear behavior of PL intensity with increasing excitation, Auger recombination cannot be expected to produce the observed kinetics of the FE PL at 0.12 and 1.2 mJ/cm^2 excitation. This is also inferred from Si recombination kinetics in the absence of SiGe energy wells (Chapter 5 of this dissertation), where a supply of holes from an Auger Fountain is not possible.

Several properties of the EHL have been experimentally observed to be quite different in spatially confined Si films than in bulk Si; examples include radiative lifetime [62] (and therefore drop radius), and the concentration threshold for condensation [67]. The increase in surface-area-to-volume ratio brought about by spatial confinement has a direct effect on properties of the EHL that depend on these quantities. For example, in bulk material, the EHL recombination rate is directly proportional to drop volume, and the rate of exciton evaporation and backflow are directly proportional to the EHL surface area, clearly seen in the differential equations of early models for EHL dynamics [12, 25, 30, 31]. The literature however, lacks serious investigations of the change in these properties, evaporation in particular, as the area-to-volume ratio of the EHL is increased. This occurs when a spatial dimension of the host crystal decreases below the dimension of the EHL.

Under 0.12 and 1.2 mJ/cm^2 energy densities, the PL spectra (Figure 4.3) indicate that the system is excited well into the liquid region of the phase diagram; i.e., most carriers contribute to the condensate in Si practically instantly. The EHL drops decay mainly via recombination (both radiative and Auger) and evaporation [12, 25]. During evaporation, the release of FEs is energetically more favorable than that of free carriers

[12]. Besides being a strong function of temperature, this is also a surface phenomenon and is expected to be enhanced under strong spatial confinement. The temperature dependence of the evaporation rate is given by $T^2 \exp(-\varphi/k_B T)$, where φ is an activation energy for exciton evaporation (equal to their condensation energy [25]). At the experiment temperature, this is about ~ 10^3 times more than that seen in Si films at the liquid He temperature (see Ref. [62]), where long FE rise times are not seen. Thus, with a larger area-to-volume ratio than in the bulk, and a relatively high condensate temperature, evaporation of FEs from EHL drops can be significant and seems to be the most likely cause for the increase in FE concentration observed in the PL dynamics under 0.12 and 1.2 mJ/cm^2 energy densities.

When a saturation of the FE PL intensity is seen (higher energy densities of Figure 4.4), a competition is expected between the FE annihilation via Auger recombination and the presumed FE supply via evaporation, until their concentration stays above the Auger threshold. The quick initial decay of the FE PL under 2 mJ/cm^2 excitation supports this postulation, following which their supply from the slower EHL evaporation continues. This suggests that the rate of FE evaporation can be greater than that of FE radiative recombination in reduced dimensional systems.

At the highest excitation energy densities used, saturation of the EHL PL intensity (Figure 4.4) indicates that Auger recombination in the EHL becomes competitive. At the same time, the photo-generated FE concentration shows a quick initial decrease (Figure 4.5), signature of an Auger process. The absence of a substantial delayed rise in the FE PL intensity however, suggests that the presumed FE evaporation from the EHL is not competitive even after the Auger event. This further indicates that the faster Auger

recombination dominates in the EHL and releases free carriers from drops much faster than evaporation releases free excitons. The residual carrier concentration after a three-particle Auger event decreases approximately as the square root of the generated concentration. All subsequent processes that depend on carrier concentration, therefore, start with an initial concentration that is only sublinearly scaled with excitation. Thus, in the "saturation regime" where Auger recombination drastically changes the concentration in the EHL and that of FEs, any change brought about by FE evaporation may become relatively less significant.

An important characteristic of the decay of the EHL PL intensity is the appearance of a distinct cutoff (t_c) at t = 1.45 μs (see log scale of Figure 4.5), which is a characteristic of the decay in bulk material and is not seen at lower excitation levels. This cutoff behavior has been quite accurately modeled assuming spherical drops with a radius that vanishes at t_c, and PL intensity evolving as $(1 - t/t_c)^{1/3}$ [30, 31]. Inferring conversely from this model, the presence of a cutoff can be taken to indicate that the shape of the recombining EHL drops is close to spherical, with a radius large enough to allow sustained PL over ~ 1 μs (recall that the EHL lifespan, the same as t_c, increases with drop radius ≈ few μm in bulk Si). Since the Si films in the nanostructure are too thin compared to the typical drop size that leads to cutoff, the PL observed at this excitation energy density must originate, at least in part, from the substrate. Moreover, since the EHL lifespan is ~ 50% longer than that in the bulk, the process that facilitates this change must be associated with the nanostructure.

A model consistent with all experimental observations in the saturation regime must involve an important role of free carriers, given that both the EHL and FEs are

subjected to Auger processes. A prolonged condensation process due to an additional supply of Auger-ejected carriers and subsequent diffusion from the nanostructure to the substrate seems plausible. This implies the existence of an equilibrium between the fast Auger process (~ 10 ns) and the fast condensation process (< 3 ns), until carrier concentration decreases below the Auger threshold. In either case, under increasing excitation, the EHL appears to move towards the substrate. The continuation of the EHL PL after ~ 1 μs under energy densities ≤ 2 mJ/cm^2, unlike the "clean" accelerated decay seen in bulk Si, indicates a slower fluctuating transition of the EHL out of the liquid phase in these nanostructures and can be speculated to occur due to enhanced localization of the liquid around cluster boundaries.

In nanostructures with higher Ge content (~ 55%) in the SiGe clusters, a correlated increase of the interface PL intensity at ~ 1 μs was interpreted to be due to the re-localization of holes, released mostly from the EHL, in the deep energy wells formed by clusters [6]. The current sample, with 16% Ge content in clusters, does not show the delayed increase in interface PL, although it shows decelerations in its fast initial decay. This shows that the re-localization process not only depends on the depths of potential wells present in the respective samples, but also on the band alignment at the interfaces. Figure 4.6 compares band alignments between interfaces with varying Ge content in the clusters. The valence band alignment in low Ge content presumably offers an energy barrier for residual holes in the Si films after the decay of drops, leading to their localization in Si rather than SiGe. The interface in these nanostructures is known via EDX measurements to be more interdiffused for high Ge content nanostructures [51]. Since interdiffusion smoothens the energy band alignment at the interface, the presence

of an energy barrier for “returning” holes is indicative of reduced intermixing in low Ge content nanostructures, leading to less interdiffusion of the interfaces.

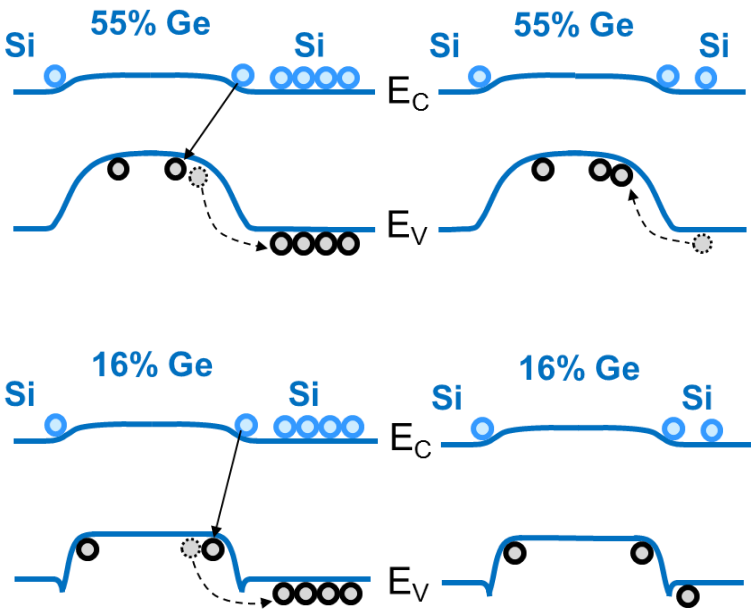

Figure 4.6 Schematic representation of recombination processes in Si/SiGe 3D nanostructures with type II heterointerfaces, for both high (55%) and low (16%) Ge content in clusters.

To summarize, the various interesting experimental results observed in this study are listed. Under specific experimental conditions, FE evaporation from the surface of EHL drops in these nanostructures can be quicker than the FE recombination rate. The lifespan of the EHL is prolonged by its localization in the nanostructure, which also changes the cutoff behavior typical of bulk material. At very high excitation levels where luminescence due to all recombination channels saturates, Auger processes enhance the

free carrier concentration that greatly influences condensation and recombination dynamics of the EHL.

In conclusion, the Auger Fountain in Si/SiGe nanostructures, previously demonstrated in high Ge content samples with deep potential wells formed by SiGe clusters, is seen to have a lower concentration threshold in low Ge content samples. Also, a re-localization of residual holes after the decay of EHL drops formed by the Auger Fountain is more effective with deep potential wells than with shallow ones. Band bending is enhanced and intermixing is reduced at the Si/SiGe interface in low Ge content nanostructures.

PL experiments using UV excitation (lower penetration depth) can be performed to better isolate substrate PL from that originating in the nanostructure. Investigations of the fluctuations in the EHL PL intensity as the liquid drops decay in the Si spacer films may lead to a more comprehensive understanding of their localization at interfaces, their possible diffusion through the nanostructure, and any interplay between condensation and Auger processes in the saturation regime.

4.2 Exciton Diffusion in Strain-engineered Nanostructures

Intermixing at Si/SiGe heterointerfaces is expected to change the luminescence properties of the nanostructure. A structure designed by varying atomic interdiffusion (described in Sub-section 3.1.1.1) in different SiGe cluster - Si layer pairs (sample B) was used; the physical extent of this intermixing was explored via electron microscopy experiments (results in Section 4.2.1) and their luminescence properties were obtained via excitation

wavelength dependent PL spectroscopy (results in Section 4.2.2). Their correlation is discussed in the final section.

4.2.1 Results of Electron Microscopy

Figure 4.7 shows a dark field TEM micrograph of sample B (Table 3.1), described in detail in Section 3.1.1. Clusters can be seen as light grey regions, forming distinct boundaries with Si films (dark grey), in most cases. Also, Si regions between clusters in individual cluster-layer pairs are uniformly intense through the nanostructure, except in the thickest layer of clusters (second cluster layer from the surface), where a relatively bright spacer is seen. Due to the high Ge content in the SiGe cluster layers, ~ 40 atomic percent (at. %), this structure is expected to have a larger maximum strain than one with lower Ge content in the clusters (sample A, for example). The distribution of this strain is visualized in the image contrast of the dark field TEM image of Figure 4.8; a general qualitative method to interpret strain distribution via contrast in TEM images was briefly described in Sub-section 3.1.1.2.

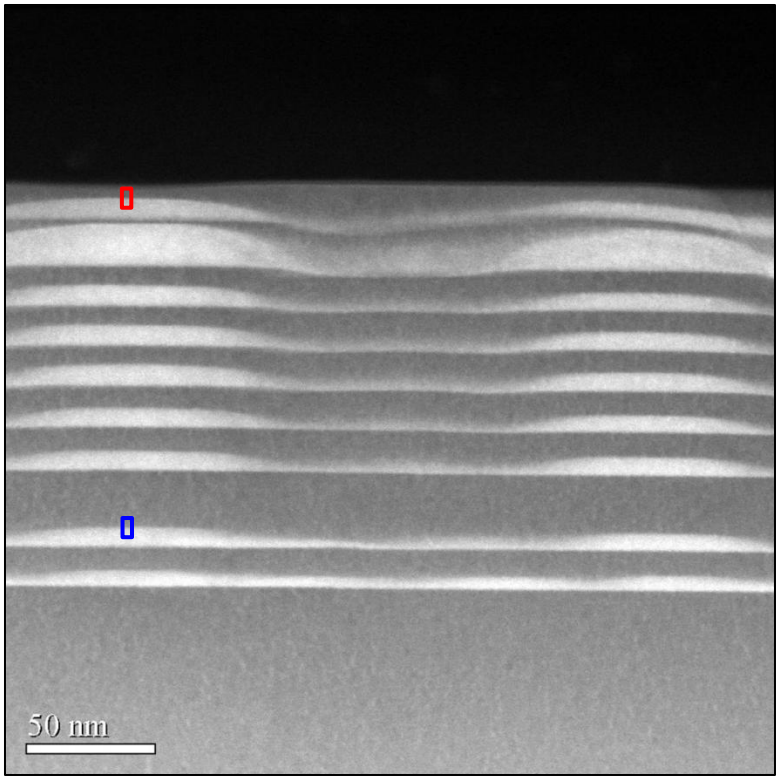

Figure 4.7 Dark-field TEM micrograph of a Si/SiGe nanostructure with a modified cluster thickness near the top of the structure. Thickness is varied to alter the strain distribution in the multilayered structure compared to typically used samples. The SiGe cluster layers are clearly seen as bright areas; the red and blue boxes indicate locations of EDX scans shown in Figure 4.9.

The image contrast in Figure 4.8 is noticeably unvarying beyond 100 nm in the substrate; the bottom of the image is taken as the unstrained reference point (labeled ‘A’) for comparison of strain in the nanostructure above. In this image, regions brighter than region A indicate tensile strain; darker regions indicate compressive strain. Both tensile and compressive strains are seen to alternate through the nanostructure, not just between cluster-layer pairs, but also inside individual clusters and layers. Regions of differing thicknesses of both Si thin films and SiGe cluster layers show differences in strain distribution and are identified as regions B through E in the TEM image.

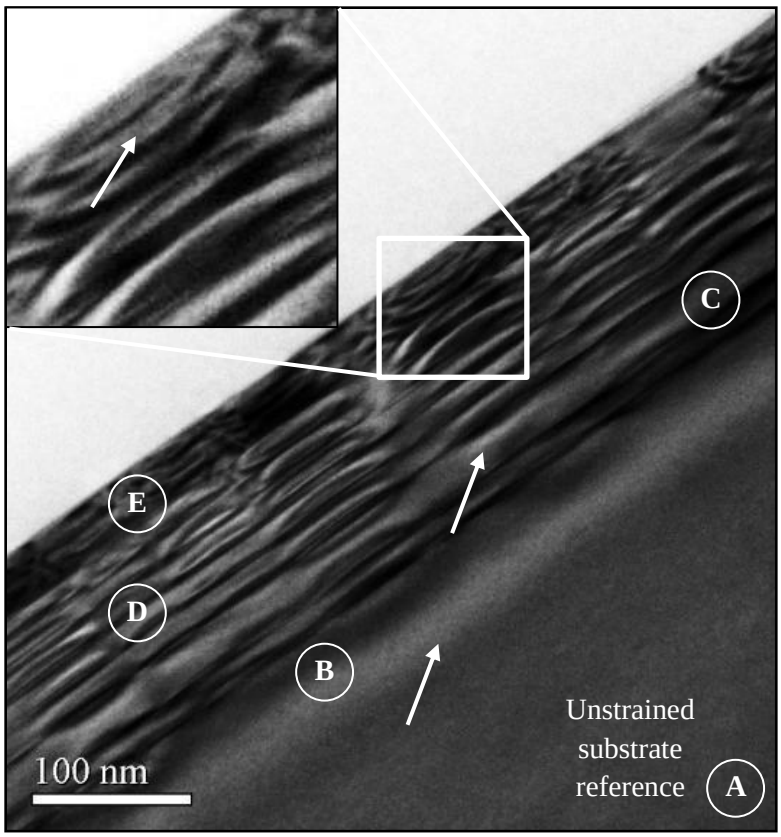

Figure 4.8 A <200> two beam dark field TEM image of a modified Si/SiGe nanostructure (description in text), showing the regional distribution of strain. Light areas indicate tensile strain and dark regions are compressively strained relative to the substrate, which is unstrained at a sufficient depth. Regions A – E show differences in strain distribution (discussed in text), which is highlighted for a region near the surface (inset) by increasing its image contrast.

Just below the surface of the original substrate (region 'B'), the observed variation in image intensity (relative to region A) extends ~ 70 nm into the substrate indicating that locations within in the substrate are strained by the growth of the nanostructure above. The relatively thick region over which most of the tensile strain is accommodated is indicated by an arrow. Recall that the strain at any point in the crystal, in the growth direction, is determined by a linear superposition of strain due to individual epitaxial layers. Since the magnitude of the strain field decreases with distance from the

source of strain, the strain at a point receives its largest contribution from adjacent layers. The substrate is influenced most by the first layer of SiGe clusters. From region B in Figure 4.8, it is seen that the strain due to a single layer of clusters in the nanostructure, for the Ge content used, may require more than 70 nm of unstrained Si to be completely accommodated.

The spatial limit (thickness) of the Si sandwiched between cluster layers changes local strain in its lattice. Region 'C', a 35 nm thick Si layer, shows a higher contrast (brighter, see arrow) than that in region B, indicating larger tensile strain than that in the substrate. The contrast in the ~ 8 nm thick standard Si layers of region 'D' shows an even larger tensile strain compared to both regions C and B. Accordingly, the highest contrast is expected in the 3 nm Si layer of the region marked 'E'. A closer examination of the region however (contrast exaggerated in inset), does not indicate a higher image intensity (arrow in inset). It is possible that either strain fields from adjacent layers overlap at this extremely thin region, or the lattice constant does not sufficiently relax due to the presence of SiGe clusters sandwiching this Si film. With increasing distance from the substrate (increasing volume for elastic relaxation underneath), heavily strained (brighter) regions within the Si layers are seen to get thinner and their maxima are seen to move towards the top of the films.

Figure 4.9 shows Ge content extracted along locations indicated by boxes in Figure 4.7, top to bottom, via EDX scans. A comparison of the Ge atomic percent (at. %) of the topmost cluster layer (red) and a near-substrate cluster layer (blue, second from bottom) shows that the Ge content in top clusters initially increases twice as fast as that in bottom clusters, with distance into the cluster. Also, the top cluster Ge content reaches its

maximum in a shorter distance (~ 6 nm) compared to bottom clusters (~ 9 nm), making it clear that top SiGe clusters have a more abrupt interface with overlying Si layers than bottom clusters.

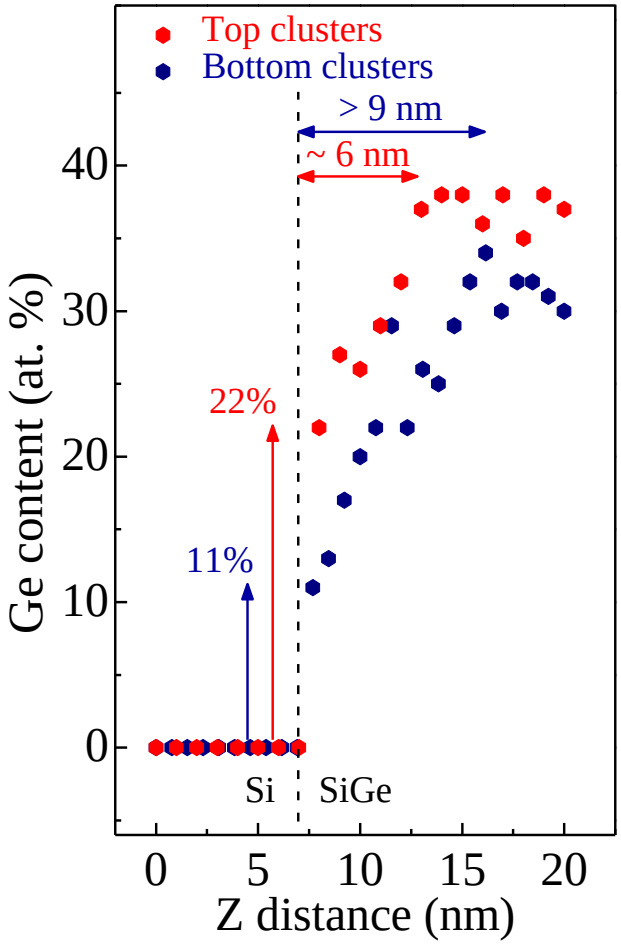

Figure 4.9 EDX depth profile of two SiGe clusters: one near the surface of the nanostructure (top, red) and the other closer to the substrate (bottom, blue), shown in colored boxes in Figure 4.7.

Figure 3.4 showed a bright field cross-sectional TEM image of the nanostructure. Figure 4.10 shows a similar image obtained from a different location on the sample,

containing a single dislocation in the [111] direction. A closer view of the image highlighting the apparent termination of the dislocation is also shown. It is seen that the dislocation does not propagate through to the top of the nanostructure, but stops before reaching the thickest layer of SiGe clusters, in this image of the cross section of the sample along <110>.

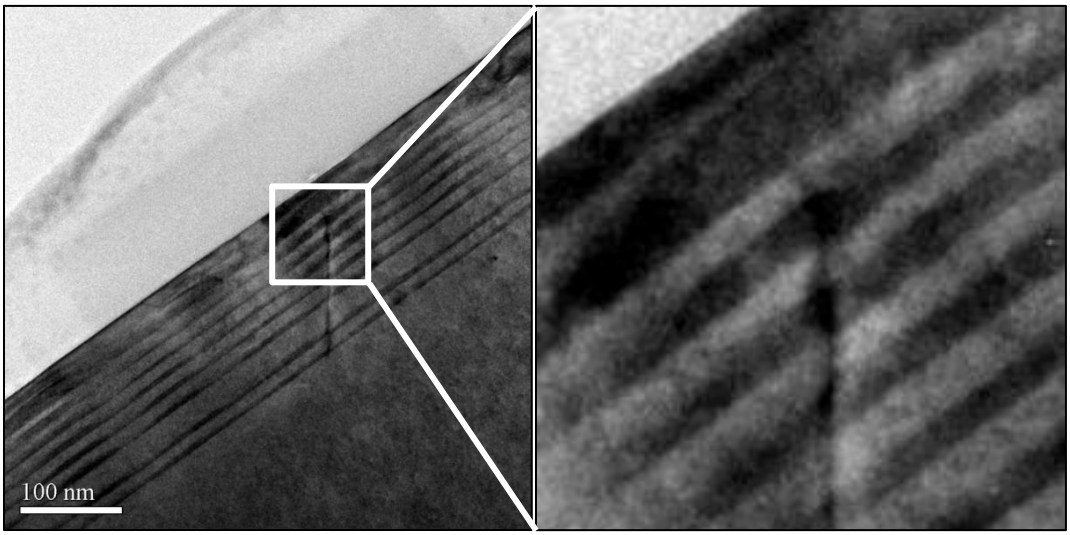

Figure 4.10 A bright field TEM image of the <110> cross section of a strain engineered Si/SiGe nanostructure, showing a close view of a [111] dislocation. Note that the dislocation does not propagate past the thickest layer of SiGe clusters, in the growth direction.

Note that this does not indicate an absolute termination of the dislocation, but only that in the growth direction. It is energetically most favorable for dislocations to glide to the end of the wafer during processing [68], and their propagation out of the imaged <110> plane (in and out of the plane of the paper) as they reach a wafer edge should be factored in interpreting PL data.

4.2.2 Results of Photoluminescence Experiments

Figures 4.11 and 4.12 compare the PL spectra obtained under approximately the same excitation intensity and the indicated excitation wavelengths. Using 514 nm excitation, the PL spectrum exhibits a peak associated with c-Si at ~ 1.1 eV and a number of PL lines associated with dislocation luminescence (D lines) at ~ 0.98 eV (D4), ~ 0.87 eV (D2) and ~ 0.81 eV (D1) [10]. The PL spectrum under 488 nm excitation is very similar to that under 514 nm excitation. Under 457 nm excitation however, the PL at ~ 1.1 eV associated with c-Si disappears, but the D lines persist. Figure 4.12 compares PL spectra acquired using lower excitation wavelengths. Under 405 nm excitation, we find a significantly different PL spectrum, without the sharp peaks associated with D-line PL. The total PL intensity (area under PL features) is the largest for this excitation wavelength. The PL spectrum under 325 nm is significantly narrower; shows no trace of the D-line PL, and the PL peak is shifted toward lower photon energies (“red” spectral shift). Its FWHM is ~ 100 meV, while that under 405 nm is ~ 130 meV, changed mainly towards higher energies.

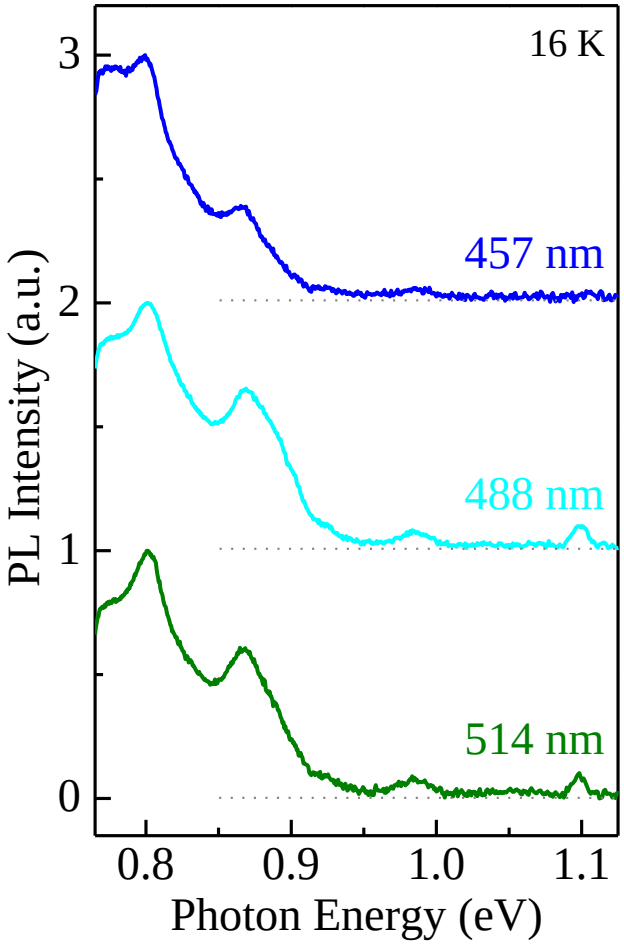

Figure 4.11 Low temperature PL spectra of a Si/SiGe nanostructure with a TEM-observed dislocation, for various visible excitation wavelengths (indicated). PL attributed to dislocations is seen. The spectra are normalized and vertically shifted for clarity.

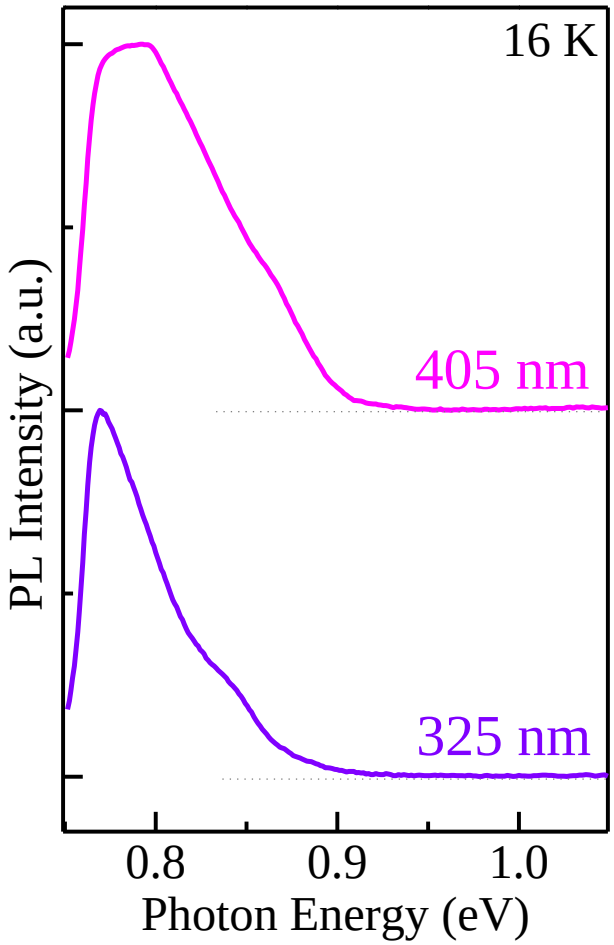

Figure 4.12 Low temperature PL spectra from a Si/SiGe nanostructure with a known dislocation obtained using excitation wavelengths with ~ 10 nm penetration depths. The spectra are normalized and vertically shifted for clarity.

4.3.3 Discussion

Although the presence of a dislocation in the nanostructure makes the inference about strain fields complicated, several observations can be made from electron microscopy data. Any inference from the PL data need to account for the observed dislocation in the structure. The absence of the highest strain field in the 3 nm Si film is presumably because of an overlap of strain fields from adjacent layers, which dominates over lattice

mismatch-induced “intrinsic” strain. The decreasing thickness of bright regions in Si films moving away from the substrate (Figure 4.8) indicates that in progressively higher Si layers, more strain is accommodated by the structure underneath. This may occur because of the volume conservation requirement for strain relaxation given the differences in elastic moduli of the anisotropic crystal [69]. Thus, a Si layer at the top of the structure would be strained more than a middle or bottom Si layer, even if their thicknesses were identical. It follows that the 3 nm thick Si layer near the surface, sandwiched between layers with larger average lattice constants and a relatively large volume for elastic relaxation in the structure underneath, has a larger biaxial tensile strain than underlying Si layers. In the absence of a useful separation of contributions from different strain fields, the analysis is restricted to select regions of the structure where the overlap is expected to be reduced.

The EDX scans of Figure 4.9 clearly show that the upper surface of the topmost clusters have more abrupt interfaces than those of clusters located towards the bottom of the nanostructure. This is important because excitation wavelengths used in certain PL experiments penetrate only into the top cluster-layer pair (see Figure 3.9). The enhanced abruptness of the topmost cluster layer presumably results from reduced intermixing of underlying Si into the clusters during their growth. Lower lying SiGe clusters are exposed to the growth temperature for progressively longer times. Using a typical MBE growth rate of several angstroms per second, the bottommost clusters are exposed to 645 °C for about an hour, versus ~ 10 minutes for the topmost layer. Besides thermally activated atomic diffusion, strain-induced intermixing during growth is also expectedly less for the topmost clusters, given the reduced lattice mismatch with the heavily strained Si thin film

underneath. In comparison with the topmost clusters, intermixing between the thickest clusters (second from top, Figure 4.7) may be enhanced not only due to a longer process time and smaller underlying lattice constant, but also due to a higher surface energy given their shorter radius of curvature relative to other cluster layers [37, 46].

Structural properties of the nanostructure show a clear correlation with the luminescence properties obtained by probing through varying depths through the multilayers. For photoexcitation reaching the bottom of the nanostructure (514 and 488 nm wavelengths, with an estimated ~ 17% and ~ 5% absorption in the substrate respectively, from Figure 3.9), the PL lines related to bulk Si and to dislocations are both observed (Figure 4.11). The disappearance of the Si PL under 457 nm excitation clearly indicates that this excitation does not reach the substrate. A conservative estimate also suggests that > 99% of this excitation is absorbed well before reaching the substrate (Figure 3.9). These observations show that the PL due to FE recombination in Si films in the lower part of the nanostructure is lost in the presence of strong carrier diffusion sinks (dislocations), indicating a quick redistribution of carriers that may otherwise form excitons.

For photoexcitation with a shorter penetration depth of ~ 16 nm using 405 nm excitation wavelength (Figure 4.12), an estimated ~ 95% of the excitation is absorbed above the highest observed point of the dislocation. Thus, any contribution to the PL due to D-lines should not be significant. The PL spectrum under 325 nm excitation (~ 6 nm penetration depth) clearly shows no Si or D-line PL (Figure 4.12). These data indicate that photogenerated carriers localized at the top of the nanostructure, which most likely form excitons at the experiment temperature, have a diffusion length $L_D < 4 \times 10^{-6}$ cm in

the z-direction (direction of growth). For comparison, the L_D of an electron in device quality Si at low temperature might approach 10^{-1} cm [70], while for a free exciton in 10^{-4} cm wide Si wires, L_D approaches 10^{-3} cm [71]. Strongly supported by the observation of interface luminescence in the vicinity of classic carrier diffusion sinks, the upper limit for the diffusion length of carriers in the nanostructure, in the vertical direction can be said to be ~ 40 nm. It is likely that carrier diffusion over this length is further restricted due to the presence of potential wells for holes formed by wetting layers.

Based on the assumption of a type II energy band alignment at the Si/SiGe heterointerface [4, 61, 63-66], and the observed spectral properties, we can infer further about the role of interface abruptness and chemical composition on radiative recombination at the Si/SiGe heterointerface. This is illustrated in Figure 4.13. Selective excitation used in this experimental technique is idealized to assume that one excitation (325 nm) generates carriers only in the topmost cluster-layer pair, whereas the other (405 nm) additionally includes the next pair with the thickest clusters. This idealization is justified not only by an understanding of penetration depths of the excitations, but also by the absence of significant D-line PL in spectra acquired under 405 nm excitation. The red spectral shift and spectral peak narrowing under 325 nm excitation, compared to 405 nm excitation, are then explained by the isolation of the PL seen from the topmost cluster-layer pair.

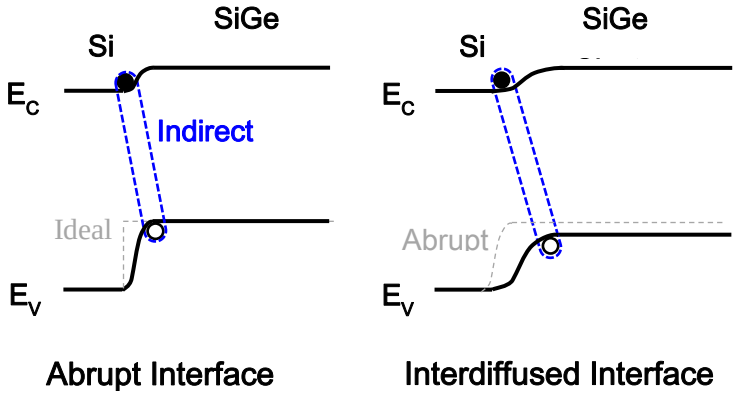

Figure 4.13 Schematic representation of recombination at Si/SiGe heterointerfaces with different extents of intermixing. The abrupt interface is seen in the topmost clusters of the strain-engineered nanostructure (compare with ideal interface shown, dashed), whereas an interdiffused interface is seen in lower clusters (compare with abrupt interface shown).

In all Si/SiGe heterostructures (bulk and low dimensional), a higher Ge content corresponds to a narrower bandgap due to an increase, mostly in the valence band offset, and their PL spectrum is correspondingly red-shifted [4, 9, 61]. With enhanced intermixing in the thickest cluster layer, its average Ge concentration is anticipated to be less than that of topmost clusters. PL arising from this or lower regions, with lower Ge content seen in EDX scans (Figure 4.9), must peak at a higher energy than that from topmost clusters.

The ~ 30 meV decrease in FWHM of the PL features obtained by selectively exciting just the topmost clusters, compared to that by exciting two cluster layers, is directly explained by the difference in their stoichiometric composition. Energy bandgaps are well characterized as a function of Ge content [44] and that between the heavy hole valence band and the lower Δ conduction valleys is found to vary as ~ 7 meV per at. %

Ge. Thus, excitons localized at interfaces with Ge content lower by ~ 4 to 5%, can produce PL at energies larger by ~ 30 meV, superposing on PL from the topmost layer.

This model also explains previously observed experimental results. A study of the temperature dependence of PL quenching in Si/SiGe nanostructures with uniform thickness of the cluster-layer pairs, had revealed two different activation energies attributed to distinct physical mechanisms [72]. An activation energy ranging between 10 to 15 meV was associated with the exciton binding energy [9], and a second > 100 meV activation energy was attributed to hole thermionic transport over valence band energy barriers at Si/SiGe hetero-interfaces [72]. It is reasonable to assume that at low temperatures (< 50 K), excitons are localized at compositional fluctuations at Si/SiGe cluster hetero-interfaces. An observed variation of the exciton thermal dissociation energy (~ 5 meV) most likely corresponds to an average energy bandgap fluctuation that varies between cluster-layer pairs through the nanostructure.

In summary, it is seen that the photoexcitation penetration depth determines PL properties in structurally non-uniform Si/SiGe 3D multilayers and the exciton diffusion length is unusually short, < 40 nm, in the vertical direction. In the proposed model, excitons are strongly localized at the Si/SiGe cluster hetero-interface, and the PL spectrum reflects the Si/SiGe heterointerface abruptness and chemical composition. It also confirms that dislocation penetration is restricted to layers closer to the Si substrate.

With exciton diffusion lengths < 40 nm, future endeavors may increase capping layer thickness to ~ 40 nm to reduce surface recombination of localized indirect excitons to increase the overall PL quantum efficiency.

4.3 Reversible Degradation of the Photoluminescence Intensity

The luminescence properties of freshly-grown Si/SiGe nanostructures are generally studied by cooling samples to low temperatures and performing PL experiments. Acquisition procedures are usually completed in a few minutes. After several cycles of cooling, performing experiments, and restoring a sample to room temperature, it was found that the low temperature luminescence intensity of samples degraded when subjected to several minutes of continuous photoexcitation. A study of the degradation mechanism was undertaken. It is found that Auger recombination plays a significant role in the overall degradation process; this postulation is developed in this section.

Results from PL experiments reported in this section were obtained using sample C (see Table 3.1). Figure 4.14 shows two PL spectra recorded at 16 K under 405 nm, ~ 0.1 W/cm^2 excitation: first without prior exposure (initial) and second after ~ 20 minutes of continuous exposure (fatigued). In the initial PL spectrum, two distinct PL features peaked at 0.82 eV and at 0.88 eV can clearly be seen. After continuous exposure, both PL features become less intense, with the 0.82 eV PL peak losing nearly 75% of its initial intensity and the 0.88 eV PL peak losing less than 50%. In the fatigued PL spectrum, the full width at half maximum (FWHM) of both PL features obtained by applying Gaussian fits, increases significantly, by more than 50%. Fatigued PL spectra are not completely restored even after several hours of incubation in the dark at low temperature; a complete recovery requires warming the sample to temperature $T > 250$K.

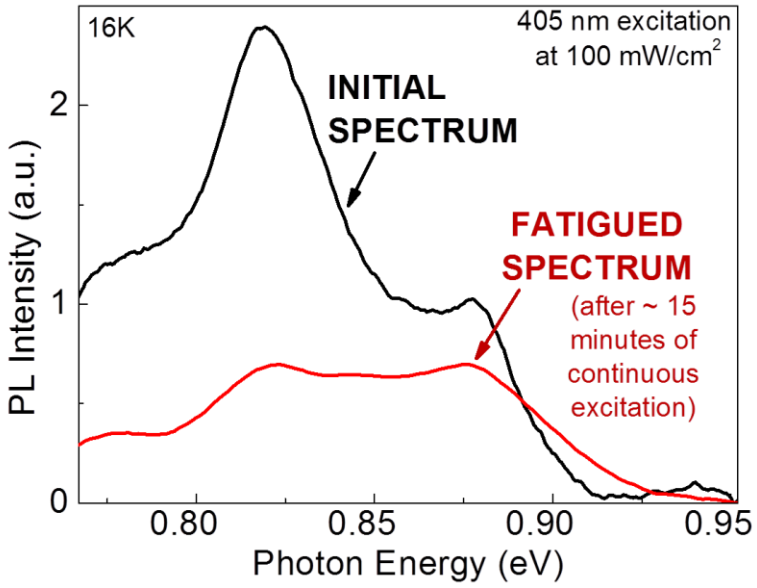

Figure 4.14 Low temperature PL spectra of the Si/SiGe nanostructure of sample C obtained before and after ~ 15 minutes of continuous excitation; 405 nm excitation was used at 100 mW/cm^2.

The evolution of the PL intensity under 405 nm excitation and two excitation intensities (150 and 15 mW/cm^2) recorded at 0.82 eV is shown in Figure 4.15. When irradiated at 150 mW/cm^2, a slow PL intensity degradation is observed for ~10 minutes, after which a much faster degradation reduces the PL intensity to ~ 10% of its initial value. Under the lower excitation intensity of 15 mW/cm^2, any slow PL intensity degradation is essentially undetectable, and the initial period of relative stability lasts ~ 15 min. This is followed by a fast PL intensity degradation, also until ~ 10% of the initial PL intensity remains. In both cases, the PL intensity stabilizes after the fast degradation period. The PL fatigue is detectable only when using excitation wavelengths $\lambda \leq 405$ nm, but not when using excitation with a wavelength ≥ 457 nm.

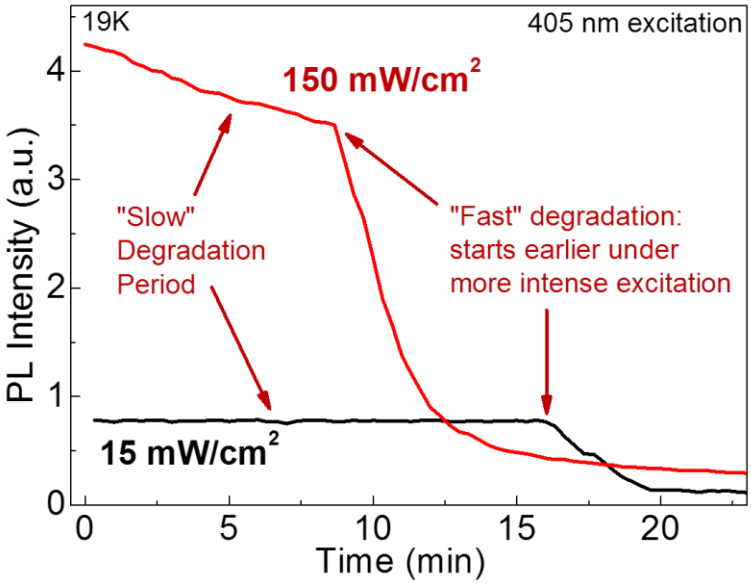

Figure 4.15 Excitation Intensity dependence of the evolution of the 0.82eV PL spectral feature of the Si/SiGe nanostructure of sample C. "Slow" and "Fast" degradation periods are seen; note that the onset of the rapid fall occurs earlier under higher intensity excitation.

Figure 4.16 shows the PL intensity degradation as a function of time under ~ 50 mW/cm^2 CW excitation (using 325 nm wavelength) recorded at different temperatures. The PL fatigue is clearly observed at $T \leq 50$ K, and is not found above 65 K. A similar result was obtained using 405 nm excitation.

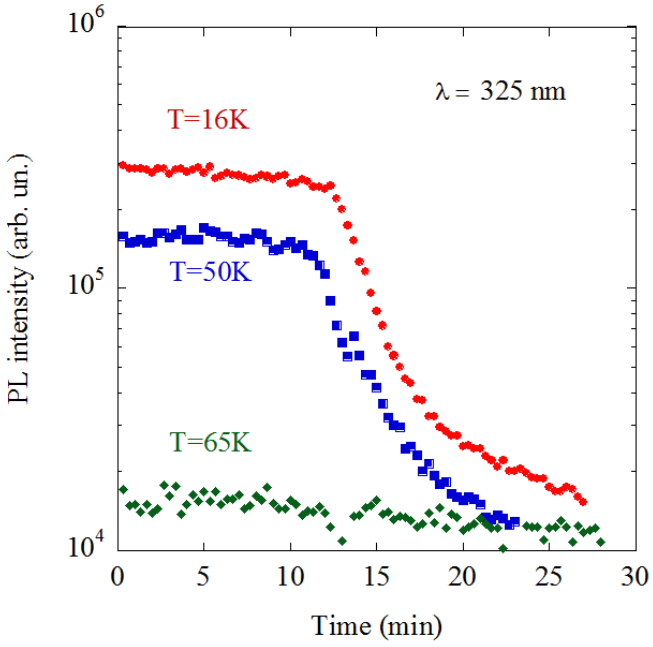

Figure 4.16 PL degradation of the Si/SiGe nanostructure of sample C recorded at 0.82 eV at various temperatures (indicated). The 325 nm CW excitation was used at 50 mW. The rapid PL degradation after ~ 10 minutes at lower temperatures is not seen at 65 K.

It is well known that the reversible PL degradation associated with photo-induced structural changes requires high temperature annealing to restore the initial PL intensity [73-76]. Since the observed PL fatigue is a low temperature phenomenon (Figure 4.16), and it can be restored by just warming the sample to $T > 250$ K, we think that this effect is primarily associated with accumulation and retention of charge in SiGe clusters. A change in sample temperature may explain one, but not both observed rates of the degradation. Degradation of the PL intensity from an ensemble of quantum dots (QDs) is proposed to be due to Auger autoionization. The PL intensity blinking in individual QDs has been described by a statistical difference in the lifetimes of charged and neutral states [16] (see Section 2.3). Since Si/SiGe heterointerfaces exhibit a type II energy band

alignment, contribution of the Auger processes in overall carrier recombination can be significant even at relatively low carrier concentration, specifically if carriers are strongly localized [6]. Energy band offsets for holes localized in SiGe clusters and electrons localized in Si layers, both increase with increasing Ge content. In Si/SiGe nanostructures, energy wells for holes associated with SiGe clusters are quite deep (up to ~ 400 meV [4]). At low temperatures, holes cannot overcome these energy barriers to diffuse, even under large concentration gradients, and transport of holes is, most likely, limited to tunneling [72]. Electrons however, are only weakly localized at the Si/SiGe heterointerface, and are more mobile compared to holes. In this model, the observed degradation of the PL intensity could be explained due to a net accumulation of holes within SiGe clusters and enhancement of Auger recombination.

It has been proposed that the two prominent PL spectral features observed in Si/SiGe nanoclusters (similar to those seen in Figure 4.14) correspond to the recombination of excitons localized within regions of different Ge compositions, presumably more Ge for the PL peaked at 0.82 eV and less for the PL peaked at 0.88 eV [61]. It is suggested that charge accumulation (holes captured within SiGe clusters) enhances Auger recombination, and that this process affects PL more effectively at Ge-rich regions of SiGe clusters (SiGe cluster core [4, 6, 45, 51, 72]) with correspondingly deeper energy wells for holes. The increase in FWHM of PL peaks could be caused by SiGe cluster charging and redistribution of the built-in potential at the Si/SiGe heterointerface.

Compared to holes, electrons are weakly localized and may have a fairly unobstructed path for diffusion through the contiguous Si spacing layers. Since the PL

fatigue is observed under a short excitation wavelength, surface states may serve as diffusion sinks for electrons. This is not the more likely cause for the observed features of the degradation however, since the phenomenon appears only after repeated thermal cycling. Also, surface states are classically known to offer a continuum of states that serve as centers for system relaxation via non-radiative recombination, not carrier trapping that leaves the system excited. Additionally, only a small portion of the total excitation intensity is absorbed in the nanostructure under longer wavelength excitation, which implies that an Auger threshold responsible for the fatigue (explained below) may not be reached when using longer wavelengths for excitation, and consequently, the PL fatigue would not be observed. Dislocations however, are well known carrier traps. Specifically, electron traps at dislocations are known to have a ~ 10^4 times greater capture cross section than those for holes [77]. Thus, dislocation related traps are believed to be the most likely destination sites for electrons.

If thermally-activated electron diffusion were the only cause of PL fatigue, one expects a single rate of change of the PL intensity that continues to degrade the PL until most trap states are filled. But the sudden change in this rate strongly suggests the presence of at least two distinct processes, the earlier of which presumably enables the latter. It is inferred that electron loss must continuously change the neutrality of the photoexcited region, leading to the onset of the fast degradation period.

Similar experiments were performed on similar samples (with 10 bilayers, not 5 as in this sample) with dislocations in the substrate inadvertently introduced during growth, which were detected by TEM imaging. In these samples, similar PL degradation was seen under 457 nm photoexcitation, which penetrated further into the nanostructure,

indicating that structural defects could be actively involved in the degradation process. When using equally intense, even longer wavelength excitation, this effect is not seen for several tens of minutes, indicating that the longer penetration depth of the excitation (comparatively less generation in the nanostructure) does not produce sufficient carriers taking part in the process. This also indicates that carriers eventually occupying trap states mostly originate from the nanostructure, not the substrate.

Hole accumulation in SiGe clusters must change carrier-carrier interaction in the nanostructure, and consequently, the rate of processes that result from such interaction. As accumulation increases, one expects the rate of Auger recombination to increase. In the context of the experimental conditions, the observed rate of PL degradation is proportional to the number of electron-hole pairs N, localized within the neighborhood of a single SiGe cluster: $dN/dt = -\gamma N$, where γ is the decay rate, assumed to be constant through the decay. Therefore, the number of electron-hole pairs at any instant is given by: $N(t) = N_0 \exp(-\gamma t)$, where N_0 is the number of generated electron-hole pairs and γ, the decay rate, is the net probability of events that cause the PL degradation. The resulting concentration of accumulating holes is $N_0 [1 - \exp(-\gamma t)]$. The effective rate of Auger recombination, which increases as positive charge is accumulated in the clusters, is given by $C \times N_0 \exp(-\gamma t) \times N_0 [1 - \exp(-\gamma t)]$, where C is the Auger rate constant. Using the Auger rate constant of 2.3×10^{-31} cm^6/s (similar for both bulk Si and bulk Ge, obtained by interpolation), the above expression is plotted in Figure 4.17 using $N_0 = 200$ electron-hole pairs per SiGe nanocluster (not necessarily distributed uniformly), and $\gamma = 4 \times 10^{-6}$ s^{-1} [15, 19]. The use of these values for N_0 and γ is explained below. For comparison, the rate of radiative recombination is also shown in the figure. It can be seen that according

to this estimation, the evolving rate of Auger recombination begins to compete with that of radiative recombination after ~ 10 min, explaining the onset of the fast PL intensity degradation.

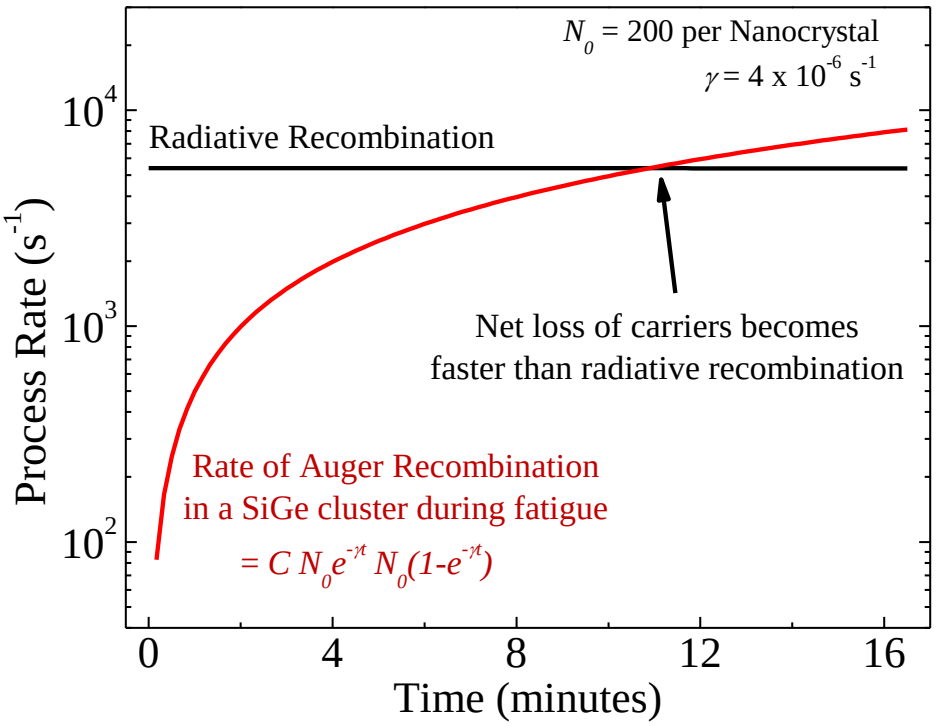

Figure 4.17 Evolution of the rates of radiative recombination and Auger recombination in individual nanoclusters. Calculations are shown for an Auger threshold (N_0) of 200 electron-hole pairs/cluster and a carrier loss rate (γ) of 4 × 10^{-6} s^{-1} (C = Auger rate constant).

For an Auger event to occur, the local carrier concentration must be larger than the threshold for Auger recombination. Since carriers in the nanostructure exist as surface excitons (localized at heterointerfaces), a simple estimation of this threshold is done by assuming that carrier-carrier interaction becomes important when the surface area of the cluster is tightly occupied with surface excitons. With stoichiometric fluctuations in SiGe

clusters, holes inside cluster boundaries are not expected to be distributed uniformly; more importantly, hole-hole interaction is expected to be stronger due to their spatial confinement, than electron-electron interaction, which may give rise to small differences in this crude approximation.

The number of electron-hole pairs leading to enhanced carrier-carrier interaction is approximated by the ratio of the surface area of a nanocluster (~ 2×10^{-10} cm^2, from Section 3.1.1) to that covered by an exciton at the interface ($\pi {r_{Bohr}}^2$, where r_{Bohr} is the radius of the Bohr exciton in Si, ~ 5×10^{-7} cm), which yields the value ~ 250 per nanocluster. Recall that Auger processes have lower thresholds given the low dimensionality of the system; it is possible that this number overestimates the threshold.

It is necessary to match the observed decay rate (γ) to a rate-determining subprocess in the proposed mechanism. Although thermal-activation and trapping are experimentally seen to contribute to the overall mechanism, these are not rate-limiting subprocesses. The remarkable similarity of this very small rate between these nanostructures and that in II-VI QDs necessitates a rigorous comparison of the two. In core-shell II-VI QD systems, PL degradation is presumably initiated by charging of QDs due to Auger autoionization events [16]. A charged QD is eventually neutralized by the return of the Auger-ejected carrier, but typically stays in the charged state for a longer period than in the neutral state. The PL intensity from an ensemble of QDs decreases with the characteristic time of minutes, explained by the statistical difference of lifetimes in these states [16]. Compared to II-VI QDs, which are typically a few nanometers in diameter and exhibit a type I energy band alignment [18], Si/SiGe 3D nanostructures are larger in size with a type II energy band alignment at Si/SiGe heterointerface. Since

electron-hole pairs are spatially separated in regions where energy levels are not quantized, Auger autoionization is not expected to be equally likely in these structures. The absence of a slow degradation period further indicates that a fundamental process that leads to charge accumulation is different in the two systems. Despite the unlikeliness of Auger Autoionization (where discrete energy states are required), Auger processes are routinely encountered in low dimensional systems, and as will be shown in the next section, are highly probable at Si/SiGe heterointerfaces.

The rate determining factor in the slow PL decay seen in QDs is not the nanosecond long Auger autoionization event itself, but the slowest event in the pathway of the Auger-ejected carrier that enables its return. Events in this pathway depend on several parameters of the II-VI system and the matrix in which dots are embedded [15-21]. For every electron-hole-pair created in the QD system, the probability that an ejected carrier does not complete this pathway, i.e., the probability of ionization per photoexcitation event, is ~ 10^{-6} [15, 19]. Thus, although autoionization may not be likely in the current nanostructure, a similar mechanism may explain PL degradation: the pathway of an electron may be initiated by an Auger event, but involve a subsequent rate-limiting step. Several processes that constitute the electron pathway, from their origin in the nanostructure to their trapping, could potentially be rate-limiting; without further experiment, the identification of this process would be purely speculative. The transport of carriers returning from traps however, can be ruled out, inferring from the negligible restoration of luminescence after more than 8 hours of incubation at 19 K. Since it is known that the probability of a sub-process in QDs can be on the order of 10^{-6}, a subprocess in the current pathway can be expected to have an equivalent probability.

The structural change brought about by thermal cycling of the nanostructure is not well understood. No structural change is expected in a Si/SiGe nanostructure at or below room temperature, because of the high activation energy of interdiffusion of Ge atoms in Si (~ 4.7 eV [78]). Also at the experiment temperature, motion of dislocations is not possible [48, 68]. Thus, any change to dislocations that leads to the creation of trap states by repeated thermal cycling between low and room temperatures is not associated with atomic diffusion or motion of dislocations. A speculative possibility is a temperature-dependent, reversible change in the tetragonal symmetry of atoms along dislocations in the strain-relaxed substrate.

The restoration of PL intensity in a fatigued sample is seen to proportionally increase with the temperature to which the sample is warmed: partial warming to temperatures below room temperature restores the intensity only partially. This qualitatively indicates that thermally de-trapped carriers occupy deep-level states. Without a value for the activation energy for the de-trapping process, a comparison of the nature of trap states with that of known dislocation lines or other defects remains incomplete. A study of the temperature-dependence of the restoration of PL intensity can be done to obtain an activation energy of the de-trapping process, which would enable a comparison with previously reported trap states [77].

Since carrier trapping is exacerbated by thermal cycling, the effect of heating samples above room temperature after observing PL fatigue is of interest. The interdiffusion of atoms depends exponentially on temperature; this high activation energy (> 4 eV) process is not expected to be important unless temperatures approaching the processing temperature (~ 645 °C) are used. The heating suggested here is on the order of

a few tens of degrees above room temperature, to study possible resetting of structural changes induced by thermal cycling.

Despite the incomprehensive knowledge on γ, the nature of the PL degradation described above and its constituent subprocesses are now better understood. In contrast with previously reported PL fatigue mechanisms, this process begins after a few minutes of continuous photoexcitation. The observed PL intensity degradation can be fully erased by warming samples to $T > 250$ K. According to the proposed model, a significant decrease in the PL intensity is explained by the accumulation of holes within SiGe nanoclusters and a consequent enhancement of Auger recombination. Slower processes involving thermally-activated carrier transport to trap states enable charge accumulation.

CHAPTER 5

RECOMBINATION PROCESSES IN SILICON-ON-INSULATOR THIN FILMS

The study of recombination processes in the Silicon-On-Insulator (SOI) system focusses on the dynamic interplay between free excitons (FEs) and the electron-hole liquid (EHL), and the influence of the Si/SiO_2 interface on their luminescence, under the reduced dimension of the liquid in the Si film of SOI. Examination of the photoluminescence (PL) intensity through spectral and time-resolved measurements enables the necessary analysis; rate equations are used to describe various processes that occur in the thin film in the presence of the interface.

The Si/SiO_2 interface in SOI wafers can greatly influence properties of electronic and possible optoelectronic devices. Interfaces with dangling Si bonds (incomplete passivation) typically serve as centers for non-radiative recombination. For nanoscale structures, these centers often lie within one diffusion length of a generated carrier, and play a much greater role in de-exciting the system to the ground state than their macroscale counterparts. The thickness of the Si thin film in SOI substrates and the quality of passivation determine the surface recombination velocity, and thus influence the lifetime of the PL. Measurement of the PL lifetime of the EHL has been used by Tajima and coworkers to assess the quality of ~ 200 nm thick Si layers in SOI wafers [62, 79]. The EHL PL lifetimes recorded at 4 K were consistently in the 100 ns range for the EHL; a longer lifetime of the EHL PL was taken to correspond to lower interface defect densities [80]. But the change in lifetime between their best and worst samples is rather

small and the corresponding estimation of trap densities yields very similar values for samples prepared by significantly different procedures. More importantly, at the same levels of excitation, they claim that the FE lifetime is ~ 10 ns or less. Since the FE lifetime in high purity bulk Si is well known to be on the order of a few μs, as reported by other groups that have also reported 100 ns EHL lifetimes [6, 81], it becomes important to validate this reported reduction in SOI thin films. Also, while these reports show or mention the non-exponential behavior of the decay of the EHL PL, they do not elaborate on its underlying mechanism. In addition to these reasons, the evaluation of changes to Si PL brought about by a Si/SiO_2 interface is perceived to be important for Si-based optical waveguide-type applications.

In the work by Tajima and coworkers [62, 79, 80], performed on 54 – 320 nm thick Si layers, surface recombination was seen to greatly influence, even control carrier lifetimes. The enhanced spatial confinement of generated carriers in such thin films increases the density of electron-hole pairs (EHPs) and influences various processes that depend on it. The role of the interface in the overall recombination process, especially recombination in the EHL, as analyzed by PL experiments, is therefore obscured by competing processes. This work uses a 2 μm thick Si film, which better delineates the influence of the Si/SiO_2 interface on EHL recombination than ~ 100 nm thick films. While 100 ns dynamics are seen in the current work, several features of the interplay between FE and EHL recombination are also observed, and signature traits of Auger processes are absent even at high carrier concentrations.

The decay of EHL PL in Si, with a critical temperature for condensation T_c = 26 K, shows an interesting difference with that in Ge (where T_c = 6.5 K): the non-

exponential nature of the decay curve in Ge is strongly dependent on temperature *T*. Below 2 K, EHL decay in Ge becomes exponential, whereas no such temperature has been reported for Si. This is attributed to the reduction of evaporation of carriers from the drop surface [29], which is proportional to $T^2 \exp(-\varphi/k_B T)$: a strongly temperature dependent process (φ is condensation energy). Thus, as temperature is decreased below a certain value (currently unknown), an increase in the lifetime of the EHL PL in Si could be expected, as in the case of germanium. At liquid He temperature, the reported lifetime is still in the 100 ns range [62] indicating that evaporation is important at least until 4 K, more so at higher temperatures up to T_c. Beyond T_c, PL due to the electron-hole plasma is seen, even up to room temperature. Experiments in the current work are performed at 17 K, wherein evaporation is expected to influence EHL recombination.

The second harmonic of the Nd-YAG, 6 ns pulsed laser (emitting at 532 nm) was used in PL experiments performed to study the SOI system. Using parameters in Table 3.2, the excitation intensity at the Si/SiO_2 interface at the end of the 2 μm thick Si layer is estimated to be ~ 21% of that at the sample surface, which is not a significant reduction. If the excitation generates EHPs well above the critical density for condensation, liquid drops can be expected to be present throughout the layer, rather than just close to the surface. Moreover, if the excitation is high enough, they can also be formed in the Si substrate beyond the oxide.

5.1 Results from Photoluminescence Experiments

Figure 5.1 shows PL spectra acquired at 17 K under 532 nm pulsed laser excitation, using different energy densities of the 6 ns excitation pulses. Under the lowest energy density

used, a peak at 1.096 eV is the only distinct feature of the mostly featureless spectrum. Upon increasing the energy density, the intensity of this peak increases, and a second, broader peak appears at 1.083 eV. Further increases in energy density result in modicum increases in the PL intensity of the 1.096 eV peak, but significant increases in that of the 1.083 eV peak.

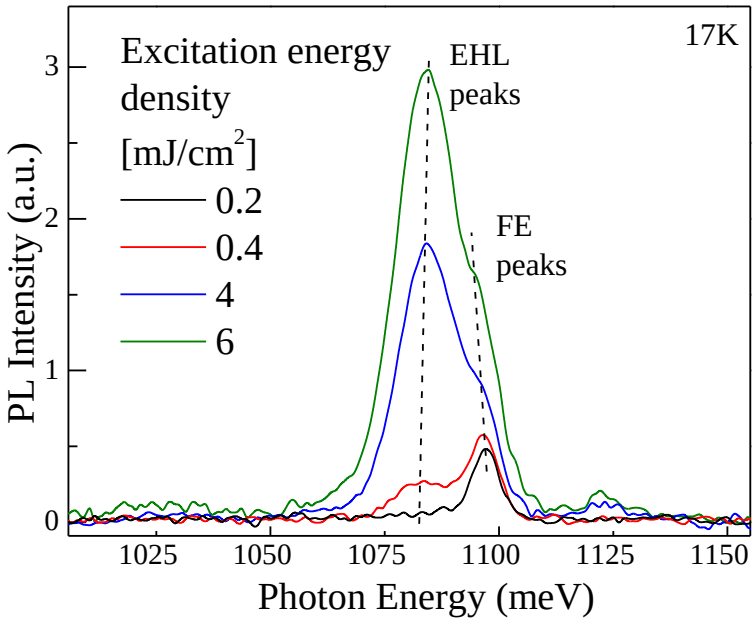

Figure 5.1 Low temperature PL spectra from a 2 μm SOI thin film obtained under pulsed excitation using various flux densities. Excitation densities were chosen to create sufficient EHPs for EHL condensation.

More information about these PL features can be obtained by applying curve-fits to the different PL spectra, extracting curve-fit parameters, and performing a quantitative comparison of the parameters for the two PL peaks. Figure 5.2 shows a double Gaussian curve-fit applied to the PL spectrum acquired using the 4 mJ/cm^2 energy density. The

positions of the FE and EHL PL peaks and their full-width-at-half-maximum (FWHM) are shown; parameters for the different spectra are tabulated in Table 5.1.

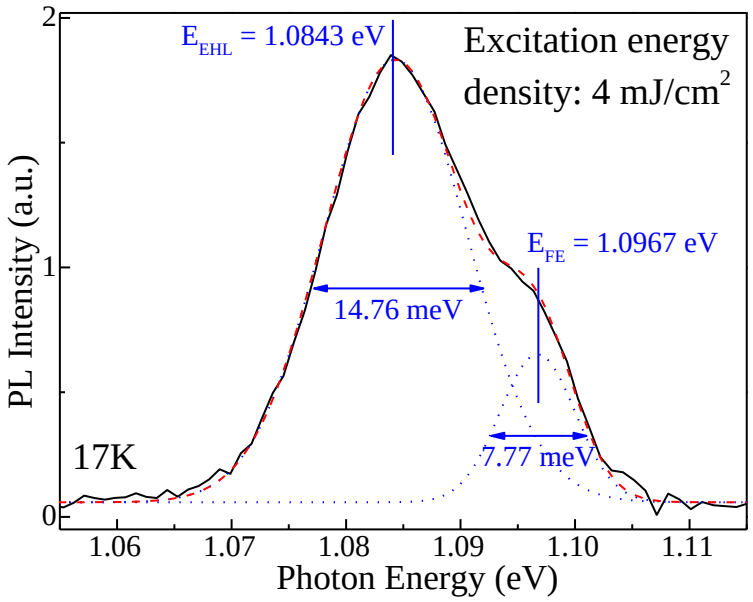

Figure 5.2 Example of a Gaussian curve fit applied to the PL spectra of a 2 μm thin SOI film. This was done to verify that the FWHM of PL features does not change significantly under different excitation energy densities.

The contribution of individual PL features to the total PL is indicated by the area under the respective Gaussian curve; these areas are plotted against the energy density of the excitation in Figure 5.3, on a double log scale. Note the linear increase of the PL arising due to recombination in the EHL, versus the heavily sublinear increase of the FE PL (lines with indicated slopes are shown as visual aids). Peak positions and FWHM of both PL features obtained by curve-fitting (Table 5.1) show no significant change ($\lesssim$ 1 meV), in agreement with published literature [11]. Figure 5.4 shows kinetics of the PL

features attributed to FE recombination and EHP recombination in the EHL, recorded at 1.096 eV and 1.083 eV respectively, for different excitation energy densities.

Table 5.1 Gaussian Curve-fit Parameters of PL Spectra

Excitation Energy Density mJ/cm^2	**PL peak attributed to**					
	EHL recombination			**FE recombination**		
	Position eV	**Area** a.u.	**FWHM** meV	**Position** eV	**Area** a.u.	**FWHM** meV
0.2	1.0836	72	14.25	1.09711	347	7.12
0.4	1.0837	412	14.36	1.09675	446	7.77
4	1.0843	2788	14.76	1.09673	490	7.77
6	1.0843	4844	15.54	1.09670	734	7.77

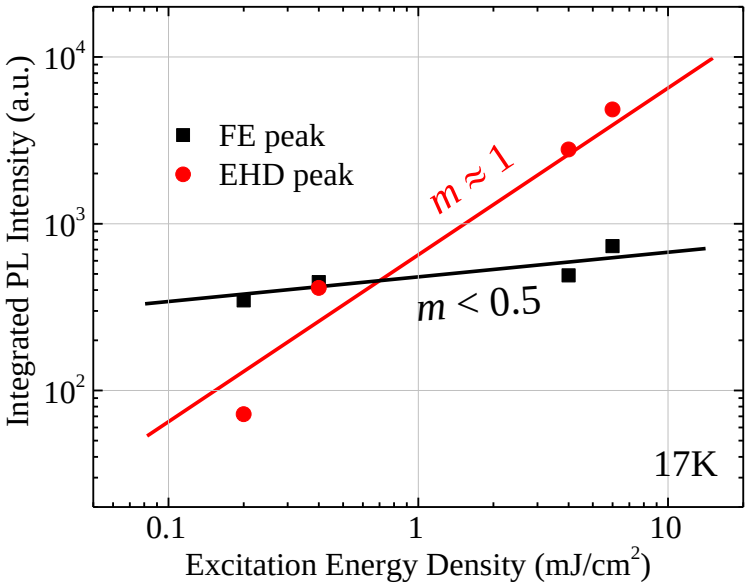

Figure 5.3 Comparison of total PL due to FE recombination with that due to EHL recombination, for a 2 μm thick SOI film. Each point on the log-log plot is obtained by applying Gaussian curve fits to the FE and EHL features in the PL spectra and extracting the area under each Gaussian. Lines are not numerical fits for data.

The presence of the EHL under these energy densities is clear from the spectra of Figure 5.1. At the lowest energy density (0.4 mJ/cm^2) shown, the EHL PL decay starts with a ~ 300 ns lifetime and quickly disappears by ~ 1 μs. PL due to FE recombination shows a surprisingly long rise time of ~ 1 μs. For comparison, in high-resistivity crystalline bulk Si, this rise time has been measured to be < 20 ns [6]. Subsequent decay however, is exponential with a ~ 6 μs lifetime, typical of free excitons in Si. Figure 5.4b shows kinetics of the same PL features under a higher excitation energy density of 2 mJ/cm^2. Initially, the EHL PL shows a similar lifetime as that under 0.4 mJ/cm^2; in addition, it shows a deceleration of the decay after about 1 μs before quenching completely. The PL due to FE recombination shows a shorter rise time of about 300 ns. More importantly, the following decay is not a single exponential, but shows multiple instances of acceleration and deceleration until ~ 4 μs before eventually decaying with the typical FE lifetime. Under the highest excitation energy density shown (10 mJ/cm^2, Figure 5.4c), the EHL PL shows an accelerated initial decay (lifetime ~ 180 ns) compared to lower energy densities, followed by an unusual increase in intensity at ~ 1 μs before completely quenching (better visible on the logarithmic scale of Figure 5.4). This delayed increase in PL intensity is more pronounced at the low energy tail of the EHL feature (Figure 5.1), and was recorded at an energy 10 meV lower than that of the peak center. The FE PL under 10 mJ/cm^2 excitation, shows a rise time shorter than the resolution of the experimental setup (~ 3 ns), continues to show the deceleration at ~ 1 μs and then decays with the typical μs lifetime. Note that the intensity of the EHL PL at all levels of excitation plummets very rapidly towards the end, clear on the log scale, as expected for the accelerating shrinkage of drops as the cutoff time mentioned earlier is approached.

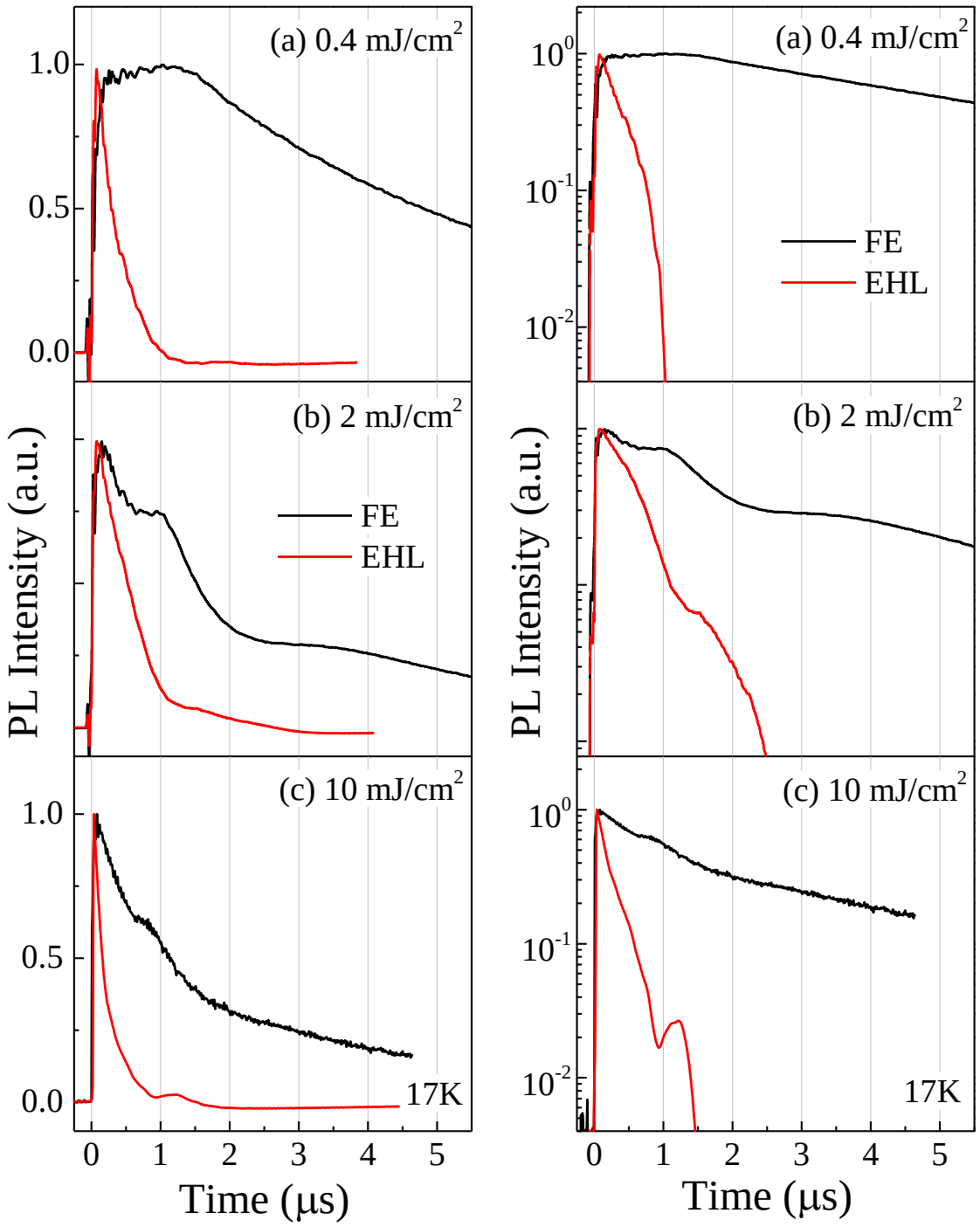

Figure 5.4 Concurrent PL kinetics of free excitons (black) and the electron-hole liquid (red) in 2 μm thick SOI films, at different excitation energy densities: (a) 0.4 mJ/cm^2, (b) 2 mJ/cm^2, and (c) 10 mJ/cm^2. A 6 ns pulse of 532 nm excitation completes before t = 0; data are normalized for comparison and shown on both linear (left) and log (right) scales; noise levels are ~ 3 orders of magnitude less than recorded PL.

5.2 Discussion

At high carrier concentrations, Auger recombination is known to be the dominant mechanism of recombination of EHPs, characterized by very short lifetimes on the order of ~ 10 ns; yet a recombination mechanism with a measured initial lifetime of ~ 100 ns is observed at high excitation levels. Additionally, the linear growth of the PL spectral feature due to recombination in the EHL with increasing excitation energy density (Figure 5.3) and the absence of saturation of the PL intensity at the highest energy densities used, indicate that Auger processes do not operate to significantly affect the EHL lifetime, up to the level of excitation used in these experiments. The contribution of Auger processes at and below this level, resulting in the ejection of free electrons or holes out of the condensate, and possible backflow to the condensate is expected to be small. Thus, at the temperature and EHP density created in the experiment, radiative recombination in the EHL competes with Auger recombination.

Impurities in crystals can serve as nucleation sites for the EHL; in very pure crystals, even mere fluctuations in EHP density can result in embryonic nucleation of droplets [12]. As the EHP concentration drops below the critical density for condensation, one expects EHPs to form excitons that then immediately diffuse to regions of lower concentration. While the global density of EHPs decreases as recombination proceeds, a delayed increase in PL intensity indicates that an *increase* in EHP density has somehow occurred. The delayed increase in PL is not explained by EHP density fluctuation- or impurity- assisted nucleation.

The observed PL dynamics are explained by considering recombination in the EHL, evaporation of carriers from the surface of drops, backflow of free carriers and excitons into the drops, and drift of carriers under strain-induced field at the Si/SiO_2 interface. These processes are explained in detail using rate equations, following a qualitative explanation of the observed phenomena.

SOI wafers formed by bonding are essentially stress-free at room temperature. At the experiment temperature however, a tensile stress develops in the Si, due to the mismatch in the coefficients of thermal expansion (CTE), and is maximum at the Si/SiO_2 interface. Stress in thin films, σ_f, due to differences in the CTE is given by [46]

$$\sigma_f = (\alpha_S - \alpha_f)\Delta T \frac{Y_f}{1 - \nu_f} \tag{5.1}$$

where α_S and α_f are the CTE of the substrate material and the overlying thin film respectively, ΔT is the temperature difference, Y_f and ν_f are the Young's modulus and Poisson ratio of the film respectively. Using mechanical properties of Si and SiO_2 [46], namely the CTE values of $\alpha_{SiO2} = 0.55\times10^{-6}$ K^{-1} and $\alpha_{Si} = 2.6\times10^{-6}$ K^{-1}, Y_{Si} = 185 GPa, and ν_{Si} = 0.28, and ΔT = 17 K – 300 K = – 283 K, the stress at the Si/SiO_2 interface is estimated to be +149 MPa, corresponding to a 0.081% tensile strain. The reduction in the energy bandgap at the interface brought about by this value of strain is estimated to be ~ 12 meV [82]. Elastic relaxation of strain in the Si layer produces a strain gradient in the film, which decreases away from the Si/SiO_2 interface, and a complete elastic relaxation

of the highly anisotropic Si lattice, as calculated for systems strained by Ge alloying, is expected to occur within ~ 150 nm [53]. These estimates indicate that a ~ 10 meV, 100 nm wide, graded potential well with the strain-maximum at the Si/SiO_2 interface, exists at the experiment temperature of 17 K.

When EHL drops are formed in the 2 μm thick Si film, they are subjected to physical acceleration in the presence of the graded, strain-induced field at the Si/SiO_2 interface, and to evaporation of carriers at 17 K, as they recombine. Indeed, EHL drops have been shown to be very sensitive to strain gradients [31], in which they can accelerate to the speed of sound [83]. Free carriers and FEs also accelerate in a strain gradient, towards the point of maximum strain, their drift velocity being directly proportional to the gradient [84]. Their accumulation in the strain potential well can locally surpass the critical density required for condensation [85]. EHL drops lose carriers to radiative recombination during their drift, but FEs have long lifetimes ($\gtrsim$ 1 μs) and diffusion lengths (~ 100 μm in bulk Si) [84, 86], so even those close to the surface may diffuse to the strain-field before accelerating under drift. Along with evaporated and Auger-ejected carriers from the EHL, FEs can thus form a condensate in the potential well at the interface. Subsequent EHL recombination would cause an increase in PL intensity, delayed by the transit time of FEs and carriers to the well.

Figure 5.5 shows the EHP phase diagram with the path along which carriers generate and recombine when the sample is sufficiently excited at 17K. The unusually long rise time of the FE PL under 0.4 mJ/cm^2 excitation (Figure 5.4a) shows excellent correlation with the decay of the EHL PL: the rise of the FE PL stops with the complete decay of EHL PL. This strongly suggests that recombination in the EHL is concomitant

with a release of FEs from the drops. The evaporation of FEs from droplets in Ge is known to be energetically more favorable than that of free electrons or holes [12]. Thus, at this level of excitation, the EHL decays mainly via radiative recombination and FE evaporation from the surface of drops; while the FE concentration, after being initially generated instantly by the light pulse, continues to be supplied by the evaporation process. After the EHL drops have vanished, the FE concentration decays exponentially with its typical lifetime. Also, this level of excitation places EHPs initially into the liquid region, close to the liquidus curve, from which they cycle back through the coexistence region as recombination proceeds. The non-exponential behavior of their luminescence in time (t) has been shown to be proportional to $(1 - t/t_c)^3$ [31], which incorporates evaporation. It is also influenced by backflow of excitons into the drop [30].

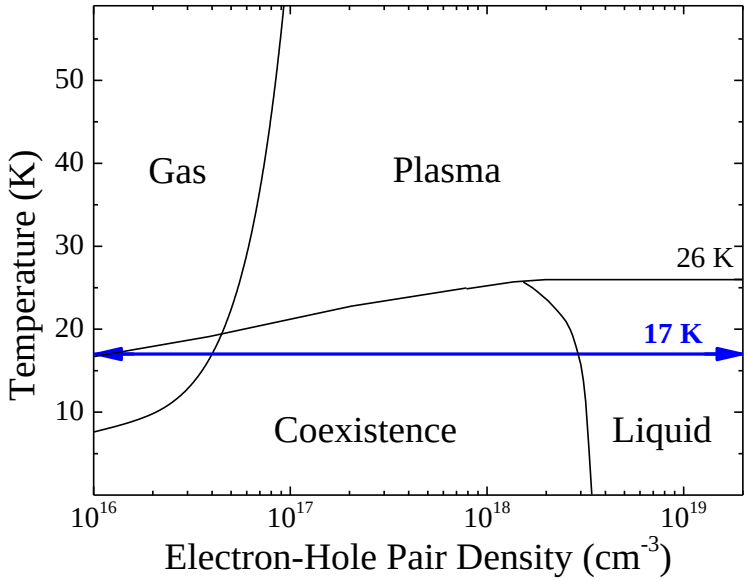

Figure 5.5 Phase diagram of EHPs in Si showing the path along which EHPs transition between phases in the current experiment.

An accurate calibration of EHP density created by excitation fluence is not available for the experimental setup, but the absence of the EHL PL spectral feature under the 0.2 mJ/cm^2 excitation level indicates that the system is sufficiently excited under the 0.4 mJ/cm^2 level to just enter the liquid region. Greater excitation energy densities generate enough non-equilibrium carriers to place the system well into the liquid region creating large EHL drops (drop radius increases as the third root of the number of EHPs [25]). If two condensation processes occur, one instantly from photoexcitation and the other from delayed accumulation at the interface, drop decay via radiative recombination should become more distinct, especially for the latter process, at higher excitation levels.

Under 2 mJ/cm^2 excitation, the cutoff time t_c, which is directly proportional to the initial drop radius, is expected to increase even without delayed condensation. A larger value of t_c is accompanied by a greater luminescence intensity, $\propto (1 - t/t_c)^3$ at a given time, as can be seen in Figure 5.4b until ~ 1 μs (compare with that under lower excitation). After 1 μs, the EHL PL presumably originates due to delayed condensation, and is strongly influenced by the drift of FEs into the potential well. With a large concentration of FEs released by the drops out of the well, the liquid inside the well loses EHPs to recombination and evaporation, which is countered by backflow and drift of FEs, resulting in a large delay in t_c. The behavior of FEs is correlated to that of the EHL: when the system is deep in the liquid region, the quick decay of FEs is due to their backflow and drift into the liquid (fewer available to recombine); as drops approach cutoff, a release of FEs supplies their decaying concentration, and their PL decay slows down. This also applies to the delayed condensation at the interface (t > 2 μs). After both

condensates, inside and outside the well have vanished, and the system has completely transitioned out of the coexistence region, FE decay continues with typical PL lifetime.

The delayed increase in the concentration of EHPs contributing to the condensate under 10 mJ/cm^2 excitation, occurs after the PL intensity has dropped by a factor of 50. Scaling relative to the 0.4 mJ/cm^2 excitation level (assumed just past liquidus curve), it follows that the density of EHPs has transitioned the system to the coexistence region, after which a new transition cycle starts. The prominence of this increase at an energy ~ 10 meV lower than the EHL PL peak position (1.083 eV) is strongly indicative that it originates from the interface potential well. The apparent reduction in initial lifetime of the PL decay is also explained by the lower photon detection energy. The obvious preemption of cutoff ($\propto$ drop initial radius) after the delayed PL increase is complete indicates that the maximum size of the drops formed in the well is smaller than that originally formed outside the well.

PL spectral line-shifts expected due to strain-induced energy bandgap reduction do not distinctly show in the spectra of Figure 5.1. This is because most of the excitation and recombination occurs away from the interface; any strain-induced red-shift or broadening due to recombination in incompletely relaxed regions would remain embedded in the broad PL features of Figure 5.1.

Quantitative modeling of the various physical phenomena that occur after the end of the excitation pulse can be done using rate equations that simulate the observed PL. In the following analysis, a rate equation for the EHL decay process is developed and analyzed to obtain expressions for drop radius and cutoff times, which should be reflected

in PL intensity measurements (recall that radius $\propto n^{1/3}$, where n is the number of EHPs in a drop), especially for the delayed increase seen at the highest excitation level used.

Although radiative recombination in the EHL appears to occur at two different regions of the Si film, initially close to the surface and later close to the interface, a measurement of the PL intensity does not represent this distinction. The current approach in modeling however, undertakes the calculation of the rate of change of the number of EHPs in the EHL, separately for each region, where the rate in either region is given by the sum of the rates of the recombination, evaporation, backflow, and drift processes. Therefore, the initial number of EHPs in the EHL (and thus the initial radius of drops), and the exciton population subject to drift are different for the two regions; i.e., a larger EHP concentration and no drift are assumed outside the potential well. The total rate of change, reflecting the experimentally measured PL signal, is then the sum of contributions from both regions.

The above simplification is quite crude since it does not spatially resolve processes in either region of the Si film, and resorts to using average values rather than continuously varying conditions such as the non-uniform strain-gradient ($\propto$ spatially varying depth of the potential well) and the exponential drop in initial EHP concentration from photoexcitation. It however greatly reduces the complexity in modeling the various phenomena, by assuming a constant strain-gradient and a constant initial EHP concentration while still retaining their different values in the two regions. Also, contributions to various processes from free carriers are ignored, assuming an equal number of electrons and holes become free from Auger processes, for example, and that

they quickly form excitons. The following rate equation summarizes the EHL decay process in each individual region.

$$\frac{d}{dt}\left(\frac{4}{3}\pi R^3 n_0\right) = -\frac{1}{\tau_0}\left(\frac{4}{3}\pi R^3 n_0\right) - 4\pi R^2 A T^2 \exp\left(\frac{-\varphi}{k_B T}\right) + \pi R^2 v_{th} N_{FE} + \pi R^2 v_\sigma N_{FE} \tag{5.2}$$

In the above equation, R [cm] is the radius of a single EHL drop, which evolves with time, n_0 [cm^{-3}] is the density of EHPs in a single drop and is assumed to be invariant between drops and through the decay, τ_0 [s] is the recorded recombination lifetime, A [A cm^{-2} K^{-2}] is the Richardson constant for thermionic emission, φ [eV] is the work function of the EHL condensate, v_{th} [cm s^{-1}] is the average thermal velocity of excitons, N_{FE} [cm^{-3}] is the concentration of FEs outside the EHL, and v_σ [cm s^{-1}] is the average drift velocity of excitons moving in a strain-induced field.

Note that each term in the equation tracks the behavior of the number of particles in the drop, $n = \frac{4}{3}\pi R^3 n_0$, which is directly proportional to the recorded PL intensity of the EHL. The density of EHPs in a drop, n_0, is only a function of temperature; since all experiments have been performed at a single T, it is assumed to be constant through the decay. Therefore the number of EHPs at a given instant is determined by drop radius at that time.

The first term in Equation 5.2 represents recombination at the levels of excitation used, and encompasses both radiative and non-radiative Auger processes, the combined effect being represented directly by measured lifetime τ_0 = 100 ns.

The second term describes evaporation, which is a function of the surface area of a spherical drop, and the rate of carrier loss due to thermionic emission of the condensate. The Richardson-Dushman formula for current due to thermionic emission, $AT^2 \exp\left(\frac{-\varphi}{k_B T}\right)$, is used with the Richardson constant $A = 2g\pi m^* k_B^2/h^3$, for particles of effective mass m^* and degeneracy g, and the condensation energy for EHPs in Si, φ = 2 meV [25], which is the energy given out by excitons as they condense into liquid form.

The third term of Equation 5.2 represents backflow, important for decelerations of the decay in the absence of other fluxes arriving at the surface of a drop [29]. It depends on the area of the drop seen by excitons as they diffuse in the crystal, and assuming their mean free path is much larger than drop radius, is simply πR^2. It also depends on the concentration of FEs available and on the velocity at which generated and evaporated FEs flow back into the drop, which is essentially the thermal velocity of excitons in Si. This velocity is estimated by the ratio of the diffusion length (~ 100 μm [84, 86]) and the lifetime (~ 1 μs) of excitons in Si, as 10^4 cm s^{-1}.

The fourth term in the rate equation calculates the rate at which FEs accumulate in drops in the presence of a strain-gradient, applicable only to the modeled interface region. It depends on the drop area, πR^2, seen by excitons and their drift velocity. Although the drift velocity can be derived from first principles, it has been explicitly calibrated under stress applied along the [100] direction in Si [84], and for the estimated change in

bandgap energy (~ 10 meV) over the width of the potential well (~ 100 nm), the drift velocity is estimated as 8×10^7 cm s^{-1}.

Several features can be discerned by a further analysis of the EHL equation. By differentiating and simplifying, the rate equation is seen to have the form $\dot{x} = -ax - b$ (as shown below), which has a standard solution: $x = \left[\left(x_0 + {}^{b}/_{a}\right)\exp(-at)\right] - \left({}^{b}/_{a}\right)$. This allows us to obtain expressions for drop radius and cutoff time.

$$\left(\frac{4}{3}\pi n_0\right)\frac{d}{dt}R^3 = -\left(\frac{4}{3}\pi n_0\right)\frac{1}{\tau_0}R^3 - \left(\frac{4}{3}\pi n_0\right)\left(\frac{3AT^2\exp(-\varphi/k_BT)}{n_0} - \frac{(v_{th}+v_\sigma)N_{FE}}{4n_0}\right)R^2$$

$$\Rightarrow \frac{dR}{dt} = -\frac{1}{3\tau_0}R - \left(\frac{AT^2\exp(-\varphi/k_BT)}{n_0} - \frac{(v_{th}+v_\sigma)N_{FE}}{12n_0}\right) \tag{5.3}$$

Using the standard form of the solution for this differential equation, and rewriting the evaporation, backflow, and drift terms for brevity as β, ξ, and ζ respectively, an expression for drop radius is obtained.

$$R(t) = \left[R(0) + 3\tau_0\left(\beta - (\xi+\zeta)\right)\right]\exp\left(\frac{-t}{3\tau_0}\right) - 3\tau_0\left(\beta - (\xi+\zeta)\right) \tag{5.4}$$

where the following substitutions have been used.

$$\beta = \frac{AT^2 \exp(-\varphi/k_B T)}{n_0} \tag{5.5}$$

$$\xi = \frac{v_{th} N_{FE}}{12 n_0} \tag{5.6}$$

$$\zeta = \frac{v_\sigma N_{FE}}{12 n_0} \tag{5.7}$$

Equation 5.4 allows us to predict cutoff time, i.e., the value of t when $R(t)$ becomes 0.

$$t_c = 3\tau_0 \ln\left(1 + \frac{R(0)}{3\tau_0(\beta - (\xi + \zeta))}\right) \tag{5.8}$$

By applying a Taylor series expansion of the natural log function in Equation 5.8, or by simply graphing the above expression, it can be seen that for $t_c < 3\tau_0$, the above expression is well approximated by $t_c = R(0) / [\beta - (\xi + \zeta)]$. If backflow is assumed to be negligible in the region outside the potential well, this expression qualitatively predicts that cutoff time should increase if the (strongly T dependent-) evaporation term β decreases: at lower T, cutoff is expected to occur later. More importantly, for the interface region, the denominator is decreased due to a contribution from ζ, leading to an additional delay in approaching cutoff. Recall that the expression in Equation 5.8 and Equations 5.2-4 apply separately to the two regions previously defined ($\zeta = 0$ outside the well), and the actual cutoff time seen in PL measurements would be the longer of the two.

Substituting the above approximation for t_c in Equation 5.4, a simpler expression for drop radius is obtained. This explains why the intensity of the EHL PL is expected to vary as $(1 - t/t_c)^{1/3}$:

$$R(t) = R(0)\left(1 - \frac{t}{t_c}\right) \tag{5.9}$$

Although the concentrations of FEs and EHPs in the EHL depend on one another, their recombination rates are independent. The actual coupling between their populations arises primarily from FEs evaporating outside the potential well and entering the interface well region to re-condense. Therefore, a free exciton rate equation is also necessary, which would have to be solved simultaneously with Equation 5.2 for the EHL. Since the evaporation of FEs from drops is energetically more favorable than that of free carriers, several terms arise directly from the EHL rate equation. Following a similar approach, a rate equation for FEs is developed.

$$\frac{dN_{FE}}{dt} = -\frac{1}{\tau_{FE}}N_{FE} + D4\pi R^2 A T^2 \exp\left(\frac{-\varphi}{k_B T}\right) - D\pi R^2 v_{th} N_{FE} - D_I \pi R^2 v_\sigma N_{FE} \tag{5.10}$$

where τ_{FE} is the free exciton lifetime, D is the number of EHL drops outside the potential well, and D_I is the number of drops in the potential well at the interface. The factor for the number of drops in either region is introduced because Equation 5.10 describes

exciton dynamics in the entire Si film, whereas Equation 5.2 describes dynamics for a single drop. Also, spatial limits of the potential well make it likely that the number of drops formed in the delayed condensation process is less than that formed outside the well. Finally, for a direct comparison with PL intensity, the expression for the number of EHPs in a drop, $n = \frac{4}{3}\pi R^3 n_0$, can be rearranged, differentiated, and substituted in Equations 5.3 and 5.10, to obtain equations in *n* rather than radius.

In conclusion, the influence of Si/SiO_2 interface on carrier recombination in an SOI thin film has been experimentally investigated. The dominant recombination channel at low temperature and high electron-hole-pair densities is not seen to be Auger recombination as is the case in bulk Si, but radiative recombination in the electron-hole liquid. Recombination dynamics of the liquid are seen to be strongly correlated to FE recombination. A potential well formed at the Si/SiO_2 interface at the experiment temperature creates a strain-induced field. Large concentrations of free carriers and excitons drift in the field to produce a delayed condensation into liquid at the interface. This shows that a reverse phase transition of decaying EHL drops, back to the liquid phase, can be made possible by the introduction of sites for re-nucleation of the condensate.

EHL drops accelerating towards the region of maximum strain can be expected to reduce surface recombination. If stress in the Si thin film can be engineered via the oxide layer to produce a larger strain at the interface while retaining the crystalline integrity of the structure, the EHL PL at the interface (lower energy) could be quite efficient. This would be highly desirable for a waveguide type application. The set of rate equations developed above account for EHL and FE concentrations and ignores free carriers. In the

Si system, where strong carrier-carrier interaction is expected to change free carrier concentrations via Auger processes, a more complete model would additionally track the third unknown variable, via a free-carrier rate equation.

CHAPTER 6

CONCLUSIONS

Based on discussions in Chapters 4 and 5, several interesting conclusions were made about recombination processes in Si/SiGe three-dimensional nanostructures and Silicon-On-Insulator systems.

In the Si/SiGe three-dimensional nanostructure system, low Ge content in clusters produces band bending at the Si/SiGe heterointerfaces, which show less intermixing. An Auger Fountain mechanism is observed, but not enhanced compared to high Ge content nanostructures. The upper limit of the exciton diffusion length in Si/SiGe nanostructures is seen to be 40 nm, over 2 orders of magnitude shorter than that seen in Si nanowires and 4 orders shorter than bulk materials. The accumulation of holes in SiGe clusters leads to an increase in the rate of Auger recombination and can cause a delayed PL degradation.

In the Silicon-On-Insulator system, it is seen that an enhanced surface area-to-volume ratio leads to increased evaporation of free excitons from the electron-hole-liquid. Strain at the Si/SiO2 interface is seen to prolong the lifespan of electron-hole-liquid drops in SOI films. Most importantly, reverse phase transitions of decaying electron-hole-liquid drops back to the liquid phase can be made possible by the introduction of nucleation sites for condensation.

In agreement with the majority of textbooks, Auger recombination is seen to be the dominant recombination mechanism at high carrier concentrations in these

nanostructures. However, radiative recombination of carriers in the electron-hole liquid is much faster than the free exciton recombination in bulk Si and SOI systems, and appears to successfully compete with Auger recombination until very high carrier concentrations, ~ 10^{19} cm^{-3}. The coexistence of a type II energy band alignment at Si/SiGe heterointerfaces, electron-hole droplets in Si, and Auger processes in responsible for several unusual PL properties in SiGe and Si nanostructures.

REFERENCES

[1] L. Tsybeskov, D. J. Lockwood, and M. Ichikawa, "Silicon Photonics: CMOS Going Optical [Scanning the Issue]," *Proceedings of the IEEE,* vol. 97, pp. 1161-1165, 2009.

[2] V. I. Klimov, "Quantization of Multiparticle Auger Rates in Semiconductor Quantum Dots," *Science,* vol. 287, pp. 1011-1013, 2000.

[3] P. T. Landsberg, *Recombination in semiconductors*. Cambridge, UK: Cambridge University Press, 2003.

[4] L. Tsybeskov and D. J. Lockwood, "Silicon-germanium nanostructures for light emitters and on-chip optical interconnects," *Proceedings of the IEEE,* vol. 97, pp. 1284-1303, 2009.

[5] W. Seidel, A. Titkov, J. P. Andre, P. Voisin, and M. Voos, "High-efficiency energy up-conversion by an "Auger fountain" at an InP-AlInAs type-II heterojunction," *Physical Review Letters,* vol. 73, pp. 2356-2359, 1994.

[6] E.-K. Lee, D. J. Lockwood, J.-M. Baribeau, A. M. Bratkovsky, T. I. Kamins, and L. Tsybeskov, "Photoluminescence dynamics and Auger fountain in three-dimensional Si/SiGe multilayer nanostructures," *Physical Review B: Condensed Matter and Materials Physics,* vol. 79, p. 233307, 2009.

[7] J. Cuthbert, "Recombination Kinetics of Excitonic Molecules and Free Excitons in Intrinsic Silicon," *Physical Review B,* vol. 1, pp. 1552-1557, 1970.

[8] P. J. Dean, J. R. Haynes, and W. F. Flood, "New Radiative Recombination Processes Involving Neutral Donors and Acceptors in Silicon and Germanium," *Physical Review,* vol. 161, pp. 711-729, 1967.

[9] J. Weber and M. Alonso, "Near-band-gap photoluminescence of Si-Ge alloys," *Physical Review B,* vol. 40, pp. 5683-5693, 1989.

[10] G. Davies, "The optical properties of luminescence centers in silicon," *Physical Reports,* vol. 176, pp. 83-188, 1989.

[11] J. Shah, M. Combescot, and A. H. Dayem, "Investigation of Exciton-Plasma Mott Transition in Si," *Physical Review Letters,* vol. 38, pp. 1497-1500, 1977.

[12] C. D. Jeffries, "Electron-Hole Condensation in Semiconductors," *Science,* vol. 189, pp. 955-964, 1975.

[13] C. Delerue, M. Lannoo, G. Allan, and E. Martin, "Auger and Coulomb Charging Effects in Semiconductor Nanocrystallites," *Physical Review Letters,* vol. 75, pp. 2228-2231, 1995.

[14] A. G. Cullis, L. T. Canham, and P. D. J. Calcott, "The structural and luminescence properties of porous silicon," *Journal of Applied Physics,* vol. 82, pp. 909-965, 1997.

[15] M. Nirmal, B. O. Dabbousi, M. G. Bawendi, J. J. Macklin, J. K. Trautman, T. D. Harris, and L. E. Brus, "Fluorescence intermittency in single cadmium selenide nanocrystals," *Nature,* vol. 383, pp. 802-804, 1996.

[16] A. L. Efros and M. Rosen, "Random telegraph signal in the photoluminescence intensity of a single quantum dot," *Physical Review Letters,* vol. 78, pp. 1110-1113, 1997.

[17] D. I. Chepic, A. L. Efros, A. I. Ekimov, M. G. Ivanov, V. A. Kharchenko, I. A. Kudriavtsev, and T. V. Yazeva, "Auger ionization of semiconductor quantum drops in a glass matrix," *Journal of Luminescence,* vol. 47, pp. 113-127, 1990.

[18] B. O. Dabbousi, J. Rodriguez-Viejo, F. V. Mikulec, J. R. Heine, H. Mattoussi, R. Ober, K. F. Jensen, and M. G. Bawendi, "(CdSe)ZnS Core-Shell Quantum Dots: Synthesis and Optical and Structural Characterization of a Size Series of Highly Luminescent Materials," *Journal of Physical Chemistry B,* vol. 101, pp. 9463-9475, 1997.

[19] T. Krauss and L. Brus, "Charge, Polarizability, and Photoionization of Single Semiconductor Nanocrystals," *Physical Review Letters,* vol. 83, pp. 4840-4843, 1999.

[20] T. D. Krauss, S. O'Brien, and L. E. Brus, "Charge and Photoionization Properties of Single Semiconductor Nanocrystals," *Journal of Physical Chemistry B,* vol. 105, pp. 1725-1733, 2001.

[21] M. Nirmal and L. Brus, "Luminescence Photophysics in Semiconductor Nanocrystals," *Accounts of Chemical Research,* vol. 32, pp. 407-414, 1999.

[22] C. Kittel, *Introduction to Solid State Physics,* 8th ed. Hoboken, NJ: Wiley, 2005.

[23] C. à la Guillaume, M. Voos, and Y. Pétroff, "Electron-hole drops in Ge-Si alloys," *Physical Review B,* vol. 10, pp. 4995-5002, 1974.

[24] S. W. Koch and H. Haug, "On the electron-hole plasma phase transition in direct and indirect gap semiconductors," *Physics Letters,* vol. 74A, pp. 250-252, 1979.

[25] Y. Pokrovskii, "Condensation of non-equilibrium charge carriers in semiconductors," *Physica Status Solidi (a),* vol. 11, pp. 385-410, 1972.

[26] J. R. Haynes, "Experimental Observation of the Excitonic Molecule," *Physical Review Letters,* vol. 17, pp. 860-862, 1966.

[27] A. S. Kaminskii and Y. E. Pokrovskii, "Recombination Radiation of the Condensed Phase of Nonequilibrium Carriers in Silicon," *Journal of Experimental and Theoretical Physics Letters,* vol. 11, pp. 255-257, 1970.

[28] J. Wolfe, W. Hansen, E. Haller, R. Markiewicz, C. Kittel, and C. Jeffries, "Photograph of an Electron-Hole Drop in Germanium," *Physical Review Letters,* vol. 34, pp. 1292-1293, 1975.

[29] R. M. Westervelt, T. K. S. Lo, J. L., and C. D. Jeffries, "Decay Kinetics of Electron-Hole-Drop and Free-Exciton Luminescence in Ge: Evidence for Large Drops," *Physical Review Letters,* vol. 32, pp. 1051-1054, 1974.

[30] J. C. Hensel, T. G. Phillips, and T. M. Rice, "Evaporation of Metallic Exciton Droplets in Optically Pumped Germanium," *Physical Review Letters,* vol. 30, pp. 227-230, 1973.

[31] Y. E. Pokrovskii and K. I. Svistunova, "Heating of electron-hole drops in an inhomogeneous-deformation field," *Journal of Experimental and Theoretical Physics Letters,* vol. 17, pp. 451-453, 1973.

[32] L. V. Keldysh, "The electron-hole liquid in semiconductors," *Contemporary Physics,* vol. 27, pp. 395-428, 1986.

[33] T. K. Lo, B. J. Feldman, and C. D. Jeffries, "New Phenomena in Exciton Condensation in Germanium," *Physical Review Letters,* vol. 31, pp. 224–226, 1973.

[34] J. I. Pankove, *Optical processes in semiconductors*. New York, NY: Dover, 1975.

[35] M. Dyakonov and V. Kachorovskii, "Nonthreshold Auger recombination in quantum wells," *Physical Review B,* vol. 49, pp. 17130-17138, 1994.

[36] S. E. Thompson, S. Guangyu, C. Youn Sung, and T. Nishida, "Uniaxial-process-induced strained-Si: extending the CMOS roadmap," *IEEE Transactions on Electron Devices,* vol. 53, pp. 1010-1020, 2006.

[37] J.-M. Baribeau, N. L. Rowell, and D. J. Lockwood, "Advances in the growth and characterization of Ge quantum dots and islands," *Journal of Materials Research,* vol. 20, pp. 3278-3293, 2005.

[38] O. G. Schmidt, O. Kienzle, Y. Hao, K. Eberl, and F. Ernst, "Modified Stranski-Krastanov growth in stacked layers of self-assembled islands," *Applied Physics Letters,* vol. 74, pp. 1272-1274, 1999.

[39] E.-K. Lee, "Optical properties and carrier transport in Si/ Si1-xGex nanostructures," PhD Dissertation, Department of Electrical and Computer Engineering, New Jersey Institute of Technology, Newark, NJ, 2008.

[40] A. Dunbar, M. Halsall, P. Dawson, U. Bangert, M. Miura, and Y. Shiraki, "The effect of strain field seeding on the epitaxial growth of Ge islands on Si(001)," *Applied Physics Letters,* vol. 78, p. 1658, 2001.

[41] J.-M. Baribeau, T. E. Jackman, D. C. Houghton, P. Maigne, and M. W. Denhoff, "Growth and characterization of $Si_{1-x}Ge_x$ and Ge epilayers on (100) Si," *Journal of Applied Physics,* vol. 63, pp. 5738-5746, 1988.

[42] Y. W. Mo, D. Savage, B. Swartzentruber, and M. Lagally, "Kinetic pathway in Stranski-Krastanov growth of Ge on Si(001)," *Physical Review Letters,* vol. 65, pp. 1020-1023, 1990.

[43] T. I. Kamins, E. C. Carr, R. S. Williams, and S. J. Rosner, "Deposition of three-dimensional Ge islands on Si(001) by chemical vapor deposition at atmospheric and reduced pressures," *Journal of Applied Physics,* vol. 81, pp. 211-219, 1997.

[44] K. Brunner, "Si/Ge nanostructures," *Reports on Progress in Physics,* vol. 65, pp. 27-72, 2002.

[45] J.-M. Baribeau, X. Wu, N. L. Rowell, and D. J. Lockwood, "Ge dots and nanostructures grown epitaxially on Si," *Journal of Physics: Condensed Matter,* vol. 18, p. 36, 2006.

[46] J. D. Plummer, M. D. Deal, and P. B. Griffin, *Silicon VLSI technology: fundamentals, practice, and modeling*, 2nd ed. Upper Saddle River, NJ: Prentice Hall, 2000.

[47] J. C. S. Bean, T.T., L. C. Feldman, A. T. Fiory, and R. T. Lynch, "Pseudomorphic growth of Ge_xSi_{1-x} on silicon by molecular beam epitaxy," *Applied Physics Letters*, vol. 44, pp. 102-104, 1984.

[48] F. K. LeGoues, B. S. Meyerson, J. F. Morar, and P. D. Kirchner, "Mechanism and conditions for anomalous strain relaxation in graded thin films and superlattices," *Journal of Applied Physics,* vol. 71, pp. 4230-4243, 1992.

[49] R. People, J. C. Bean, D. V. Lang, A. M. Sergent, H. L. Störmer, K. W. Wecht, R. T. Lynch, and K. Baldwin, "Modulation doping in Ge_xSi_{1-x}/Si strained layer heterostructures," *Applied Physics Letters,* vol. 45, pp. 1231-1233, 1984.

[50] X. Liao, J. Zou, D. Cockayne, J. Qin, Z. Jiang, X. Wang, and R. Leon, "Strain relaxation by alloying effects in Ge islands grown on Si(001)," *Physical Review B*, vol. 60, pp. 15605-15608, 1999.

[51] J.-M. Baribeau, X. Wu, M.-J. Picard, and D. J. Lockwood, "Characterization of Coherent Si1−xGex Island Superlattices on (100) Si," *MRS Proceedings*, vol. 958, pp. L10-32, 2007.

[52] H. K. Shin, D. J. Lockwood, and J. M. Baribeau, "Strain in coherent-wave SiGe/Si superlattices," *Solid State Communications*, vol. 114, pp. 505-510, 2000.

[53] S. Christiansen, M. Albrecht, H. P. Strunk, and H. J. Maier, "Strained state of Ge(Si) islands on Si: Finite element calculations and comparison to convergent beam electron-diffraction measurements," *Applied Physics Letters*, vol. 64, pp. 3617-3619, 1994.

[54] E. Stach. (2011, October 21). *Diffraction Contrast Imaging (MSE 582 Lecture 10)* [Online]. Available: http://nanohub.org/resources/4013

[55] R. F. Egerton, *Physical Principles of Electron Microscopy: An Introduction to TEM, SEM, and AEM*, 1st ed. New York, NY: Springer, 2005.

[56] C.-P. Liu, J. Gibson, D. Cahill, T. Kamins, D. Basile, and R. Williams, "Strain Evolution in Coherent Ge/Si Islands," *Physical Review Letters*, vol. 84, pp. 1958-1961, 2000.

[57] P. D. Miller, C.-P. Liu, W. L. Henstrom, J. M. Gibson, Y. Huang, P. Zhang, T. I. Kamins, D. P. Basile, and R. S. Williams, "Direct measurement of strain in a Ge island on Si(001)," *Applied Physics Letters*, vol. 75, p. 46, 1999.

[58] D. Halliday, R. Resnick, and J. Walker, *Fundamentals of Physics*, 6 ed. Hoboken, NJ: John Wiley & Sons, 2001.

[59] Virginia Semiconductor. (2011, March 15). *Optical Properties of Si and Ge* [Online]. Available: www.virginiasemi.com

[60] J. Humlicek, "Optical spectroscopy of SiGe," in *Properties of Strained and Relaxed Silicon Germanium*. vol. 12, E. Kasper, Ed., London, UK: INSPEC, the Institution of Electrical Engineers, 1995, pp. 116-120.

[61] B. V. Kamenev, L. Tsybeskov, J.-M. Baribeau, and D. J. Lockwood, "Photoluminescence and Raman scattering in three-dimensional Si/$Si_{1-x}Ge_x$ nanostructures," *Applied Physics Letters*, vol. 84, pp. 1293-1295, 2004.

[62] M. Tajima, S. Ibuka, and S. Arai, "Condensate luminescence under ultraviolet excitation: application to the study of ultrathin SOI layers," *Materials Science & Engineering, B: Solid-State Materials for Advanced Technology*, vol. B91-92, pp. 10-15, 2002.

[63] T. Baier, U. Mantz, K. Thonke, R. Sauer, F. Schaeffler, and H.-J. Herzog, "Type-II band alignment in Si/Si1-xGex quantum wells from photoluminescence line shifts

due to optically induced band-bending effects: experiment and theory," *Physical Review B: Condensed Matter,* vol. 50, pp. 15191-15196, 1994.

[64] M. Thewalt, D. Harrison, C. Reinhart, J. Wolk, and H. Lafontaine, "Type II Band Alignment in Si1-xGex/Si(001) Quantum Wells: The Ubiquitous Type I Luminescence Results from Band Bending," *Physical Review Letters,* vol. 79, pp. 269-272, 1997.

[65] G. Abstreiter, "Silicon/Germanium Quantum Structures," *Solid State Communications,* vol. 92, pp. 5-10, 1994.

[66] G. Abstreiter, H. Brugger, T. Wolf, H. Jorke, and H. Herzog, "Strain-Induced Two-Dimensional Electron Gas in Selectively Doped Si/Si_xGe_{1-x} Superlattices," *Physical Review Letters,* vol. 54, pp. 2441-2444, 1985.

[67] N. Pauc, V. Calvo, J. Eymery, F. Fournel, and N. Magnea, "Electron hole liquid in silicon single quantum wells," *Optical Materials,* vol. 27, pp. 995-999, 2005.

[68] J. P. Hirth and J. Lothe, *Theory of dislocations*. New York, NY: McGraw-Hill, 1967.

[69] W. F. Hosford, *Mechanical behavior of materials*. New York, NY: Cambridge University Press, 2005.

[70] M. S. Tyagi and R. Van Overstraeten, "Minority carrier recombination in heavily-doped silicon," *Solid-State Electronics,* vol. 26, pp. 577-597, 1983.

[71] J. Brunner, W. Jung, P. Schittenhelm, M. Gail, G. Abstreiter, J. Gonderman, B. Hadam, T. Koester, B. Spangenberg, H. G. Roskos, H. Kurz, H. Gossner, and I. Eisele, "Local epitaxy of Si/SiGe wires and dots," *Journal of Crystal Growth,* vol. 157, pp. 270-275, 1995.

[72] E.-K. Lee, L. Tsybeskov, and T. I. Kamins, "Photoluminescence thermal quenching in three-dimensional multilayer Si/SiGe nanostructures," *Applied Physics Letters,* vol. 92, pp. 033110-1-033110-3, 2008.

[73] P. M. Fauchet, J. von Behren, K. D. Hirschman, L. Tsybeskov, and S. P. Duttagupta, "Porous Silicon Physics and Device Applications: A Status Report," *Physica Status Solidi A,* vol. 165, pp. 3-13, 1998.

[74] R. A. Street, "Recombination in amorphous semiconductors," *Physical Review B: Solid State,* vol. 17, pp. 3984-3995, 1978.

[75] F. Mollot, J. Cernogora, and C. Benoit a la Guillaume, "Excitation spectra of photoluminescence fatigue and creation of paramagnetic centers in amorphous GexSe1-x," *Journal of Non-Crystalline Solids,* vol. 35-36, pp. 939-944, 1980.

[76] N. F. Mott and E. A. Davis, *Electronic processes in non-crsytalline materials*, 2nd ed. New York, NY: Oxford University Press, 1979.

[77] P. N. Grillot, S. A. Ringel, E. A. Fitzgerald, G. P. Watson, and Y. H. Xie, "Minority- and majority-carrier trapping in strain-relaxed $Ge_{0.3}Si_{0.7}$/Si heterostructure diodes grown by rapid thermal chemical-vapor deposition," *Journal of Applied Physics,* vol. 77, pp. 676-685, 1995.

[78] H. Klauk, T. N. Jackson, S. F. Nelson, and J. O. Chu, "Thermal stability of undoped strained Si channel SiGe heterostructures," *Applied Physics Letters,* vol. 68, pp. 1975-1977, 1996.

[79] S. Ibuka and M. Tajima, "Characterization of silicon-on-insulator wafers by photoluminescence decay lifetime measurement," *Japanese Journal of Applied Physics, Part 2: Letters,* vol. 39, pp. L1124-L1126, 2002.

[80] M. Tajima, H. Yoshida, S. Ibuka, and S. Kishino, "Correlation between photoluminescence lifetime and interface trap density in silicon-on-insulator wafers," *Japanese Journal of Applied Physics, Part 2: Letters,* vol. 42, pp. L429-L431, 2003.

[81] R. B. Hammond and R. N. Silver, "Temperature dependence of the exciton lifetime in high-purity silicon," *Applied Physics Letters,* vol. 36, pp. 68-71, 1980.

[82] J. Munguía, G. Bremond, J. M. Bluet, J. M. Hartmann, and M. Mermoux, "Strain dependence of indirect band gap for strained silicon on insulator wafers," *Applied Physics Letters,* vol. 93, p. 102101, 2008.

[83] V. S. Bagaev, T. I. Galkina, O. V. Gogolin, and L. V. Keldysh, "Motion of Electron-hole Drops in Germanium," *Journal of Experimental and Theoretical Physics Letters,* vol. 10, pp. 195-198, 1969.

[84] M. Tamor and J. Wolfe, "Drift and Diffusion of Free Excitons in Si," *Physical Review Letters,* vol. 44, pp. 1703-1706, 1980.

[85] P. L. Gourley and J. P. Wolfe, "Spatial Condensation of Strain-Confined Excitons and Excitonic Molecules into an Electron-Hole Liquid in Silicon," *Physical Review Letters,* vol. 40, pp. 526-530, 1978.

[86] Y. H. Chen and S. A. Lyon, "Photoluminescence and Diffusivity of Free Excitons in Doped Silicon," *IEEE Journal of Quantum Electronics,* vol. 25, pp. 1053-1055, 1989.